

Spin-polarized quantum confinement in nanostructures: Scanning tunneling microscopy

Hirofumi Oka, Oleg O. Brovko, Marco Corbetta, Valeri S. Stepanyuk,
Dirk Sander, and Jürgen Kirschner

Max-Planck-Institut für Mikrostrukturphysik, Weinberg 2, D-06120 Halle/Saale, Germany

(published 3 October 2014)

Experimental investigations of spin-polarized electron confinement in nanostructures by scanning tunneling microscopy (STM) and scanning tunneling spectroscopy (STS) are reviewed. To appreciate the experimental results on the electronic level, the physical basis of STM is elucidated with special emphasis on the correlation between differential conductance, as measured by STS, and the electron density of states, which is accessible in *ab initio* theory. Experimental procedures which allow one to extract the electron dispersion relation from energy-dependent and spatially resolved STM and STS studies of electron confinement are reviewed. The role of spin polarization in electron confinement is highlighted by both experimental and theoretical insights, which indicate variation of the spin polarization in sign and magnitude on the nanometer scale. This review provides compelling evidence for the necessity to include spatial-dependent spin-resolved electronic properties for an in-depth understanding and quantitative assessment of electron confinement in magnetic nanostructures and interaction between magnetic adatoms.

DOI: [10.1103/RevModPhys.86.1127](https://doi.org/10.1103/RevModPhys.86.1127)

PACS numbers: 68.37.Ef, 73.20.-r, 74.20.Pq, 75.25.-j

CONTENTS

I. Introduction	1127	B. Spin-polarized electron scattering on magnetic substrates and films	1145
II. Probing Spin-polarized Electron Confinement with STM	1129	C. Spin-polarized quantum confinement on a magnetic nanostructure	1146
A. Working principle of STM	1129	D. Tuning spin polarization on the nanoscale by confinement	1148
B. Spectroscopy measurements of the differential conductance by STM	1130	V. Spin Polarization of Surface-state Electrons Upon Scattering at Magnetic Scatterers: Theory and Experiment	1149
C. Spin-polarized STM: The method of choice to study spin-polarized electron confinement	1131	A. Spin polarization induced by adatoms	1149
D. Experimental realization of SP-STM	1133	B. Quantum mirages and magnetic interactions in quantum corrals	1150
1. Spin-sensitive STM tips	1133	C. Surface-state-mediated interactions and exchange coupling between adatoms	1150
a. Magnetic materials	1133	D. Spin polarization induced by magnetic nanostructures	1151
b. Optically pumped GaAs	1133	E. Induced spin polarization in systems with strong spin-orbit coupling	1153
c. Superconducting materials in magnetic fields	1133	VI. Impact of Spin-dependent Electron Confinement on Transport Properties	1155
2. Mode of operation	1134	A. Experiments on spatially modulated TMR	1155
a. Constant-current mode	1134	B. <i>Ab initio</i> based theory of spin-dependent transport	1157
b. Spectroscopic mode	1134	VII. Concluding Remarks and Future Developments	1158
c. Differential magnetic mode	1134	Acknowledgments	1159
E. SP-STM in magnetic fields: A tool to study spin polarization	1135	References	1159
1. Experimental setup	1135		
2. Characterization and control of magnetic SP-STM tips	1135		
III. Confinement of Surface-state Electrons	1137		
A. Origin of two-dimensional surface states	1137		
B. Probing electronic surface states experimentally by STM	1137		
C. Examples of electron confinement involving surface-state electrons	1139		
1. Stripes	1139		
2. Stepped surfaces	1140		
3. Islands and vacancy islands	1142		
D. Electron confinement without surface states	1143		
IV. Spin-polarized Surface States on Magnetic Substrates: Theory and Experiment	1144		
A. Experiments to extract the electron spin polarization	1144		

I. INTRODUCTION

Quantum phenomena are often strikingly evident when the electronic properties of nanostructures are studied (Chang, Esaki, and Tsu, 1974; Dingle, Wiegmann, and Henry, 1974; Ando, Fowler, and Stern, 1982; Weisbuch and Vinter, 1991; Kelly, 1995). With shrinking spatial extension of at least one dimension to the nanometer (nm) scale, electron spectroscopy may reveal discrete energy levels. Also, the wave-particle dualism of electrons emerges as a spatial variation of

electronic properties on the nm scale. The electron dispersion relation determines this length scale. For example, on Cu(111) and Au(111) electronic surface states (Gartland and Slagsvold, 1975; Kevan, 1983; Goldmann, Dose, and Borstel, 1985; Kevan and Gaylord, 1987; Reinert *et al.*, 2001) determine the electron dispersion relation near the Fermi energy. Typically, the electron wavelength at the Fermi energy is of the order of nanometers, significantly larger than the nearest-neighbor atomic distances on metal substrates, which is of the order of 0.2 nm.

Scanning tunneling microscopy (STM) and scanning tunneling spectroscopy (STS) (Binnig *et al.*, 1982a, 1982b, 1983; Hamers, Tromp, and Demuth, 1986; Kaiser and Jaklevic, 1986) offer an unsurpassed spatial resolution on the atomic scale to study not only the atomic corrugation, but also the electronic properties of nanostructures. Pioneering STM studies have presented stunning maps of spatially modulated electronic properties induced by scattering off step edges (Crommie, Lutz, and Eigler, 1993b; Hasegawa and Avouris, 1993), by electron confinement at atomic terraces (Avouris *et al.*, 1994), and in quantum corrals (Crommie, Lutz, and Eigler, 1993a), which were constructed by atomic manipulation (Eigler and Schweizer, 1990; Stroscio and Eigler, 1991), by subsurface impurities (Schmid *et al.*, 1996; Weismann *et al.*, 2009), and in molecular networks (Pennec *et al.*, 2007). The resulting modulation patterns were ascribed to interference between scattered electrons at the boundaries of the nanostructures (Heller *et al.*, 1994; Fiete and Heller, 2003). STM and STS can also detect electronic states confined in a direction perpendicular to the surface, in thin films (Kubby and Greene, 1992; Becker and Berndt, 2010) and nanostructures (Altfeder, Matveev, and Chen, 1997; Yang *et al.*, 2009), where the motion of electrons is confined by the surface and the interface with substrates.

What is new in this review? Electrons carry in addition to charge also a spin, and the spin is the basis for magnetism of matter. Thus, *a priori* it is not obvious how spatial variations of the electron density also impact the magnetic properties on the nanoscale. Here it is our goal to present an understanding of the spatially varying spin-dependent electronic properties of nanostructures and at surfaces.

To appreciate the significance of magnetism on the nanoscale we remind the interested reader that the properties of thin magnetic films and magnetic nanostructures have been a central topic of research for fundamental physics and applications (Kronmüller and Parkin, 2007). When the size of magnetic films or magnetic nanostructures is reduced to the nanometer or the atomic scale, their magnetic properties change and differ from their bulk properties, for example, enhanced magnetic anisotropies (Gambardella *et al.*, 2003; Ouazi *et al.*, 2012), spin reorientation transitions (Sander, 2004), and noncollinear magnetism (Wulfhchel and Gao, 2010) have been reported. Thus, the understanding of the magnetic properties of magnetic films and magnetic nanostructures with reduced dimensions on the electronic level is decisive.

For example, giant magnetoresistance has been realized in a variety of multilayers consisting of ferromagnetic and nonmagnetic thin films (Baibich *et al.*, 1988; Binasch *et al.*, 1989; Parkin, More, and Roche, 1990). The magnetic coupling

between ferromagnetic layers oscillates between ferromagnetic and antiferromagnetic with the thickness of nonmagnetic layers separating them (Parkin, More, and Roche, 1990, 1991; Cebollada *et al.*, 1991). Spin-polarized quantum-well states formed in nonmagnetic spacer layers are found to be responsible for the oscillatory magnetic coupling (Ortega and Himpfel, 1992; Ortega *et al.*, 1993). Quantum-well states formed in not only nonmagnetic but also ferromagnetic layers also lead to oscillations of magnetocrystalline anisotropy energy with thickness (Würsch *et al.*, 1997; U. Bauer *et al.*, 2011; Przybylski *et al.*, 2012; Manna *et al.*, 2013). Ferromagnetism of ferromagnetic semiconductors, where a small amount of magnetic impurities is doped into nonmagnetic semiconductors, emerges due to the *p-d* exchange interaction between valence band holes and localized *d* electrons of magnetic dopants (Ohno, 1998; Dietl, 2010). Interfaces of complex oxide heterostructures show a variety of magnetic properties (Bibes, Villegas, and Barthélémy, 2011). Unpaired dangling bonds can induce magnetic moments and magnetic ordering, for example, at the edges of graphene nanostructures (Yazyev, 2010) and Si(553)-Au surfaces (Erwin and Himpfel, 2010; Snijders *et al.*, 2012; Aulbach *et al.*, 2013).

At the surface, spin-polarized surface states play an important role in various spin-dependent phenomena. Spin-polarized STM (SP-STM) offers insight into the spin-dependent electronic structures with high spatial resolution (Bode, 2003; Wulfhchel and Kirschner, 2007; Wiesendanger, 2009). Combined experimental and theoretical studies reveal the decisive role of spin-dependent electron confinement in magnetic nanostructures for spin polarization and spin-dependent transport properties on the nanoscale (Niebergall, Stepanyuk *et al.*, 2006; Oka *et al.*, 2010, 2011). Magnetic adatoms on metal surfaces induce oscillations of the spin polarization in nonmagnetic metals due to spin-dependent scattering of surface-state electrons. This leads to a long-range magnetic coupling between magnetic adatoms on the surfaces (Stepanyuk *et al.*, 2005; Meier *et al.*, 2008; Khajetoorians *et al.*, 2012), described by the so-called Ruderman-Kittel-Kasuya-Yosida (RKKY) interaction (Ruderman and Kittel, 1954; Kasuya, 1956; Yosida, 1957). Systems with strong spin-orbit coupling are predicted to show a rotation of the spin-polarized local density of states around magnetic impurities adsorbed on surfaces (Guo and Franz, 2010; Stróżecka, Eiguren, and Pascual, 2011; Liu, Qi, and Zhang, 2012; Lounis, Bringer, and Blügel, 2012).

In this article, we review STM and STS investigations of electron confinement at nanostructures and its impact on spin-dependent phenomena. In Sec. II we review the tunneling theory used for the interpretation of STM and STS and SP-STM and SP-STs measurements, and we address experimental aspects of SP-STM. In Sec. III we review selected results on electron confinement in various nanostructures studied by STM and STS. In Sec. IV we highlight results on scattering and confinement as studied by SP-STM in its application to magnetic nanostructures. The impact of magnetic adatoms and magnetic nanostructures on the spin polarization of nonmagnetic substrates is discussed in Sec. V. In Sec. VI we review the role of spin-dependent electron confinement

for transport properties, such as the tunneling magnetoresistance (TMR).

This review focuses on elastic tunneling processes. Important insights into single-atom magnetic properties and magnonic excitations are accessible by inelastic electron tunneling spectroscopy, and the interested reader is referred to Heinrich *et al.* (2004), Hirjibehedin, Lutz, and Heinrich (2006), Hirjibehedin *et al.* (2007), Gao *et al.* (2008), Otte *et al.* (2008, 2009), Fernández-Rossier (2009), Lorente and Gauyacq (2009), Tsukahara *et al.* (2009), Fransson, Eriksson, and Balatsky (2010), Loth, Lutz, and Heinrich (2010), Khajetoorians *et al.* (2011), and Gauyacq, Lorente, and Novaes (2012).

II. PROBING SPIN-POLARIZED ELECTRON CONFINEMENT WITH STM

A. Working principle of STM

Electron tunneling describes the phenomenon in which an electron can tunnel between two electrodes that are separated by an insulating layer (Esaki, 1958; Giaever, 1960a, 1960b; Bardeen, 1961; Fisher and Giaever, 1961). The insulating layer can be an oxide or vacuum, and its typical thickness is in the range of 3–10 Å. Electron tunneling gives rise to a tunneling current, which depends on the thickness of the insulating layer d and the applied voltage V . In STM, the

insulating layer is given by the vacuum between tip and sample, and this tunnel barrier width d corresponds to the tip-sample distance, which is of the order of 3–6 Å in typical working conditions. The high spatial resolution of STM on the subatomic scale is based on an exponential dependence of the tunneling current on the distance between tip and sample, as discussed below. A more detailed description and technical aspects of STM can be found in Chen (1993), Wiesendanger (1994), Bonnell (2001), and Foster and Hofer (2006). We point out here that the tunneling process is necessarily an electron-spin-dependent effect. Tunneling is described as a spin-conserving phenomenon. Spin-up (spin-down) electrons can tunnel only into unoccupied spin-up (spin-down) states. The magnitude of the tunneling current and its energy dependence $I(V)$ depend on the spin polarization of both tip and sample as discussed in Sec. II.C.

In order to interpret experimental data obtained by STM, it is crucial to characterize the tunneling process on the electronic level (Briggs and Fisher, 1999; Drakova, 2001; Hofer, Foster, and Shluger, 2003, and references therein). Here we briefly introduce widely accepted concepts used to interpret experimental results of STM and STS measurements.

Bardeen (1961) treated the tunneling phenomenon in first-order time-dependent perturbation theory,¹ for the first time, to describe the tunneling current. The tunneling current I can be derived as follows:

$$\begin{aligned} I &= I_{T \rightarrow S} - I_{S \rightarrow T} \\ &= \frac{2\pi e}{\hbar} \sum_{\mu, \nu} \{f(E_{\mu}^T)[1 - f(E_{\nu}^S + eV)] - f(E_{\nu}^S + eV)[1 - f(E_{\mu}^T)]\} |M_{\mu, \nu}|^2 \delta(E_{\nu}^S - E_{\mu}^T) \\ &= \frac{2\pi e}{\hbar} \sum_{\mu, \nu} [f(E_{\mu}^T) - f(E_{\nu}^S + eV)] |M_{\mu, \nu}|^2 \delta(E_{\nu}^S - E_{\mu}^T), \end{aligned} \quad (1)$$

where $f(E)$ is the Fermi function, V is the applied sample-bias voltage, $M_{\mu, \nu}$ is the tunneling matrix element between unperturbed states ψ_{μ} of the tip and ψ_{ν} of the sample surface, and E_{μ} (E_{ν}) is the energy of the state ψ_{μ} (ψ_{ν}) in the absence of tunneling. The δ function ensures the conservation of energy for elastic tunneling. The summation includes all possible initial and final states of the tip and the sample. Bardeen (1961) described the tunneling matrix element as

$$M_{\mu, \nu} = -\frac{\hbar^2}{2m} \int dS (\psi_{\mu}^* \nabla \psi_{\nu} - \psi_{\nu} \nabla \psi_{\mu}^*), \quad (2)$$

where the integral is evaluated over any surface lying entirely within the vacuum barrier region separating the two electrodes. At this point, it is possible to calculate the tunneling current using Eq. (1) with Eq. (2) if the electronic states of the tip ψ_{μ} and the sample ψ_{ν} are known. This would give a complete understanding of experimental results of STM. However, the atomic structure of the tip

is unknown in most STM experiments. The atomic structure of the tip can be characterized using transmission electron microscopy (Rodary *et al.*, 2011) or field ion microscopy (Müller and Tsong, 1969; Tsong, 1990; Okawa *et al.*, 2011; Sugiura *et al.*, 2011; Nagai *et al.*, 2014). Detailed structural and elemental characterizations of tips in STM are scarce, and it is still quite challenging to experimentally identify the atomic structure of the tip.

Tersoff and Hamann (1983, 1985) extended Bardeen's tunneling theory into a more accessible relation between the tunneling current and the electronic properties of the sample. They assumed that the electronic state of the tip ψ_{μ} can be described by a spherically symmetric wave function, that is, an s wave [see also Chen (1990b)]. The s -wave tip state can be described as

$$\psi_{\mu} = \frac{C}{\kappa \rho} e^{-\kappa \rho}, \quad (3)$$

where $\kappa = \sqrt{2m\phi/\hbar^2}$ is the decay constant, ϕ is the work function, $\rho = |\vec{r} - \vec{r}_0|$ is the radial distance from the center of curvature of the tip \vec{r}_0 , and C is a normalization coefficient. A schematic of the geometry at the tip apex of the STM is depicted in Fig. 1. Tersoff and Hamann (1983, 1985) further considered

¹A detailed discussion of Bardeen's tunneling theory is given by Duke (1969) and Gottlieb and Wesoloski (2006).

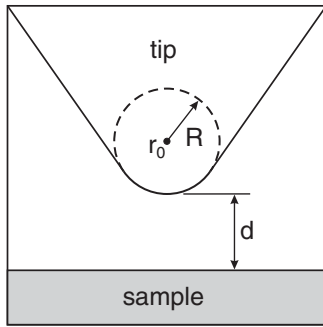


FIG. 1. Schematic of the tip apex as used in the mathematical description of the tunneling process. The STM tip is assumed to be locally spherical with radius of curvature R , where it approaches closest to the sample surface (shaded). The distance of nearest approach is d . The center of curvature of the tip is located at \vec{r}_0 . Note that this schematic is idealized as it does not consider the atomic structure of a tip apex. Adapted from Tersoff and Hamann, 1985.

the limits of small sample-bias voltage ($V \leq 10$ mV) and low temperature, where Eq. (1) is simplified as

$$I = \frac{8\pi^3 C^2 \hbar^3 e}{\kappa^2 m^2} eV n_T(E_F) n_S(\vec{r}_0, E_F), \quad (4)$$

and a linear $I(V)$ characteristic results for small sample-bias voltages. Here $n_T(E_F)$ is the density of states of the tip at the Fermi energy E_F and $n_S(\vec{r}_0, E_F)$ is the local density of states (LDOS) of the sample at the tip apex position \vec{r}_0 at the Fermi energy, which are given as

$$n_T(\epsilon) = \sum_{\nu} \delta(E_{\nu}^T - \epsilon), \quad (5)$$

and

$$n_S(\vec{r}_0, \epsilon) = \sum_{\mu} \delta(E_{\mu}^S - \epsilon) |\psi_{\mu}(\vec{r}_0)|^2. \quad (6)$$

Equation (4) tells us that the tunneling current measured with STM is proportional to the sample LDOS at the tip apex position \vec{r}_0 at the Fermi energy E_F within the approximations made above. Thus, STM images obtained in a constant-current mode and at low sample-bias voltage reflect maps of constant LDOS of the sample at the Fermi energy E_F , as measured at the tip apex position \vec{r}_0 .

Note that the sample states ψ_{μ} decay exponentially into the vacuum region

$$|\psi_{\mu}(\vec{r}_0)|^2 \propto \exp[-2\kappa(R + d)], \quad (7)$$

and an exponential dependence of the tunneling current on the tip-sample distance d ,

$$I \propto n_S(\vec{r}_0, E_F) \propto \exp(-2\kappa d), \quad (8)$$

results. Assuming that the work function of the sample is 5 eV (Michaelson, 1977), a change in the tip-sample distance by 1 Å induces a variation in the tunneling current by 1 order of

magnitude. Therefore, even very small changes in the tip-sample distance are easily detected, leading to an extremely high vertical resolution of STM. This vertical resolution is mainly limited by experimental noise. Currently, this vertical noise can be as low as 200 fm_{*p-p*} in liquid-He-cooled STM on vibrationally isolated setups (Wedekind, 2010; Zhang *et al.*, 2011). The exponential dependence of the tunneling current on distance is also one of the key factors for the atomic resolution of the STM. For a detailed discussion concerning the origin of the atomic resolution of the STM, see Chen (1990a, 1991). We note that the decay of the sample LDOS through the vacuum toward the tip apex position depends in a nontrivial manner on the symmetry of the involved wave functions, and very different decay lengths may occur for states with minority- or majority-spin character. This is essential for the proper assessment of spin-dependent STM results. This aspect is extensively discussed in Sec. II.C.

The proximity between the tip apex and the sample surface also leads to a chemical interaction between the electrodes. Thus, forces acting between the tip apex and the sample need to be considered, and this interaction also influences resolution and data interpretation in STM considerably. A detailed discussion of these aspects goes beyond the scope of this review, and we refer the interested reader to the numerous articles on this aspect (Clarke *et al.*, 1996; Hofer *et al.*, 2001; Hofer, Foster, and Shluger, 2003; Hofer, 2003; Palotás and Hofer, 2005).

B. Spectroscopy measurements of the differential conductance by STM

One of the most powerful and important applications of STM is spectroscopic measurements of the differential conductance dI/dV as a function of sample-bias voltage. In the following, we briefly elucidate the correlation between differential conductance and LDOS in STS. This unique possibility to map the sample LDOS with lateral atomic precision serves as the basis for a comparison between calculated electronic properties of nanostructures and the experimental results.

The equation for the tunneling current in Eq. (1) can be expressed for a finite bias voltage ($eV \ll \phi$, where ϕ is the work function) within the approximation of the s -wave tip state in the following form:

$$I = \frac{8\pi^3 C^2 \hbar^3 e}{\kappa^2 m^2} \int n_T(\epsilon + eV) n_S(\vec{r}_0, \epsilon) [f(\epsilon - E_F^S) - f(\epsilon + eV - E_F^T)] d\epsilon, \quad (9)$$

where $n_T(\epsilon)$ is the DOS of the tip [Eq. (5)], and $n_S(\vec{r}_0, \epsilon)$ is the LDOS of the sample at the tip apex position \vec{r}_0 [Eq. (6)]. The DOS of the tip $n_T(\epsilon)$ is assumed to be constant and given by n_T . By replacing the Fermi function with the step function, Eq. (9) can be further simplified into

$$I(V) \propto n_T \int_{E_F}^{E_F + eV} n_S(\vec{r}_0, \epsilon) d\epsilon. \quad (10)$$

The tunneling current for a finite bias voltage V is proportional to the integrated LDOS between the Fermi energy E_F and the

sample-bias voltage V , eV , of the sample at the tip apex position \vec{r}_0 . The differential conductance dI/dV follows from the energy derivative of the tunneling current I in Eq. (10), as

$$\frac{dI}{dV}(V) \propto n_T n_S(\vec{r}_0, E_F + eV). \quad (11)$$

Thus, measurements of the differential conductance allow us to directly compare the experimental data with the calculated sample LDOS, as provided by theory.

We point out that in the discussion above *unperturbed* tip and sample states (E_μ and E_ν) in the absence of tunneling are considered. A finite bias voltage applied to the STM tunnel junction may induce electronic modifications of both tip and sample, as described by, e.g., the Stark effect (Becker, Golovchenko, and Swartzentruber, 1985; Binnig *et al.*, 1985; Limot *et al.*, 2003; Kröger *et al.*, 2004). A close tip-sample distance may also cause structural relaxations of both sample and tip apex due to chemical forces (Hofer, Foster, and Shluger, 2003; Huang, Stepanyuk, and Kirschner, 2006; Huang *et al.*, 2006).

Another critical assumption made above is that the DOS of the tip n_T is constant. The DOS of the tip may drastically change from tip to tip, whereas the LDOS of the sample is fixed provided that the sample has a well-characterized atomic structure (Crommie, Lutz, and Eigler, 1993c). Therefore, in experiments we strive for reproducibility of spectroscopic features in differential conductance measurements with different tips to reliably characterize the LDOS of the sample.

C. Spin-polarized STM: The method of choice to study spin-polarized electron confinement

Electrons carry a spin in addition to charge and the phenomenon of electron tunneling is spin dependent (Tedrow and Meservey, 1973; Julliere, 1975). Thus, when materials with a spin polarization are used for both tip and sample, the tunneling current depends on the spin-dependent electronic properties of both electrodes. Figure 2 schematically illustrates the spin-dependent electron tunneling between two spin-polarized electrodes. We recall that the DOS of ferromagnets splits up into majority- and minority-spin states due to exchange interaction between electrons (Kittel, 1949). Consequently, the DOS is different for majority- and minority-spin states at a given energy, giving rise to spin polarization. The spin polarization $P(\epsilon)$ is defined as the difference of the DOS of majority- n_\uparrow and minority- n_\downarrow spin electrons at a given energy ϵ , normalized to the total DOS,

$$P(\epsilon) = \frac{n_\uparrow(\epsilon) - n_\downarrow(\epsilon)}{n_\uparrow(\epsilon) + n_\downarrow(\epsilon)}. \quad (12)$$

To illustrate the proof of principle of SP-STM, we assume identical DOSs for tip and sample in Fig. 2. When a small positive sample-bias voltage is applied, electrons tunnel from occupied tip states to empty sample states. Assuming that the spin orientation of tunneling electrons is conserved during the tunneling process, i.e., spin-up (spin-down) electrons always tunnel into spin-up (spin-down) states, the magnitude of the

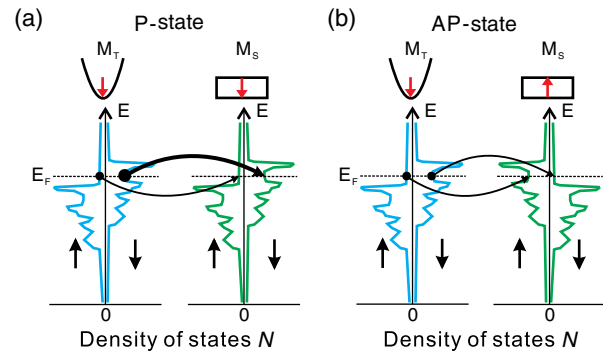


FIG. 2 (color online). Simplified picture of spin-polarized tunneling within a hypothetical spin-split density of states model in parallel (P) and antiparallel (AP) magnetization orientations. The spin orientation of the tunneling electrons is assumed to be conserved during tunneling, i.e., spin-up electrons always tunnel into spin-up states and spin-down electrons always tunnel into spin-down states. Arrows (bottom) indicate the DOS of spin-up and spin-down electrons. The spin direction is antiparallel to the magnetic moment (Chikazumi, 1997). M_T and M_S (top arrows) denote the magnetization orientation of tip and sample, respectively. (a) P and (b) AP alignment of tip and sample magnetization. Adapted from Wulfhekel and Kirschner, 2007.

tunneling current differs for spin-up and spin-down channels [Fig. 2(a)]. Since in our example around the Fermi energy the DOS of the spin-down state is higher for both tip and sample than that of the spin-up state, a tunneling current in the spin-down channel is larger than in the spin-up channel, as indicated by arrows with different thicknesses. When the sample magnetization is switched to the antiparallel (AP) state [Fig. 2(b)], the tunneling current in the spin-up channel remains the same; however, that of the spin-down channel is reduced.

In this peculiar example, the tunneling current is lower in the AP case than in the P case as seen in Fig. 2. Thus the magnitude of the tunneling current depends on the relative orientation of the sample magnetization with respect to the tip magnetization. This phenomenon is known as the TMR effect (Moodera, Nassar, and Mathon, 1999; Tsymbal, Mryasov, and LeClair, 2003; Parkin *et al.*, 2007; Miao, Münzenberg, and Moodera, 2011). The working principle of SP-STM is based on this phenomenon. We note explicitly that, in general, it is not true that a P state gives a larger tunneling current than an AP state. We discuss in Secs. II.E.2 and VI.A and show explicitly in Figs. 4(b) and 29(a) that the variation of $dI/dV(V)$ and $I(V)$ is a spectroscopic feature, where, depending on the sample-bias voltage, a larger differential conductance and conductance can also be obtained for the AP state. Thus, in general, it is not possible to distinguish between AP and P states from the observation of a change of the $I(V)$ and $dI/dV(V)$ signal alone. It is mandatory to perform field-dependent measurements to obtain a reliable interpretation of SP-STM data (Rodary *et al.*, 2009).

Wortmann *et al.* (2001) extended the Tersoff-Hamann theory (Tersoff and Hamann, 1983, 1985) of the non-spin-polarized tunneling current for the spin-polarized case. They introduced two-component spinors for the wave functions. They introduce the quantization direction of the tip, which is

defined by the magnetization axis of the tip \vec{e}_M^T . The tip and sample states are described as

$$\Psi_\nu^T = \begin{pmatrix} \psi_{\nu\uparrow}^T \\ 0 \end{pmatrix} \quad \text{or} \quad \begin{pmatrix} 0 \\ \psi_{\nu\downarrow}^T \end{pmatrix} \quad (13)$$

and

$$\Psi_\mu^S = \begin{pmatrix} \psi_{\mu\uparrow}^S \\ \psi_{\mu\downarrow}^S \end{pmatrix}, \quad (14)$$

respectively.

The tip state at the tip apex is modeled as a spherically symmetric wave function, that is, an s wave, comparable to the Tersoff-Hamann model, as discussed in Sec. II.A. Here it is further assumed that the s -wave states have the same decay constant κ and the same normalization coefficient C for both spin-up and spin-down states. The DOS of the tip is assumed to be constant in energy but different in magnitude for spin-up, n_T^\uparrow , and spin-down, n_T^\downarrow electrons. Under these assumptions, the tunneling current can be decomposed into two parts, a non-spin-polarized current I_0 and a spin-polarized current I_P :

$$I(\vec{r}_0, V, \theta) = I_0(\vec{r}_0, V) + I_P(\vec{r}_0, V, \theta), \quad (15)$$

$$= \frac{4\pi^3 C^2 \hbar^3 e}{\kappa^2 m^2} [n_T \tilde{n}_S(\vec{r}_0, V) + \vec{m}_T \tilde{\vec{m}}_S(\vec{r}_0, V)], \quad (16)$$

where $n_T = n_T^\uparrow + n_T^\downarrow$ is the non-spin-polarized DOS of the tip, $\tilde{n}_S(\vec{r}_0, V)$ is the energy integral from E_F to $E_F + eV$ of the sample LDOS, and $\vec{m}_T = (n_T^\uparrow - n_T^\downarrow) \vec{e}_M^T$ is the spin-polarized DOS of the tip. $\tilde{\vec{m}}_S(\vec{r}_0, V)$ is the vector of the energy integral of the spin-polarized LDOS of the sample (\vec{m}_S) and is given for low temperatures by

$$\tilde{\vec{m}}_S(\vec{r}_0, V) \simeq \int_{E_F}^{E_F + eV} \vec{m}_S(\vec{r}_0, \epsilon) d\epsilon, \quad (17)$$

with

$$\vec{m}_S(\vec{r}_0, \epsilon) = \sum_\mu \delta(E_\mu - \epsilon) \Psi_\mu^{S\dagger}(\vec{r}_0) \sigma \Psi_\mu^S(\vec{r}_0), \quad (18)$$

where σ is Pauli's spin matrix. The energy derivative of the tunneling current I for the spin-polarized case in Eq. (16) gives the differential conductance of SP-STM measurements as

$$\frac{dI}{dV}(\vec{r}_0, V) \propto n_T n_S(\vec{r}_0, E_F + eV) + \vec{m}_T \vec{m}_S(\vec{r}_0, E_F + eV). \quad (19)$$

Equation (19) tells us that the differential conductance measured with the SP-STM contains two components. The first term of Eq. (19) is a non-spin-polarized part and reflects the spin-integrated LDOS of the sample (n_S) at an energy of $E_F + eV$ and a tip apex position \vec{r}_0 . The second term of Eq. (19) corresponds to a spin-polarized part and reflects the projection of the vector of the spin-polarized sample LDOS

(\vec{m}_S) at an energy of $E_F + eV$ and a tip apex position \vec{r}_0 onto the spin-polarized DOS of the tip (\vec{m}_T). It depends on the magnitudes of \vec{m}_T and \vec{m}_S , and $\cos\theta$ as $\vec{m}_T \vec{m}_S = |\vec{m}_T| |\vec{m}_S| \cos\theta$. The angle θ describes the angle between the magnetization directions of the tip and the sample. In the case of zero spin polarization of either the tip or the sample, the second term in Eq. (19), which describes the spin-polarized part, vanishes.

To investigate spin polarization on the sample with SP-STM, the asymmetry of the differential conductance, $A_{dI/dV}$, is introduced. The asymmetry is defined as (Oka *et al.*, 2010)

$$A_{dI/dV} \equiv \frac{dI/dV_{AP} - dI/dV_P}{dI/dV_{AP} + dI/dV_P}, \quad (20)$$

where dI/dV_{AP} and dI/dV_P are the differential conductance signals measured with the tip and sample magnetization in AP and P configurations, respectively. The AP and P configurations correspond to $\theta = 180^\circ$ and 0° , and thus $\cos\theta = -1$ and 1 in Eq. (19), respectively. Therefore, the asymmetry of the differential conductance in Eq. (20) can be linked to the spin polarization of the tip P_T and sample P_S :

$$A_{dI/dV}(\vec{r}_0, V) = -P_T P_S(\vec{r}_0, E_F + eV). \quad (21)$$

Note that the differential conductance measured by STM [Eq. (11)] is always evaluated at the tip apex position \vec{r}_0 . A displacement of the tip apex position, i.e., a different tip-sample distance, may induce a change of this quantity. Therefore, differential conductance measurements should be performed at a defined tip-sample distance to allow a reliable comparison between measurements (Hörmandinger, 1994). STM measurements are usually performed in a constant-current mode, where not the tip-sample distance but the tunneling current is kept constant during scanning of a tip over a sample surface. When $\tilde{n}_S(\vec{r}_0, V)$ and/or $\tilde{\vec{m}}_S(\vec{r}_0, V)$ depend on the spatial position on the sample surface, which causes a variation of the tunneling current [Eqs. (11) and (19)], the tip-sample distance varies with the spatial position in constant-current mode. Even at the same spatial position on the surface, a change in the magnetization direction of the sample induces a change in the tunneling current [Eq. (19)], leading to a different tip-sample distance. This effect is exploited in SP-STM studies in the constant-current mode (Wiesendanger *et al.*, 1990; Rusponi *et al.*, 2005). An important insight from theory is that the spin-dependent DOS of a sample decays on different length scales for majority- and minority-spin states (Ignatiev, 2009). A striking result is that the calculations for a Co bilayer on Cu(111) reveal a decay of the minority d states on a shorter length scale as compared to that of the majority s - p states. Thus, the measured differential conductance asymmetry may depend critically on the tip-sample distance. This leads to the experimental question: At what tip-sample distance are the spectroscopy measurements performed? This aspect is taken care of by performing spectroscopy measurements with an open feedback loop of the STM. This means that the tip-sample distance is stabilized at certain stabilization parameters of the sample-bias voltage V_{stab} and the tunneling current I_{stab} , before the feedback loop is opened and the bias voltage is

ramped between V_{\min} and V_{\max} , while the $I(V)$ and $dI/dV(V)$ signals are recorded simultaneously. These stabilization parameters are chosen such that V_{stab} falls into the spectral range where the spin-polarized current in Eq. (16) is negligible. This can be confirmed by a comparison of constant-current STM images at V_{stab} and I_{stab} for P and AP states (Kubetzka *et al.*, 2003).

D. Experimental realization of SP-STM

Experimental aspects of SP-STM have been discussed in several reviews (Bode, 2003; Wulfhchel and Kirschner, 2007; Wiesendanger, 2009, 2011; Wulfhchel and Gao, 2010), and in the following we focus on selected aspects to provide the necessary insight to appreciate SP-STM experiments.

1. Spin-sensitive STM tips

Spin-polarized tips are the essential aspects in SP-STM. There are several ways to produce spin-polarized states in materials, which were already realized in planar tunnel junctions: (1) magnetic materials (Julliere, 1975; Maekawa and Gfvert, 1982; Miyazaki and Tezuka, 1995; Moodera *et al.*, 1995), (2) optically pumped GaAs (Prins, Abraham, and van Kempen, 1993), and (3) superconducting materials in magnetic fields (Meservey, Tedrow, and Fulde, 1970; Tedrow and Meservey, 1971a, 1971b, 1973). These procedures are also followed to obtain spin-polarized tips for SP-STM.

a. Magnetic materials

The use of magnetic materials for tips is the most common way to reliably perform SP-STM measurements so far. There have been many reports on successful SP-STM measurements using bulk magnetic material tips (Wiesendanger *et al.*, 1990, 1992; Subagyo and Sueoka, 2006) or magnetic-film-covered W tips (Bode, Getzlaff, and Wiesendanger, 1998; Kleiber *et al.*, 2000; Kubetzka *et al.*, 2002). Bulk ferromagnetic materials can be used for SP-STM tips. However, their large magnetic stray fields, which were evaluated to induce more than 500 mT at a tip-sample distance of 25 nm (Wadas and Hug, 1992), have the potential to modify the magnetic structures of the sample. Thus their application to SP-STM tips is limited. To reduce the magnetic stray field effect, bulk antiferromagnetic materials are good candidates for tips in SP-STM and, indeed, bulk Cr tips were successfully used as SP-STM tips (Li Bassi *et al.*, 2007; Schlenhoff *et al.*, 2010; Corbetta *et al.*, 2012). Corbetta *et al.* (2012) revealed that the spin orientation of the apex of bulk Cr tips can be controlled by external magnetic fields due to the presence of uncompensated magnetic moments at the tip apex (Payne, Jiang, and Bloomfield, 2006; Czerner *et al.*, 2010). The tips most commonly used for SP-STM measurements are W tips covered with magnetic materials. In particular, Fe-coated and Cr-coated W tips are in use (Bode, Getzlaff, and Wiesendanger, 1998; Yamada *et al.*, 2003; Yamasaki *et al.*, 2003; Kawagoe *et al.*, 2005). These tips are prepared by high-temperature flashing of W tips and subsequent deposition of magnetic materials onto the W tips.

b. Optically pumped GaAs

III-V compound semiconductors can produce spin-polarized electrons at their conduction band when illuminated by circularly polarized light. Thus, optically pumped GaAs is widely used as a spin-polarized electron source. This is based on the following three factors: (1) the band structures of III-V compound semiconductors, (2) the optical selection rule, where the total angular momentum of an illuminated photon and an excited electron must be conserved, and (3) the transition probability of electrons. III-V compound semiconductors have an *s*-like conduction band (the angular momentum $m_j = \pm 1/2$) and a *p*-like valence band ($m_j = \pm 3/2$ for the heavy-hole band and $m_j = \pm 1/2$ for the light-hole band) around the Γ point. The two bands are separated by the band gap ($E_g = 1.52$ eV for GaAs at 0 K). If circularly polarized light ($m_j = \pm 1$ along the beam axis) with the energy of the band gap is used, the optical selection rule allows electronic transitions with $\Delta m_j = m_f - m_i = \pm 1$, where m_f and m_i are the angular momenta of the final and initial states, respectively. For σ^+ circularly polarized light ($m_j = +1$), the following two transitions are allowed: from $m_j = -3/2$ (the heavy-hole band) to $m_j = -1/2$ (conduction band) and from $m_j = -1/2$ (the light-hole band) to $m_j = +1/2$ (conduction band). The net spin polarization of electrons excited to the conduction band is given by the relative transition probabilities of the two transitions. Pierce and Meier (1976) determined by calculating the matrix element of the transition that the relative transition probability from the heavy-hole band is 3 times larger than that from the light-hole band. This yields the result that the net spin polarization of electrons excited to the conduction band is +50% [−50% for σ^- circularly polarized light ($m_j = -1$)]. Pierce (1988) proposed SP-STM with optically pumped GaAs tips based on the principles discussed above. There have been reports on successful detection of spin-polarized current between a magnetic tip and an optically pumped GaAs sample (Alvarado and Renaud, 1992; Sueoka, Mukasa, and Hayakawa, 1993). For the reversed setup, SP-STM experiments with an optically pumped GaAs tip, results have also been reported (Kodama *et al.*, 1998; Shinohara *et al.*, 1998; Sueoka *et al.*, 2004).

c. Superconducting materials in magnetic fields

Meservey, Tedrow, and Fulde (1970) observed spin splitting (Zeeman splitting) of the quasiparticle coherence peak of superconducting Al thin films by applying an in-plane magnetic field and measuring the differential conductance of Al/Al₂O₃/Ag tunnel junctions. Using the spin-split states, the spin polarization of electrons tunneling in superconducting-ferromagnetic tunnel junctions was obtained (Tedrow and Meservey, 1971b, 1973). This technique might be exploited for SP-STM experiments by using a superconducting tip in magnetic fields. The drawback of the approach is the need for large external magnetic fields. Large fields are required to induce a sizable spin splitting of the quasiparticle density of the superconductor (Meservey, Tedrow, and Fulde, 1970). A field of 1 T induces an energy split between quasiparticle spins of P and AP orientation to the external field of ~ 0.12 meV. Thus, this method relies on the application of large magnetic fields, which certainly also impact the magnetic state of the

sample. The technique requires an energy resolution of spectroscopy well below $100 \mu\text{eV}$. Corresponding experiments with sub-K STM, using a ^3He - ^4He dilution refrigerator for cooling of the STM (Assig *et al.*, 2013), are currently under way (Ast, 2013).

2. Mode of operation

a. Constant-current mode

As outlined previously and described in Eq. (16), the tunneling current for the spin-polarized tip and sample has two components, a non-spin-polarized and a spin-polarized part. If a magnetic tip is scanned over an atomically flat magnetic surface with a constant-current mode, a difference in the apparent height of a constant-current STM image reflects a change in the spin-polarized part of the tunneling current. Thus, the constant-current STM image can reveal magnetic structures of surfaces. The first successful SP-STM measurement was performed with the constant-current mode and revealed the topological antiferromagnetism of Cr(001) (Wiesendanger *et al.*, 1990). This operation mode was also successfully applied to other systems to investigate their surface magnetic properties (Rusponi *et al.*, 2005; Hofer *et al.*, 2008). However, the morphology of surfaces greatly contributes to the difference in the apparent height of the constant-current STM image. Therefore, this operation mode is not ideal for studying larger surface areas, where there are atomic steps and islands, giving rise to a large topographic contrast. The constant-current image reflects both the energy-integrated non-spin-polarized and magnetization (spin-polarized) LDOSs [Eq. (16)]. The contribution of the spin-polarized part to the image contrast gets smaller as the bias voltage increases. The most powerful application of this operation mode is in atomic-resolution SP-STM experiments. It was believed that atomically resolved SP-STM images mainly reflect atomic structures of surfaces and only a small superimposed corrugation of magnetic origin was expected. In contrast to this expectation, Wortmann *et al.* (2001) theoretically revealed that a constant-current SP-STM image is dominated by the magnetic superstructure rather than the atomic or chemical unit cell. Indeed, constant-current mode SP-STM unveiled numerous atomic-scale spin structures (Wiesendanger *et al.*, 1992; Heinze *et al.*, 2000; Yang *et al.*, 2002; Gao, Wulfhekel, and Kirschner, 2008), even for complex spin structures such as skyrmions (Heinze *et al.*, 2011).

b. Spectroscopic mode

It had been a long-standing issue how to disentangle structural, electronic, and magnetic information in STM data. The spectroscopy technique solves this problem because the differential conductance dI/dV can be linked to the energy-resolved LDOS of the sample [Eq. (11)]. In contrast to the constant-current mode SP-STM, the spectroscopic mode offers access to the energy-resolved spin-polarized LDOS [Eq. (19)]. If a sample surface has a highly spin-polarized electronic state at the surface, a large magnetic signal in the differential conductance dI/dV can be expected around an energy where the state exists. By making use of highly spin-polarized surface states, the spectroscopic mode SP-STM revealed magnetic domain structures on various material surfaces in the area range

of subnanometer to a few hundred nanometers (Pratzer *et al.*, 2001; Ravlić *et al.*, 2003; Yamasaki *et al.*, 2003; Berbil-Bautista *et al.*, 2007). The great advantage of this mode is that energy- and spin-resolved electronic structures can be obtained and compared to results of spin-resolved photoemission spectroscopy (PES) measurements and *ab initio* spin-resolved band structure calculations. Combined studies of these complementary techniques contributed to the progress in surface nanomagnetism. A unique aspect of SP-STs is that it allows one to obtain spatially resolved maps with subnanometer resolution of spin-dependent electronic properties such as the TMR [see Eq. (31)] and the asymmetry of the differential conductance, as defined in Eq. (20). To this end, at each image pixel of the scan range, a complete spectroscopy curve of the tunneling current $I(V)$ and the differential conductance $dI/dV(V)$ is recorded for states of P and AP magnetization orientation between the tip and sample. These measurements are time intensive. A typical 200×200 pixel map with the spectroscopic data over 200 voltage points of one magnetization state takes a data collection time of roughly 20 h. These spectroscopy maps are obtained by the following sequence of steps: First the tip is stabilized at I_{stab} and V_{stab} , which is normally set to $|V| \geq 0.5 \text{ V}$. The feedback loop, which controls the tip-sample distance to keep the tunneling current constant, is opened. Then the gap voltage is swept, and simultaneously the tunneling current and the differential conductance dI/dV are measured. The differential conductance dI/dV is recorded by adding an ac modulation signal V_{mod} to the sample-bias voltage and detecting the resulting modulation of the tunneling current with a lock-in amplifier. The feedback loop is closed again, and the tip moves to the next image point, where this process is repeated. The spectroscopy data characterize $I(V)$ and $dI/dV(V)$ at a single point. These measurements can be performed at each image pixel position, resulting in a complete map of the spectroscopic properties. Examples are Figs. 12(b) and 12(c) for the discussion of spin polarization and Figs. 31(b) and 31(c) for the discussion of TMR, both on a single nanostructure with spatial resolution in the subnanometer range.

c. Differential magnetic mode

The dependence of the tunneling current on the relative magnetization orientation between tip and sample [Eq. (16)] opens the way to exploit a magnetization modulation of the tip to disentangle topographic and magnetic information in SP-STM. The concept of this operational mode was proposed by Johnson and Clarke (1990). Wulfhekel and Kirschner (1999) successfully observed magnetic domain structures of Co (0001) using this technique for the first time. The idea is to modulate the magnetization direction of a magnetically soft tip by passing an ac current through a miniature coil, surrounding the tip. The frequency of the ac current is chosen above the bandwidth of the feedback loop of the STM. A lock-in technique is used to detect the magnetic information from the ac component of the tunneling current, whereas the dc component reflects the topographic information. Needlelike tips (Wulfhekel and Kirschner, 1999) and disklike tips (Schlickum, Wulfhekel, and Kirschner, 2003) were successfully used to probe out-of-plane and in-plane magnetization

components, respectively. The drawback of this approach is that it cannot be used in external magnetic fields, which would be high enough to pin the magnetization direction of the soft magnetic tip. But the method has shown its potential in identifying noncollinear spin structures (Gao *et al.*, 2007) and inverted spin polarization near O atoms on Fe(001) (Tange *et al.*, 2010).

E. SP-STM in magnetic fields: A tool to study spin polarization

1. Experimental setup

In this section, we describe our experimental setup as an example of low-temperature STM systems for the investigation of spin-dependent phenomena at surfaces. Figure 3(a) shows a schematic drawing of the system, which is composed of three chambers separated by gate valves, the STM chamber, the preparation chamber, and the load-lock chamber. The STM chamber incorporates a cryostat, which contains two concentric tanks.² The outer tank holds liquid N₂ and the inner tank liquid He. The cryostat is equipped with a superconducting split coil magnet, which produces a magnetic field of up to 8 T, perpendicular to the sample surface. The STM head [Fig. 3(b)] is mechanically decoupled from the ultrahigh-vacuum (UHV) chambers by a spring suspension within the UHV system. Its movements are damped by eddy current damping, which works also in the presence of a strong external field of up to 8 T. The complete UHV system is supported by four air-damping legs to decouple the UHV system mechanically from the laboratory floor. The complete system is surrounded by a sound proof cabin to minimize acoustic noise influence. The lowest temperature of the STM is 7–8 K, as checked by calibrated Cernox sensors³ in proximity to the sample in the STM head. The preparation chamber is equipped with an ion gun, a sample and tip heating stage, and evaporators. This allows one to prepare the sample and tip under UHV conditions. The sample and tip [Figs. 3(d) and 3(c)] can be transferred from the preparation chamber to the STM chamber under UHV conditions with a magnetically coupled transfer tube and manipulated by wobble sticks.⁴ Sample and tip preparation under UHV conditions is mandatory for reliable and reproducible experiments under well-defined conditions. The load-lock chamber allows fast introduction and removal of sample and tip into and out of the system without breaking the vacuum of the preparation chamber within some 2 h after loading. Further details of the system are described by Wedekind (2010) and Sander *et al.* (2013). Other low-temperature STM systems with magnetic field are described by Pietzsch *et al.* (2000), Wiebe *et al.* (2004), and Zhang *et al.* (2011).

2. Characterization and control of magnetic SP-STM tips

A magnetic characterization of the tip is decisive for a reliable interpretation of SP-STM data. Rodary *et al.* (2009) demonstrated a characterization of the magnetic configuration

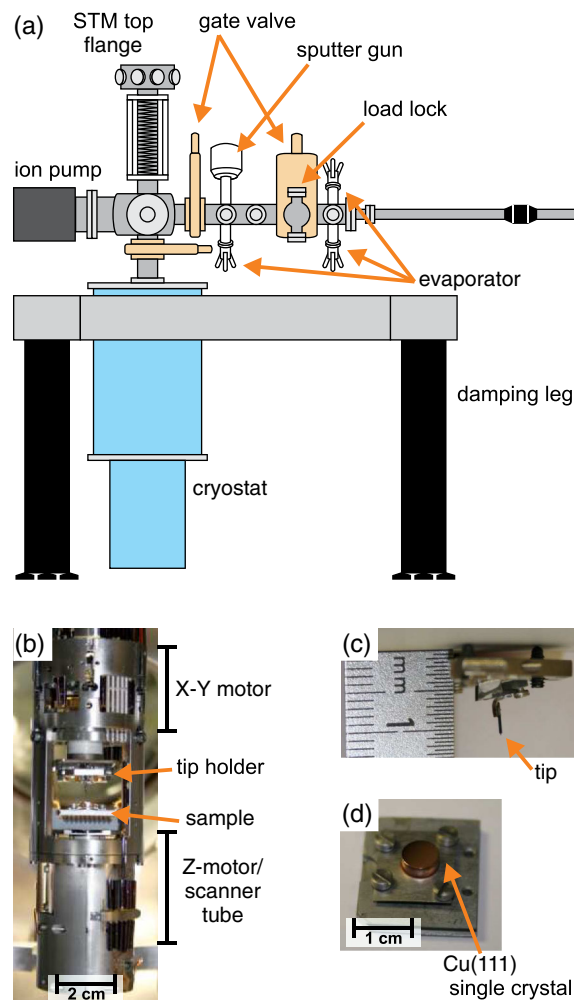


FIG. 3 (color online). Ultrahigh-vacuum system for low-temperature STM in magnetic fields. The STM is cooled by liquid N₂ and liquid He in a bath cryostat. This allows for STM measurements at 7 K in fields of up to 8 T. (a) Schematic drawing of the system. Photos of the system can be found in Wedekind (2010). (b) Head of the STM with tip and sample inserted. (c) STM tip attached on a tip holder. (d) Cu(111) single crystal mounted on a sample holder.

of SP-STM tips based on measurements in magnetic fields. Figures 4 and 5 show examples of the tip characterization. The STM image in Fig. 4(a) shows Co islands on Cu(111), which were prepared by a deposition of Co [~ 0.4 monolayers (ML)] onto a clean Cu(111) surface at room temperature (RT). Co atoms form islands with a triangular shape, 2 ML high, and different sizes (de la Figuera *et al.*, 1993). Figure 4(b) shows two differential conductance dI/dV spectra measured on a Co island A with a 40 ML Cr/40 ML Co/W tip for different magnetic fields, 0.0 T and +0.6 T. Both spectra were measured at the center of the island to exclude the effect of position-dependent electronic properties of Co islands on Cu(111) on the dI/dV signal (Pietzsch *et al.*, 2006; Rastei, Heinrich *et al.*, 2007). A characteristic feature of the dI/dV spectrum is a peak around -0.3 V, which is ascribed to a Co minority d state (Diekhöner *et al.*, 2003). Applying a magnetic field of +0.6 T drastically changes the shape of the spectrum. To understand the change of the spectra due to the magnetic

²Cryogenic SFM from Omicron NanoTechnology, www.omicron.de, and ⁴He cryostat from Janis Research, <http://www.janis.com/>.

³<http://www.lakeshore.com/Pages/Home.aspx>.

⁴<http://www.ferrovac.com/>.

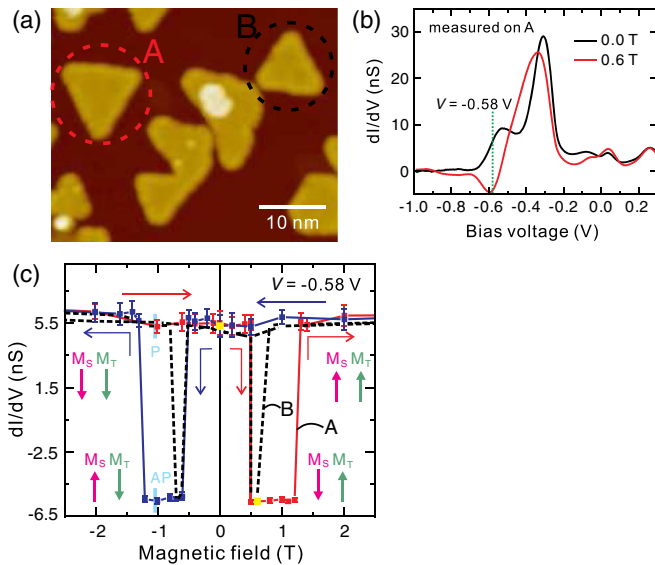


FIG. 4 (color online). Differential conductance hysteresis loops of Co islands on Cu(111) at 8 K. (a) Constant-current STM image of Co islands on Cu(111) ($V_S = -0.1$ V, $I = 1.0$ nA). (b) Differential conductance (dI/dV) spectra measured at the center of the Co island shown in (a) (dashed circle A) at different external magnetic fields, $B = 0.0$ T and $+0.6$ T ($V_{\text{stab}} = +0.5$ V, $I = 1.0$ nA). The broken line indicates the bias voltage where the corresponding dI/dV hysteresis loop of (c) was taken. (c) dI/dV hysteresis loops at the center of the Co islands marked by the dashed circles in (a) ($V = -0.58$ V). The colors correspond to upward and downward sweeps of the magnetic field, respectively. The dashed line presents a dI/dV hysteresis loop of the smaller Co island B marked by the dashed circle B in (a). The dots correspond to measurement conditions of the dI/dV spectra in (b), the markers identify the measurement conditions of the dI/dV images shown in Fig. 12 corresponding to P and AP states.

field, the differential conductance signal at -0.58 V is plotted as a function of the field in Fig. 4(c). The plot shows a clear hysteretic behavior of the signal with respect to the field. It reveals sharp signal changes at ± 0.5 and ± 1.3 T. Another measurement of a dI/dV hysteresis loop was performed on the smaller size Co island B [Fig. 4(c)]. The hysteresis loop of island B shows abrupt signal changes at ± 0.5 and ± 0.8 T. Our measurements identify four magnetic switching events. The switching event at ± 0.5 T is identical for both measurements. The easy magnetization direction of bilayer Co islands on Cu (111) at low temperature is perpendicular to the surface, and the switching field of the magnetization direction of the Co islands strongly depends on the size of the islands (Pietzsch *et al.*, 2004; Rodary *et al.*, 2008; Ouazi *et al.*, 2012). Therefore, the magnetic tip is characterized by a bistable out-of-plane magnetization, which switches at ± 0.5 T. The signal changes at ± 1.3 and ± 0.8 T are ascribed to the magnetization reversal of islands A and B, respectively. This is schematically indicated by the arrows M_S and M_T in Fig. 4(c).

Rodary *et al.* (2009) also demonstrated that the magnetic configuration of an SP-STM tip and its response to a magnetic field change for different tip apices, as shown in Fig. 5. The macroscopic preparation of the tip is the same for tips ③ and ④ in Fig. 5, but the shape of the hysteresis loop is totally different

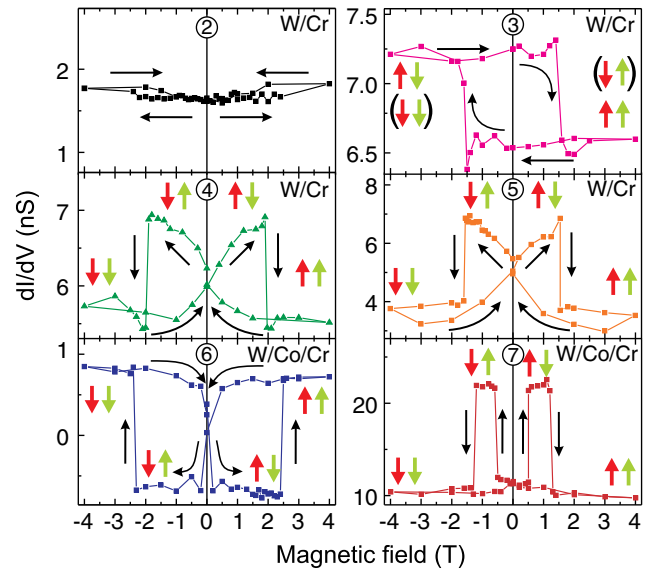


FIG. 5 (color online). Magnetic hysteresis loops measured with different tips. The thin black arrows show the sequence of data acquisition while sweeping the magnetic field. The shorter, thicker arrows represent schematically the magnetization directions of tip and sample, respectively. For loop ③, a fixed magnetization direction is found. However, its direction cannot be determined (up or down), and the two possibilities are shown. Adapted from Rodary *et al.*, 2009.

for the two tips. Tip ③ has a fixed magnetization direction of the tip apex, which does not respond to the field, and gives a magnetic signal at 0.0 T for an out-of-plane magnetized sample. In contrast, tip ④ does not provide a magnetic contrast at 0.0 T, and its magnetization direction changes with field (Rodary *et al.*, 2008). These examples indicate that field-dependent measurements are required to characterize the magnetic response of the tips reliably.

It is evident that the tip and its detailed apex configuration are central for performing reliable spin-resolved spectroscopy measurements (Phark *et al.*, 2013). Recent experiments by combined atomic force microscopy and STM offer a venue to characterize tips and their apex configurations on the atomic scale, and corresponding experiments would improve the tip characterization considerably (Welker and Giessibl, 2012).

Field-dependent measurements are also required to reliably identify parallel and antiparallel states between tip and sample magnetizations. In Fig. 4(c), the magnetization directions of the tip M_T and the Co island M_S are denoted by arrows. It is possible to control the magnetic configuration of the island with respect to the tip by applying a magnetic field to manipulate the magnetization direction of either the tip or the island. This is a necessary condition for studying the spin polarization of the sample from measurements of P and AP states, as discussed in Sec. IV.C.

The analysis of hysteresis curves of the differential conductance gives access also to the magnetic switching field of individual Co nanoislands, as discussed in greater detail by Rodary *et al.* (2008), Wedekind *et al.* (2011), Ouazi *et al.* (2012), and Sander *et al.* (2013). Thus, the magnetization reversal has been studied in dependence on island size and temperature. The analysis indicates that the reversal is

thermally assisted, and the magnetic anisotropy and the reversal mode can be derived from a quantitative data analysis (Ouazi *et al.*, 2012; Sander *et al.*, 2013). This review reveals that spin-dependent electronic properties, such as the spin polarization, vary on a nanometer scale within a single Co nanoisland. It is suspected that structural and electronic relaxations near the island rim are important aspects which drive this nonhomogeneous electronic structure. Presently, no comprehensive insight has been reached into the spatial variation of spin-dependent electronic properties on magnetism on the nanoscale. Further combined efforts by experiment and theory are called for to advance the understanding on the electronic level, where relevant properties vary on the nanometer scale (Ouazi *et al.*, 2012; Sander *et al.*, 2013).

III. CONFINEMENT OF SURFACE-STATE ELECTRONS

A. Origin of two-dimensional surface states

A crystal surface breaks the translational symmetry of the crystal structure of an infinitely extended bulk crystal. Tamm (1932) was the first to find that new electronic states appear at surfaces in energy gaps of projected bulk bands due to the translational symmetry breaking at solid surfaces. He referred to the new electronic states appearing at surfaces as “surface states.” Shockley (1939) gave for the first time physical insight into how surface states emerge from atomic orbitals as a crystal is formed by changing the lattice constant of the crystal. Shockley (1939) demonstrated that surface states appear in the gap due to a crossing of electronic bands.⁵ He also pointed out that such surface states form surface-state bands at surfaces. The surface-state band is characterized by the bulk band from which it originates. A surface state having its origin in a d bulk band makes a nondispersive electronic band in the surface Brillouin zone and is essentially localized on surface atoms. In contrast, a surface state originating from an s - p bulk band consists of nearly free s - p electrons and forms a laterally extended two-dimensional electronic band at the surface. Because of inherent surface sensitivity of the tunneling process in STM, we dominantly probe states localized in the surface layer. But also bulk states may contribute to the conductance, as discussed in Sec. III.D. For a detailed discussion of the theory of surface states and the historical development in both theory and experiment, see Davison and Stęślicka (1992) and textbooks on surface science (Zangwill, 1988).

B. Probing electronic surface states experimentally by STM

STM and STS are sensitive to the electronic LDOS at the tip position as discussed in Sec. II.B. On a real surface there are always steps, point defects, dislocations, and adsorbates. Also the structure of a surface can be modified on the nanometer scale by STM. An indentation of an STM tip into a single-crystal surface can artificially create long and straight step edges and nanostructures separated by those step edges (Jeandupeux *et al.*,

1999). These deviations from the ideal surface induce corresponding spatial modulations of the LDOS.

Figure 6(a) shows an STM image of a Cu(111) surface with a straight step edge, which was created by indentation of the STM tip on purpose. Since the image was acquired at a gap voltage of +0.02 V, it reflects a map of the surface LDOS around E_F . Spatial oscillations of the surface LDOS are clearly seen on the upper terrace near the step edge and extend beyond the scanning area. Note that the terrace extends for more than 100 nm from the step edge. Crommie, Lutz, and Eigler (1993b) observed for the first time spatial oscillations of the surface LDOS on a Cu(111) surface at 4 K using STM. Hasegawa and Avouris (1993) also found similar oscillations of the surface LDOS on a Au(111) surface at room temperature. The spatial oscillations of the surface LDOS were interpreted in terms of scattering of surface-state electrons off the step edges.

On noble metal (111) surfaces, Shockley surface states appear in a gap of projected bulk bands along the Γ - L line. Electrons of the surface states are localized near the surface because their DOS decays exponentially both into the vacuum and into the bulk. However, they behave like free electrons parallel to the surface and form a two-dimensional electron gas. Thus the dispersion relation can be described approximately for the two-dimensional surface-state band as

$$E(k_{\parallel}) = E_0 + \frac{\hbar^2}{2m^*} k_{\parallel}^2, \quad (22)$$

where E_0 is the energy of the surface-state bottom, m^* is the effective mass of a surface-state electron, and k_{\parallel} is the wave vector parallel to the surface. PES experimentally revealed the existence of such surface states on noble metal (111) surfaces (Gartland, Berge, and Slagsvold, 1973; Heimann, Neddermeyer, and Roloff, 1977). Angle-resolved PES (ARPES) demonstrated that the band structure of the surface states can be described by Eq. (22) (Gartland and Slagsvold, 1975; Kevan, 1983; Goldmann, Dose, and Borstel, 1985; Kevan and Gaylord, 1987; Reinert *et al.*, 2001).

When a surface has a defect, electrons of the surface states are expected to scatter off the defect. Electron waves incident to a defect interfere with those reflected at the defect, forming standing waves in the surface LDOS. The spatial oscillations observed in Fig. 6(a) can be viewed as standing waves, originating from quantum interference of electron waves of surface states of the Cu(111).

As discussed in Sec. II.B, the tunneling current at a sample-bias voltage of V reflects the surface LDOS integrated between E_F and $E_F + eV$, whereas the differential conductance dI/dV measured at a sample-bias voltage of V gives a measure of the surface LDOS at $E_F + eV$. Thus, measuring the differential conductance dI/dV and its spatial mapping is more appropriate for exploring surface electronic properties in detail, as compared to a spatial mapping of the tunneling current in a constant-current STM image. A differential conductance dI/dV map obtained on the same area of Fig. 6(a) at +0.02 V shows clear spatial oscillations of the surface LDOS [Fig. 6(b)]. Based on the assumption that a step edge acts as a hard wall potential barrier, which surface-state

⁵Zak (1984, 1985) showed that the existence of Shockley surface states is determined by the symmetry of the electronic band only and, thus, the band crossing is not always necessary for formation of Shockley surface states.

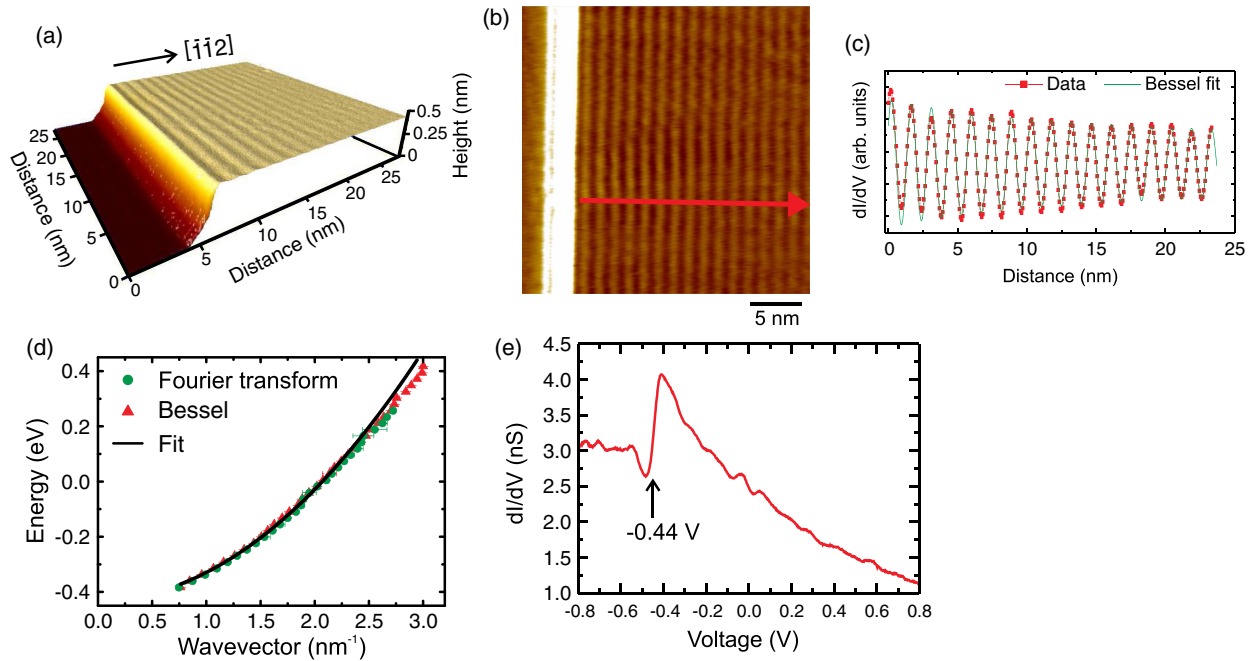


FIG. 6 (color online). Observation of standing waves near a step on Cu(111) by STM and STS. (a) A three-dimensional (3D) view of a constant-current STM image of the step edge of Cu(111). $I = 1.0$ nA, $V = +0.02$ V, 28×28 nm². (b) Differential conductance (dI/dV) map of the step edge simultaneously measured with the STM image in (a). (c) Line profile of the dI/dV map along the arrow in (b), showing a spatial oscillation of the dI/dV signal. (d) Dispersion relation of electronic states forming standing waves in dI/dV maps taken at different energies. The data points are extracted by a Fourier transform of the differential conductance map and a Bessel-function fit [Eq. (24)] in (c). The data points are compared to a parabolic fit [Eq. (22)]. (e) dI/dV spectrum measured on Cu(111) in a region of negligible spatial modulation.

electrons cannot penetrate, the LDOS of the surface states around the step edge is given by

$$\text{LDOS}(E, x) = \frac{2}{\pi^2} \sqrt{\frac{2m^*}{\hbar^2 E}} \int_0^{k_0} dk \frac{\sin^2(kx)}{\sqrt{1 - (k/k_0)^2}}, \quad (23)$$

where E is the energy of an electron with respect to the surface-state band bottom, x is the distance from the step edge, and $k_0 = \sqrt{2m^*E/\hbar^2}$. An analytical solution of the integral in Eq. (23) gives

$$\text{LDOS}(E, x) = [1 - J_0(2k_0x)]L_0, \quad (24)$$

where J_0 is the zeroth-order Bessel function and $L_0 = m^*/\pi\hbar^2$ is the LDOS of the surface states without any defect (Davis *et al.*, 1991; Crommie, Lutz, and Eigler, 1993b). Fitting Eq. (24) to a line profile of the differential conductance dI/dV map yields a wave vector representing the standing waves at $+0.02$ V [Fig. 6(c)]. The result for $E = +0.02$ eV is $k_0 = 2.14$ nm⁻¹. This procedure can be performed for data obtained at different energies to get the dispersion relation $E(k)$ of the surface states, shown in Fig. 6(d). The dispersion relation reveals that the wave vector continuously increases with energy, approximately following a parabolic dependence. This is expected for the two-dimensional surface-state electrons from both theoretical and experimental results. The solid line in Fig. 6(d) is a fit of Eq. (22) to the data points, yielding $E_0 = -0.44 \pm 0.01$ eV and $m^* = 0.38m_e$, where m_e is the free-electron mass, which are in excellent agreement with the values obtained from PES on Cu(111) (Kevan and Gaylord,

1987; Reinert *et al.*, 2001). Limitations of this parabolic dispersion model for larger energies (Bürgi, Petersen *et al.*, 2000; Ünal *et al.*, 2011) are discussed next.

Figure 6(e) shows a dI/dV spectrum measured on a flat terrace of a Cu(111) surface. A sharp increase of the differential conductance dI/dV signal at -0.44 V can be seen in the spectrum. On a Cu(111) surface Crommie, Lutz, and Eigler (1993b) found a sharp increase of the differential conductance dI/dV signal at -0.45 V and explained this increase as electrons tunneling from the occupied surface state of Cu(111) into empty states of the tip. Therefore, such a sharp increase of the dI/dV signal is recognized as the onset of the two-dimensional surface-state band of the noble metal (111) surfaces (Everson, Jaklevic, and Shen, 1990). The energy where the sharp increase is measured by STM is in good agreement with that of the surface-state band bottom E_0 obtained with PES. Note that E_0 is usually lower by some 5–10 meV in STS measurements than in PES measurements because the electric field induced by the presence of an STM tip affects the surface electronic structure, via the so-called Stark effect (Becker, Golovchenko, and Swartzentruber, 1985; Binnig *et al.*, 1985; Limot *et al.*, 2003; Kröger *et al.*, 2004). It was reported that E_0 shifts downward in energy by a few meV under tunneling conditions with a bias voltage of some hundred mV and a tunneling current in the range of nA, which reflect normal settings used for STM and STS measurements (Limot *et al.*, 2003; Kröger *et al.*, 2004).

The spatial oscillation of the LDOS is also observed on the lower terrace near a step edge. But the amplitude of the oscillation is always smaller on the lower terrace than

on the upper terrace, indicating different scattering properties of steps for the upper and lower terraces near the step (Crommie, Lutz, and Eigler, 1993b; Hasegawa and Avouris, 1993). Crommie, Lutz, and Eigler (1993b) and (Hasegawa and Avouris (1993) also clearly showed a damping of the spatial oscillation of the LDOS away from step edges, implying the loss of phase coherency of surface-state electrons. A detailed analysis of the spatial oscillation of the LDOS revealed not only the dispersion relation of two-dimensional surface states, but also the reflection coefficient of steps and the phase coherence length of surface-state electrons (Bürigi *et al.*, 1999; Jeandupeux *et al.*, 1999; Bürigi, Brune *et al.*, 2000; Vitali *et al.*, 2003).

A careful inspection of the data in Fig. 6(d) reveals that data points for energies larger than +0.3 eV deviate from the parabolic behavior of Eq. (22) (solid line). Bürigi, Petersen *et al.* (2000) accounted for the trend of the deviation from the parabolic behavior by means of a simple tight-binding model. Recently, a combined study of multiphoton PES with a momentum microscopy (Krömker *et al.*, 2008), STM, STS, and first-principle calculations identified the deviation as a consequence of the strong hybridization between the surface states and bulk states with increasing energy, as illustrated in Fig. 7 (Ünal *et al.*, 2011).

C. Examples of electron confinement involving surface-state electrons

When electrons are confined to structures with size comparable to the de Broglie wavelength, i.e., lateral dimensions in the nanometer range, quantum-size effects become obvious and are observed in STM studies.

1. Stripes

The simplest example of electron confinement is a stripe structure separated by two straight and parallel steps. Avouris and Lyo (1994) reported for the first time electron confinement in a narrow Au(111) terrace with a 36 Å width separated by monatomic steps at room temperature. Their results nicely demonstrated that surface-state electrons are confined to the terrace along the terrace width, and this results in the quantization of the wave vector of the electrons. We explain the effect in the following for a monatomic high stripe on Cu(111).

Figure 8(a) shows an STM image of a stripe structure, created on a Cu(111) surface by tip indentation. All measurements were performed at 7 K. The stripe has a monatomic height of 0.2 nm, and a width of 8.9 nm, corresponding to 40 atomic rows. It runs along the Cu[1 $\bar{1}$ 0] direction, and the stripe edges correspond to {100} facets. Spatial oscillations are clearly observed in a dI/dV image of the stripe, and they are ascribed to modulations of the LDOS. The pronounced spatial oscillation is the signature of electron confinement. To investigate the electronic structure within the stripe in detail, the differential conductance signal is plotted as functions of the position perpendicular to the steps (the x axis) and of the energy (the y axis) in Fig. 8(b). There is no clear spatial modulation of the LDOS below -0.45 eV.

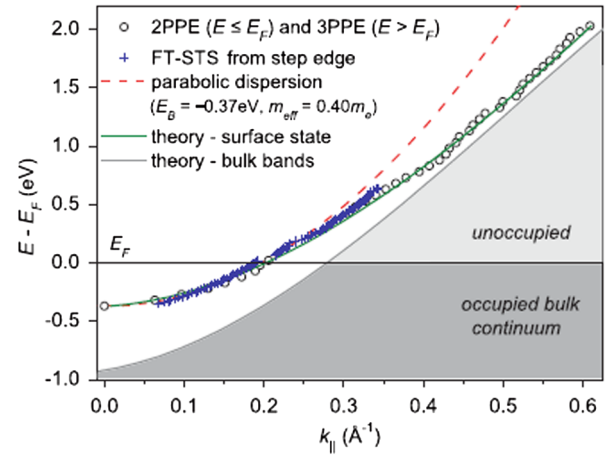


FIG. 7 (color online). Dispersion of the surface state of Cu(111) in the bulk band gap obtained by multiphoton photoemission (mPPE), Fourier transform (FT) STS, and theory along the $\Gamma\bar{M}$ direction. The solid lines display the calculated dispersion of the surface state and the bulk band edge. The experimental results are compared to the model of a quasi-free-electron-like parabolic dispersion (dashed curve). A deviation from the parabolic dispersion is apparent at higher energies above +0.1 eV. From Ünal *et al.*, 2011.

This reflects the energy position of the surface-state band bottom. A spatial modulation of the LDOS appears first at -0.45 eV and has a peak at the center of the stripe. The modulation evolves and shows more structures as the energy increases. It changes into a pattern with two maxima around -0.39 eV, and then into a pattern with three maxima around -0.32 eV. In contrast to the case of standing waves at a step edge discussed previously, the spatial modulation of the LDOS does not change continuously, but discretely with energy. This is a characteristic of quantum electron confinement. The confinement can be described by a one-dimensional particle-in-a-box model.

Figures 8(c) and 8(d) schematically explain the model. We approximate the confinement in the Cu stripe by a one-dimensional particle-in-a-box model with infinitely high potential barriers. Although this is a crude model, it reflects important aspects of the experiment well. We note that the applied free-electron model with parabolic dispersion cannot describe the experimental results properly at higher energies, as discussed previously. When a free electron is confined to an infinite potential quantum well, the wavelength of the electron, λ , is restricted to specific values because the wave function of the electron, ψ , must vanish at the infinite potential walls,

$$d = \frac{\lambda}{2} n = \frac{\pi}{k} n, \quad (25)$$

where n are positive integers and d is the width of the quantum well. Our quantitative analysis shows that the confinement length d reflects the width of the stripe at half height, as deduced from a line scan in a constant-current STM image [Fig. 8(a)]. This restriction of the electron wavelength leads to discrete energy levels, and we get from the dispersion relation of a free electron Eq. (22),

$$E = E_0 + \frac{\hbar^2}{2m^*} k^2 = E_0 + \frac{\pi^2 \hbar^2}{2m^* d^2} n^2. \quad (26)$$

The wave functions for $n = 1-5$ are schematically sketched in Fig. 8(d). The energy positions of the states reflect the discrete energy levels of Eq. (26).

The differential conductance signal measured by STM is related to the LDOS of the sample [Eq. (11)], and the LDOS of the sample scales with the probability density $|\psi|^2$ [Eq. (6)]. Therefore, the probability densities corresponding to the $n = 1-5$ wave functions are also depicted in Fig. 8(c). The probability density is not constant within the quantum well but spatially modulated. The $n = 1$ state has a peak in the middle of the quantum well and the $n = 2$ state has two peaks. Higher (n th) states have more peaks (n peaks) in the probability density within the quantum well. This behavior is identical to the experimental result in Fig. 8(b). Thus the surface-state electrons within the stripe structure can be approximated by a free electron in an infinite potential quantum well.

To extract the wave vector k responsible for the modulation of the LDOS, a Fourier transform (FT) of the differential conductance image within the stripe structure is performed.⁶ Figure 8(e) shows a map of FT power spectrum obtained from an image taken at -0.3 V. The FT map clearly indicates the wave vector producing the spatial modulation of the LDOS. The same procedure is repeated for every image as a function of energy, and the dispersion relation $E(k)$ is obtained [Fig. 8(f)]. The data points reflect discrete k values. This is in contrast to the dispersion relation obtained at a step edge [Fig. 6(d)], which shows a continuous change of the wave vector with energy. The continuous line in Fig. 8(f) is a fitting of a parabola [Eq. (22)] to the data points of energies smaller than $+0.1$ eV. A deviation from the parabolic dispersion, indicative of free electron behavior, is apparent and the reasons for this deviation have been discussed in view of hybridization with bulk states above. The parabola fit gives $m^* = 0.40m_e$ and $E_0 = -0.43$ eV, in good agreement with the values obtained from PES on Cu(111) (Kevan and Gaylord, 1987; Reinert *et al.*, 2001) and obtained from STM measurements at a step edge on Cu(111) (see Sec. III.B). The inset of Fig. 8(f) shows wave vectors as a function of the quantum number n revealing a clear quantization of the wave vector. The slope of the linear fit to the data points yields a width of the “quantum well” $d = 8.2$ nm. This

value is in good agreement with a width at half height of the stripe extracted from STM measurements, 8.9 nm, in view of tip-convolution effects (Kröger *et al.*, 2005) and possible variations of the electronic structure of the stripe in proximity to its edge (Wedekind, 2010).

Following Eq. (26), the linewidth of the discrete energy levels should be infinitely sharp. However, the experimental results above reveal a rather broad linewidth. This can be seen in Fig. 8(b), for example, the $n = 4$ state exists in an energy range from -0.11 to -0.23 eV. This broadening is ascribed to the fact that the surface-state electrons form a two-dimensional gas, and in the direction parallel to the steps the electrons are not confined but can move freely (Avouris and Lyo, 1994). The wave vector for movement perpendicular to the steps k_x is quantized, as discussed previously. However, the wave vector parallel to the steps k_y can change continuously with energy. Therefore, specific wave vectors perpendicular to the steps can be obtained over a wider energy range because the following is always fulfilled for $E \geq E_n$:

$$k_{xn} = \sqrt{k_{\parallel}^2 - k_y^2}, \quad (27)$$

where E_n is the n th discrete energy level and k_{xn} is the n th wave vector, both of which result from the confinement effect in the direction perpendicular to the steps. However, the density of states of the system follows a $1/\sqrt{E - E_n}$ decay. Thus, clear discrete states are observed in the STM and STS measurements of the stripe structure, but these states are broadened in energy. This is analogous to the behavior of free electrons confined to a quantum nanowire (Davies, 1997).

2. Stepped surfaces

If a single crystal of copper is cut at a small angle with respect to the (111) surface plane, its surface consists of (111) terraces periodically separated by monatomic steps, a situation known as a vicinal or stepped surface. The terrace width is determined by the miscut angle; for example, a miscut angle of 5.7° along an azimuth of $[\bar{1} \bar{1} 2]$ to the (111) plane of Cu, which corresponds to a Cu(554) surface, leads to a terrace width of 21 Å or nine atomic rows. This type of surface brings an additional periodicity in the direction perpendicular to the step array to crystal surfaces.

Two-dimensional surface-state electrons can still move freely in the direction parallel to steps but their behavior in the direction perpendicular to steps changes due to the step array. We saw previously that a single stripe structure separated by two parallel and straight steps confines surface-state electrons, and the dispersion relation of the surface state is not continuous but quantized, where atomic steps act as potential walls (Avouris and Lyo, 1994; Bürgi *et al.*, 1998). However, PES measurements on stepped Cu surfaces demonstrated that the dispersion relation perpendicular to steps shows a continuous parabolic curve and its umklapp replica in the surface Brillouin zone, which is defined by the periodicity of the step array. This indicates that atomic steps on stepped surfaces behave like a transparent potential, leading to a coherent coupling of the two-dimensional surface state between terraces and the formation of Bloch states. Furthermore, PES revealed that the character of the surface

⁶This is the so-called FT-STM method. Sprunger *et al.* (1997) developed this method and applied it for the first time for Be(0001) surfaces. They performed a two-dimensional FT of a constant-current STM image at $+4$ mV, and obtained a Fermi contour of a Be(0001) surface state in the power spectrum of the two-dimensional FT. This method was applied also for Au(111) and Cu(111) (Petersen, Laitenberger *et al.*, 1998; Petersen, Sprunger *et al.*, 1998), which is briefly reviewed in Sec. III.D. In these pioneering papers, a FT was performed for constant-current STM images [see Petersen *et al.* (2000) for a review]. Song *et al.* (2001) and Diekhöner *et al.* (2003) performed a FT for differential conductance maps to investigate the dispersion relation of surface states. Recently, FT-STM has been frequently used for high- T_c superconductors to investigate the pairing order parameter through the observation of quasiparticle interferences (Hoffman *et al.*, 2002; McElroy *et al.*, 2003; Hanaguri *et al.*, 2010). The following reviews are devoted to STM and STS studies on cuprates (Fischer *et al.*, 2007) and Fe-based superconductors (Hoffman, 2011).

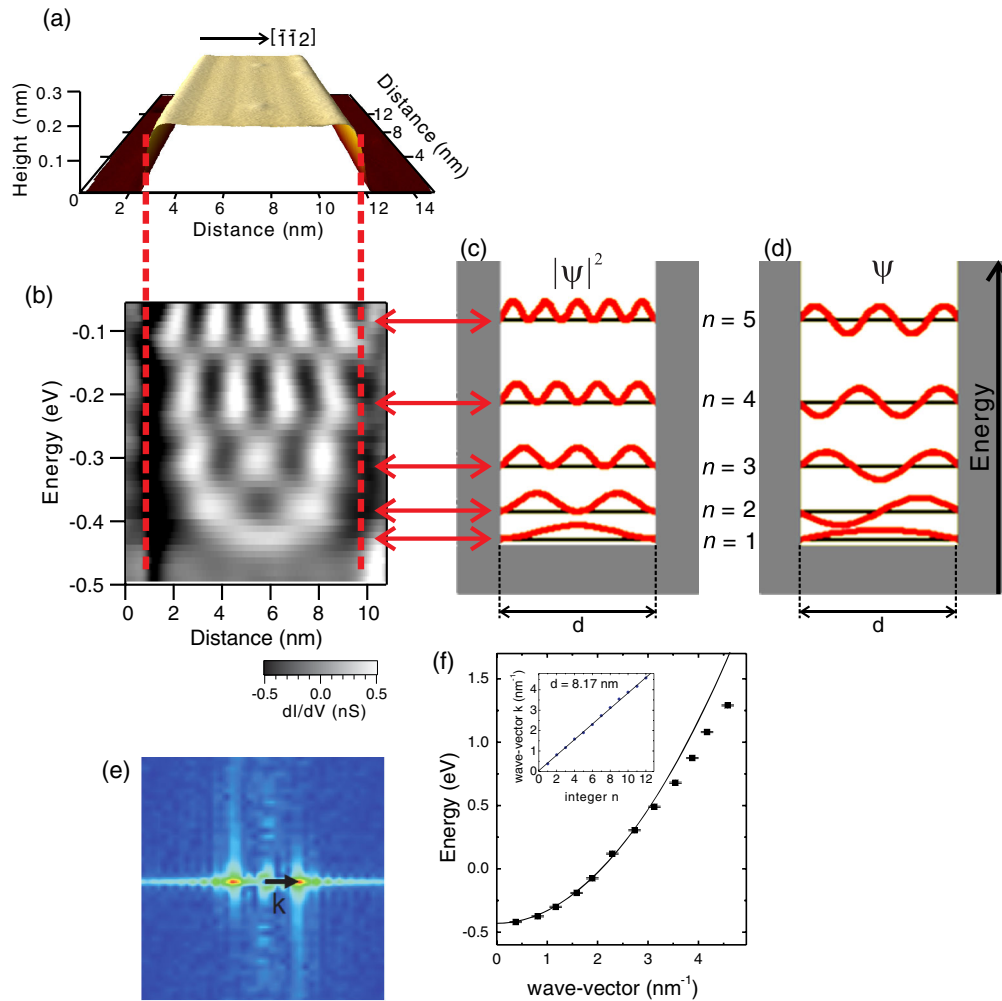


FIG. 8 (color online). Electron confinement for a monatomic-high stripe structure on Cu(111). (a) A 3D view of an STM image of the Cu stripe. Scan size: $15 \times 15 \text{ nm}^2$. (b) Differential conductance as a function of the energy and the position in the Cu stripe. The dashed lines show the edges of the stripe of (a). Schematics of a “particle-in-a-box” model for (c) the probability density $|\psi|^2$ and (d) the wave function ψ . The arrows indicate the mode assignment n_i for the different energies shown in (b). (e) Fourier transform map of the wave pattern taken at -0.3 V . (f) Dispersion relation of the electronic states, where the wave vector k has been extracted from the Fourier analysis. The continuous line is a parabolic function with $m^* = 0.40m_e$ and $E_0 = -0.43 \text{ eV}$. Note that only discrete k values are observed, which obey the quantization rule $k_n = n\pi/d$. The inset shows the k_n vs n relation. A linear fit $k = n\pi/d$ indicates $d = 8.2 \text{ nm}$. Adapted from Wedekind, 2010.

state switches from confined states to propagating Bloch states as the terrace width decreases (Ortega *et al.*, 2000, 2002; Baumberger *et al.*, 2004). The critical terrace width was found to be $16\text{--}17 \text{ \AA}$ for stepped Cu(111) surfaces (Ortega *et al.*, 2000; Baumberger *et al.*, 2004). This crossover was interpreted by considering an overlap of the surface state with projected bulk states. With decreasing terrace width or increasing miscut angle, the bulk projected band gap at $\bar{\Gamma}$ shrinks and the overlap between the surface state and projected bulk states increases. When the gap of the bulk bands vanishes the surface state turns into a resonance state. Whereas the surface state within the gap experiences atomic steps as a strong barrier potential and is confined to a terrace by steps, the resonance state sees the step as a low effective potential, and electrons can propagate across a step and form Bloch states. Indeed, the analysis of data with a Kronig-Penney model indicates that the step barrier strength

is reduced as the terrace width becomes smaller (Ortega *et al.*, 2005). Ignatiev *et al.* (2007) performed *ab initio* calculations of surface states on stepped Cu(111) surfaces and found an indication of the coupling between surface and bulk states.

Hansmann *et al.* (2003) performed STM and STS measurements on stepped Cu surfaces, Cu(554) surfaces, and found the following: (1) The surface-state band bottom shifts upward in energy. The value of this energy shift does not depend on the local terrace width. (2) A broad but clear peak appears in the differential conductance and its energy position changes with the local terrace width. The first finding was ascribed to formation of Bloch states and the second one to surface states confined to a terrace by steps. Interestingly, the two features were observed even on the same terrace, revealing the coexistence of the Bloch and confined states. They pointed out that the lowest quantized state is at the Fermi energy for stepped Cu(111) surfaces with a terrace width of

17 Å, where the crossover between the two characters of electronic states, Bloch versus surface states, was found. This means that for surfaces with a terrace width narrower than this critical value of 17 Å, there is no confined state below the Fermi level. This might be a reason why PES measurements did not show any feature of confined states for surfaces with narrower terrace widths. Very recently *Ortega et al.* (2013) found by PES that Bloch states still exist on stepped Ag(111) and Au(111) surfaces with a terrace width larger than 100 Å. Therefore, it was concluded that there is no clear transition of surface-state characters. The question as to why both Bloch and confined states can coexist or why atomic steps act differently for the two states still remains to be solved.

3. Islands and vacancy islands

The morphology of metal deposits on a substrate can be tuned by the selection of the proper growth parameters such as temperature and rate of deposition to produce well-ordered low-dimensional nanostructures (*Brune, 1998; Michely and Krug, 2004*). These nanostructures serve as model systems for electron confinement, and examples include hexagonal Ag(111) islands on polycrystalline silver (*Avouris and Lyo, 1994; Avouris et al., 1994*). They observed a standing wave pattern in a map of the differential conductance obtained on an island at an energy of ~ 110 meV above the bottom of the Ag(111) surface state. By modeling the hexagonal island as a two-dimensional circular box, they found that the observed standing wave pattern can be described as a superposition of two eigenstates, which result from confinement of surface-state electrons to the island boundary (*Avouris and Lyo, 1994; Avouris et al., 1994*). However, the evolution of the standing wave pattern with energy was not investigated.

A more systematic study of electron confinement to nanoislands was performed on hexagonal Ag islands on Ag(111) using low-temperature STM (*Li, Schneider, Berndt, and Crampin, 1998; Li et al., 1999*). It was demonstrated that the standing wave pattern observed on a Ag island changes with energy, starting with a single peak at the center of the island and changing into multiple hexagonal-shaped rings. Calculated LDOS maps of electronic states confined to a hexagonal potential well show qualitative agreement with experiments. It was found that the experimentally observed standing wave patterns do not correspond to individual eigenstates, but reflect superpositions of some eigenstates due to intrinsic and thermal broadening and small separations of eigenstates in energy. The term “lossy” reflects the fact that electrons might be scattered out of surface states into bulk states.

The effects of electron energy, vacancy island size, step reflectivity, and phase coherence length on the lifetime of surface-state electrons have been examined on hexagonal and triangular vacancy islands on a Ag(111) surface (*Crampin, Jensen et al., 2005; Jensen et al., 2005; Kröger et al., 2005*). Lossy scattering has been proposed as the dominant factor limiting the surface-state lifetime.

A combined study of STM and STS and *ab initio* based theory has been performed to investigate electron confinement in hexagonal, monolayer-deep vacancy islands on Cu(111) (*Niebergall, Rodary et al., 2006*). In the calculation, a

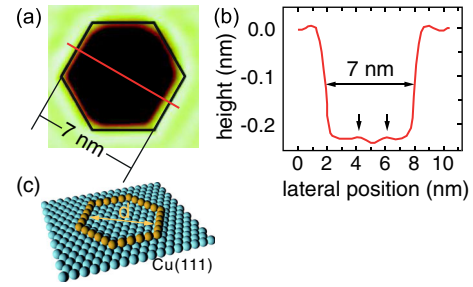


FIG. 9 (color online). Modeling a hexagonal vacancy island on Cu(111) for *ab initio* calculations. (a) STM image of a hexagonal vacancy island on Cu(111). ($V = -0.02$ V, $I = 0.5$ nA). (b) Three line scans along the lines in (a). The line scans reveal the monolayer-deep depression (0.21 nm) and two apparent modulations (arrows) due to the impact of the electron standing waves on the topographic image. The depression has a size of $d = 7$ nm. (c) A corral of Cu adatoms on Cu(111). The same size d as the depression is used in the calculations to model the vacancy island of (a). From *Niebergall, Rodary et al., 2006*.

hexagonal vacancy island is modeled as a corral of Cu adatoms on Cu(111). The size of the corral is the same size d as the diameter of the vacancy island, as extracted from STM topographic measurements (Fig. 9). The study reveals that *ab initio* based theory can reliably reproduce the spatial modulation of the LDOS, its size and energy dependence, and the energy width of confined states measured by STM and STS (Fig. 10). The theory did not include electron-electron and electron-phonon interactions but it takes scattering of surface-state electrons into bulk states into account. The good

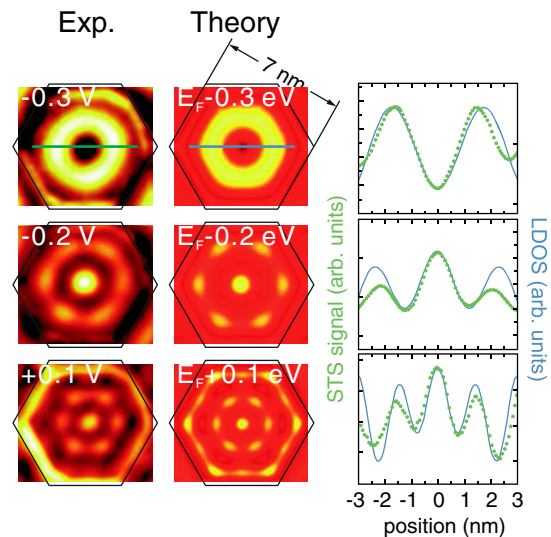


FIG. 10 (color online). Comparison of experimental maps of differential conductance of a hexagonal vacancy island with calculated LDOS maps of a corral structure. (Left column) dI/dV images of the hexagonal vacancy island in Fig. 9(a) at the indicated sample-bias voltage at 1 nA. The solid hexagon indicates the vacancy island rim. (Center column) Calculated LDOS maps of the corral structure in Fig. 9(c) at various energies. (Right column) Line scans passing through the center of the vacancy island and the corral structure. Dotted line: experiment; solid line: calculation. From *Niebergall, Rodary et al., 2006*.

agreement between experiment and theory in the energy width of confined states implies that the inelastic decay processes are not the decisive factors that broaden the energy width of the states on Cu(111) at 7 K.

Since this lossy scattering greatly contributes to the energy width of confined states, the intrinsic energy width, which is indicative of the intrinsic lifetime, is hidden. Tournier-Colletta *et al.* (2010, 2011) performed STM and STS measurements on Ag pyramidal nanostructures with a height of 4–5 ML. The geometry of the pyramidal nanostructures reduces the scattering of surface-state electrons into bulk states and shows a large reflection coefficient for the electrons. They found that the electron-phonon coupling dominantly contributes to the energy width of confined surface states around the Fermi energy, which agrees with PES measurements (Eiguren *et al.*, 2002) and theory (Eiguren *et al.*, 2003).

Rodary *et al.* (2007) exploited the FT to analyze standing wave patterns in maps of the differential conductance measured on hexagonal vacancy islands on Cu(111). A corresponding map of a hexagonal vacancy island obtained at -0.16 V [Fig. 11(a)] clearly shows spatial modulation of the LDOS. A FT of the spatial modulation inside the hexagonal vacancy was performed. In a map of the FT [Fig. 11(b)], six maxima, separated by 60° along the azimuthal direction, are observed. These maxima correspond to wave vectors that form the spatial modulation of the LDOS observed in Fig. 11(a). This FT analysis was applied to differential conductance maps of the same hexagonal vacancy for different energies. By plotting the wave vectors as extracted from the FT analysis as a function of energy, they obtained the dispersion relation [Fig. 11(c)]. The dispersion relation shows a discontinuous change of the wave vector with energy as a consequence of the

electron confinement. Surprisingly, the discrete wave vectors can be described by the one-dimensional quantization rule $k_n = n\pi/d$, where n is an integer and d is the vacancy diameter at half depth, even for this two-dimensional system. Figure 11(d) shows the result for two different vacancy islands with sizes of 20.5 and 13.5 nm, which are extracted from STM images. The slope of the curve, π/d , gives the vacancy size. The curves in Fig. 11(d) give sizes of 20.1 and 12.8 nm, respectively, in good agreement with the sizes from STM measurements as defined as the diameter at half depth in constant-current STM images. They concluded that electron confinement can be properly ascribed to scattering off parallel straight edges of the hexagonal vacancy island at a distance d .

D. Electron confinement without surface states

Up to this point we have seen quantum interference and confinement effects of Shockley *s-p* surface states on noble metal (111) surfaces. Here we point out that bulklike electronic states may also lead to electron confinement and quantum interference.

Petersen, Laitenberger *et al.* (1998) reported quantum interferences not only for surface-state electrons but also for bulk electrons near step edges and point defects on Au (111) and Cu(111). FT-STM images were extracted by performing a two-dimensional FT of constant-current STM images measured on Au(111) and Cu(111) around the Fermi energy. The FT-STM images showed two concentric circles around the $\bar{\Gamma}$ point in k space of the surface Brillouin zone. This implies that two electronic states with slightly different wave vectors [$k_{\text{inner}} = 0.166^{-1}$ and $k_{\text{outer}} = 0.21^{-1}$ for Au(111)] were involved in the formation of the standing waves.

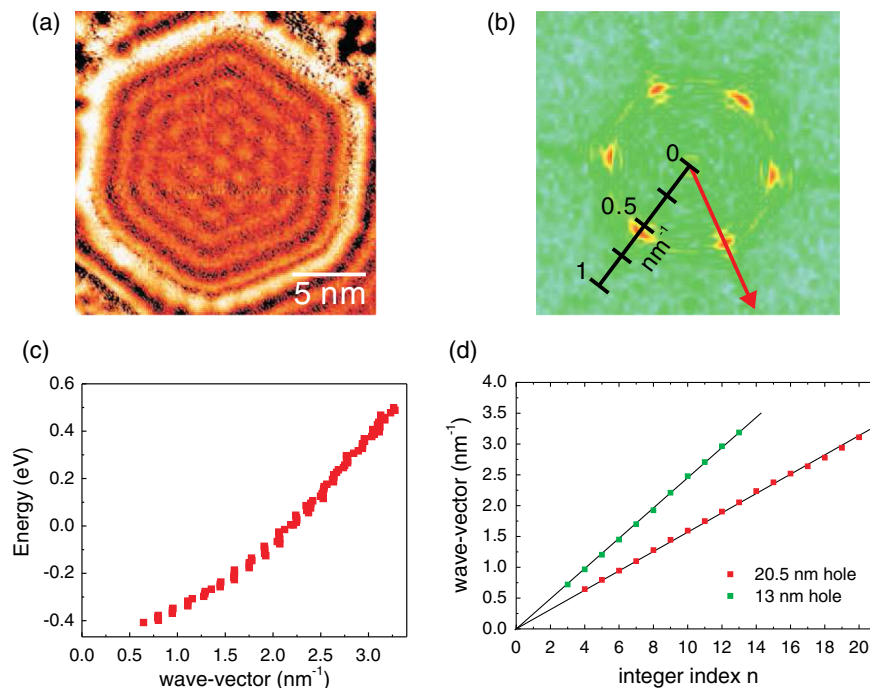


FIG. 11 (color online). Confinement of surface-state electrons by a 20 nm hexagonal vacancy island. (a) Differential conductance (dI/dV) map of the hexagonal vacancy island of 20 nm size. ($V = -0.16$ V, $I = 1.0$ nA). (b) Map of the Fourier transform of the dI/dV map in (a). (c) Dispersion relation obtained by the FT analysis of the dI/dV maps. (d) Quantization rule followed by the wave vector k . The line is a fit using $k = n\pi/d$ with $d = 20.1$ nm. Adapted from Rodary *et al.*, 2007.

The analysis of the data revealed that the inner circle can be ascribed to a Shockley surface state and the outer one to a bulk state at the “neck” of the bulk Fermi surface. To see the role of the surface and bulk states in the formation of standing waves or the screening of defects, an inverse FT was performed for modified FT-STM images in which either the inner or the outer circle in the original FT-STM image was removed. A comparison with the original STM images demonstrated that bulk electrons do not have a significant contribution to the formation of standing waves at step edges. Similar experiments (Schouteden, Lievens, and Van Haesendonck, 2009) revealed that both surface- and bulk-state electrons scatter off the same (sub)surface point defects, and found in their quantum interference patterns that bulk-state electrons decay over a shorter distance than surface-state electrons. This finding was interpreted by considering the dimensionality of the states. In general, the amplitude of so-called Friedel oscillations, which describe charge density variations (Friedel, 1958), decays on a shorter length scale in a three-dimensional system than in a two-dimensional system.

Pascual *et al.* (2006) observed quantum confinement of bulk electrons on Ag(110). Ag(110) surfaces have projected bulk bands around $\bar{\Gamma}$ and a band gap centered at the surface Brillouin zone boundary at \bar{Y} . Two surface states exist in the band gap: One is a surface state S_2 at +1.7 eV above the Fermi energy at the \bar{Y} point, which disperses upward in energy toward $\bar{\Gamma}$. The other state S_3 starts at -50 meV below the Fermi energy at the \bar{Y} point, and it disperses upward in energy toward $\bar{\Gamma}$, but crosses the bulk band edge around +200 meV above the Fermi energy and turns into a bulk state. There is no surface state, but only bulk states in the energy range between +200 meV and +1.7 eV. They observed spatial oscillations of the differential conductance exactly in this energy range. Their density functional calculations revealed that the density of bulk states near a surface is strongly enhanced at the band edge of projected bulk bands due to band curvature in a three-dimensional description of the band structure. Therefore, the bulk band topology can be investigated by detecting and analyzing quantum interference patterns formed by bulk electrons. Indeed, a bulk band edge of the Au(111) surface was observed (Didiot *et al.*, 2010).

Another example of electron quantum interference without (crystal-induced) surface states was given by Wahl *et al.* (2003). Electrons brought to a metallic surface are bound in a potential well formed by the Coulomb-like attractive image potential and the repulsive surface potential, and form hydrogenlike states, so-called image-potential states (IPSs). Electrons of IPSs are localized at distinct distances perpendicular to the surface, but can move freely parallel to the surface. Wahl *et al.* (2003) observed for the first time quantum interference of IPS electrons⁷ at step edges of Cu (100). The analysis of quantum interference patterns obtained at different energies yielded the dispersion relation of the $n = 1$ IPS, which was described by a parabola in a two-dimensional free-electron model. They extracted the phase coherence length of the IPS electrons as 75–85 Å (Crampin, Kröger *et al.*, 2005; Wahl *et al.*, 2005). Quantum confinement

of IPS electrons to nanostructures was theoretically predicted on a system of 1-ML-high Na nanoislands on Cu(111) (Borisov *et al.*, 2007), and then experimentally demonstrated on Co islands on Au(111) (Schouteden and Van Haesendonck, 2009) and on Ag nanocrystals formed at Ag(111) surfaces (Schouteden and Van Haesendonck, 2012). In the experimental studies, STS with a closed feedback loop (Binnig *et al.*, 1985) was utilized to access higher IPSs, which appear at very high sample-bias voltages of 5–10 V.

In this section, we reviewed non-spin-polarized STM and STS measurements on electron confinement in various nanostructures. A detailed analysis of patterns of the spatial modulations provides information on the dispersion relation and the scattering properties of confined electrons. In the following sections, we present the results of spin-polarized STM and STS studies on confinement and scattering. It will be shown that majority and minority electrons are affected differently by confinement, and this leads to spatial modulations of the spin polarization of the sample.

IV. SPIN-POLARIZED SURFACE STATES ON MAGNETIC SUBSTRATES: THEORY AND EXPERIMENT

A. Experiments to extract the electron spin polarization

The spin-dependent analysis of electron confinement by SP-STM offers a way to extract spin polarization with subnanometer resolution on individual nanostructures (Oka *et al.*, 2010). Before we discuss these results, we briefly review other techniques for extracting the electron spin polarization.

The spin polarization of secondary electrons or photoelectrons emitted from surfaces can be extracted by a Mott detector (Gay and Dunning, 1992), by a low-energy electron diffraction (LEED) detector (Kirschner and Feder, 1979; Kirschner, 1985), or by a very-low-energy electron diffraction (VLEED) detector (Tillmann, Thiel, and Kisker, 1989).

The Mott detector and the LEED detector exploit spin-dependent scattering angles of incident electrons with respect to the scattering plane due to spin-orbit interaction. In a Mott detector, electrons are accelerated to an energy of 20–100 kV toward a Au target. Electrons with different spins are back-scattered into different directions. The number of electrons scattered in a specific direction is counted by two channeltrons mounted at $+60^\circ$ and -60° off the target normal. The difference of the electron counts N_1 and N_2 yields the asymmetry $A_N = (N_1 - N_2)/(N_1 + N_2)$. This asymmetry is related to the spin polarization of incident electrons P_e through the Sherman function S as $A_N = SP_e$. The magnitude of S is 0.1–0.4, which depends on the type of spin detector (Okuda and Kimura, 2013). For the LEED detector, electrons accelerated to 104.5 eV are diffracted by a W(001) single-crystal surface. The difference of the diffracted intensity for the (2,0) and $(\bar{2},0)$ beams is analyzed to extract the asymmetry.

The VLEED detector uses the spin-dependent reflectivity of incident electrons due to exchange-split band structures of the target. Electrons are accelerated to an energy of 2–10 eV, and they enter a target of Fe(001) (Tillmann, Thiel, and Kisker, 1989) or Fe(001)- $p(1 \times 1)$ -O surface (Bertacco and Ciccacci, 1999; Bertacco, Onofrio, and Ciccacci, 1999). Both surfaces

⁷Precisely, this is a Stark-shifted image-potential-derived state.

have a band gap in unoccupied states. The reflectivity of incident electrons is maximum at the center of the band gap in energy and decreases on approaching the edges of the band gap (Jaklevic and Davis, 1982). The energy position of the band gap is different for majority and minority spins and shifted due to the exchange split. Therefore, the reflectivity of incident electrons is largely spin dependent at the bottom and top of the band gap (Tillmann, Thiel, and Kisker, 1989). The number of reflected electrons is measured for the target magnetization in two opposite directions. A set of measurements gives the asymmetry of the reflected electrons, and this asymmetry is related to the spin polarization as discussed previously.

By combining a spin detector with scanning electron microscopy (SEM), which is known as spin-polarized SEM (spin SEM) (Koike and Hayakawa, 1984) or SEM with polarization analysis (SEMPA) (Unguris *et al.*, 1986), we can map the spatial distribution of the spin polarization of material surfaces, which reflects magnetic domain structures at the surface (Oepen and Kirschner, 1989; Unguris, Celotta, and Pierce, 1991; Konoto *et al.*, 2004; Oepen and Frömter, 2007). Recently, a spatial resolution of 3 nm was achieved (Koike, 2013). The combination of PES with a spin detector allows us to investigate spin-resolved electronic band structures, as demonstrated for Au(111) (Hoesch *et al.*, 2004), Cu(001) (Winkelmann *et al.*, 2008), Bi_{1-x}Sb_x (Hsieh *et al.*, 2009; Nishide *et al.*, 2010), and Co films on Cu(001) (Chiang *et al.*, 2012), and reviewed by Dil (2009) and Okuda and Kimura (2013).

The methods discussed so far give an integrated value of the spin polarization averaged over a large surface area, which is given by the electron beam size or the laser beam size. In Sec. IV.C, we show that SP-STM can measure the spatial variation of the spin polarization of the sample at the subnanometer scale and also reveal its energy dependence.

B. Spin-polarized electron scattering on magnetic substrates and films

The existence of a Shockley surface state in a gap of projected bulk bands along the Γ - L line is common to the (111) surfaces of the noble metals, Cu, Ag, and Au. Since the existence of such a bulk band gap is a common feature of face-centered-cubic (111) crystals, a Ni(111) surface is also expected to exhibit a Shockley surface state. In addition, surface states on a Ni(111) surface are anticipated to be spin polarized due to the ferromagnetism of Ni. Therefore, Ni(111) surfaces have been intensively investigated using PES (Himpsel and Eastman, 1978; Donath, Passek, and Dose, 1993; Kutzner *et al.*, 1997; Okuda *et al.*, 2009) and in theory (Braun and Donath, 2002; Magaud *et al.*, 2004; Ohwaki *et al.*, 2006). It was revealed that Ni(111) surfaces indeed have spin-polarized surface states. Spin-split Shockley surface states dispersing upward in energy were found (Donath, Passek, and Dose, 1993). The spin-split surface states have an exchange splitting of 50–100 meV and a band bottom for the majority-spin electron around the Fermi energy at $\bar{\Gamma}$ (Donath, Passek, and Dose, 1993; Okuda *et al.*, 2009). Thus, spin-dependent electron scattering phenomena might be investigated on Ni(111) surfaces.

Pons *et al.* (2003) performed STM and STS measurements on Ni(111) surfaces and observed spatial modulation in maps of the differential conductance on Ni(111). They ascribed this to the LDOS modulations due to the formation of standing waves of the spin-split Shockley surface states. Unfortunately, they did not resolve the spin splitting of the surface states. Braun and Rieder (2008) observed standing waves at two different locations on Ni(111) surfaces: (1) at a step edge, and (2) around impurities on a flat terrace. The analysis of their data revealed two branches in the dispersion relation. The two branches disperse upward in energy with the same curvature (effective mass $0.17m_e$), but start at different energies, -165 and -225 meV. Interestingly, data at a step edge lead to the lower branch of dispersion, and data around impurities on a terrace form the upper branch. Braun and Rieder (2008) interpreted the two branches in the dispersion relation as a spin-split Shockley surface state, the lower branch as a majority-spin band and the upper one as a minority-spin band. This splitting of 60 meV is in good agreement with values for the exchange splitting energy extracted from PES measurements (Donath, Passek, and Dose, 1993; Okuda *et al.*, 2009). They proposed that due to spin-dependent scattering at step edges, only one component of spin states was resolved at step edges. Nishimura *et al.* (2009) also performed STM and STS measurements on Ni(111) surfaces and obtained just one branch dispersing upward in the dispersion relation, which has an effective mass of $0.19m_e$ and a band bottom energy of -135 meV. They remarked that the electrostatic potential drops near step edges (Ono *et al.*, 2006), which leads to a downward shift of electronic structures in energy and might be a cause of the observed splitting of the Shockley surface-state band. SP-STM would give a clear-cut picture for the above discussion, but up to now there has been no report on spin-resolved electronic structures of the Ni(111) surface by SP-STM.

von Bergmann *et al.* (2004) performed SP-STM measurements on a system of oxygen atoms adsorbed on double-layer Fe films on W(110) and investigated spin-resolved electronic properties around single oxygen atoms. Differential conductance maps revealed that the LDOS around oxygen atoms is spatially modulated with highly anisotropic patterns. This anisotropy differs from observations on noble metal (111) surfaces, where a spatial modulation with circular patterns is observed (Crommie, Lutz, and Eigler, 1993b). SP-STM and STS revealed that electronic states involved in the LDOS modulation are highly spin polarized. A comparison of experimental data with *ab initio* spin-resolved band structure calculations demonstrated that minority-spin d states are responsible for the observed LDOS modulation and the anisotropic modulation patterns are ascribed to anisotropic band structures of the double-layer bcc Fe(110) surfaces on W(110) where the band structure in the $\bar{\Gamma}$ - \bar{H} direction differs from that in the $\bar{\Gamma}$ - \bar{N} direction.

These examples show that specific aspects of spin-split electron states in magnetic systems lead to novel phenomena which are absent for confinement and quantum interference in nonmagnetic systems. Spin-split electronic bands of majority- and minority-spin character need to be considered, and the anisotropy of the involved wave functions may induce spatially anisotropic modulation patterns in the differential

conductance. We show that mainly majority-spin electrons contribute to the spatially modulated LDOS due to spin-dependent electron confinement on Co islands on Cu(111), as discussed next.

C. Spin-polarized quantum confinement on a magnetic nanostructure

To study spin-dependent electron confinement, we focus on bilayer-high Co islands on Cu(111). Previous theoretical studies predicted that spin-polarized two-dimensional surface states exist on bilayer-high Co islands on Cu(111). They originate from *s-p* surface-state bands with majority-spin character (Diekhöner *et al.*, 2003; Niebergall, Stepanyuk *et al.*, 2006). In addition, there are *d*-related minority states, which lead to a peak in the differential conductance near -0.3 V (Diekhöner *et al.*, 2003). Figure 12(a) shows an STM image of a single Co island on Cu(111). It is two atomic layers high and its base length is 12 nm. Such an island contains 3900 atoms. As discussed in Sec. II.E.2, the identification of the magnetic configuration of the tip with respect to the island (see Fig. 4) is required to link the asymmetry of the differential conductance to the spin polarization of the island [Eqs. (20) and (21)].

Two maps of the differential conductance on the Co island were recorded, one in the AP magnetic configuration, and the other in the P configuration. To evaluate the spin polarization, the asymmetry of the differential conductance signal, defined as Eq. (20), was calculated. Figures 13(b)–13(e) show asymmetry ($A_{dI/dV}$) maps for different energies. The asymmetry $A_{dI/dV}$ maps all reveal that the asymmetry $A_{dI/dV}$ is highly position dependent within the Co island.⁸ A spatial modulation of the asymmetry $A_{dI/dV}$ can be clearly seen in the center region. The modulation pattern changes with energy and the sign of $A_{dI/dV}$ surprisingly also changes with energy.

The spatial modulations of the asymmetry $A_{dI/dV}$ can be interpreted by considering the spin dependence of electron confinement. The quantum confinement hardly influences energetically localized electronic states (*d* states) but mainly affects energetically dispersive states (*s-p* states) (Niebergall, Stepanyuk *et al.*, 2006). The majority *s-p* surface state is thus predominantly affected by electron confinement as compared to the minority *d* states (Niebergall, Stepanyuk *et al.*, 2006). Therefore, the spatial modulation of the asymmetry $A_{dI/dV}$ is ascribed to electron confinement of the majority *s-p* surface state. The wavelength of electrons of the majority *s-p* surface state becomes shorter with increasing energy, as described by the dispersion relation (Diekhöner *et al.*, 2003; Pietzsch *et al.*, 2006), leading to a change of spatial periodicity in the modulation pattern of the asymmetry $A_{dI/dV}$ maps. Note that the modulation length is not due to atomic corrugation, but much larger, ≥ 1.5 nm. This is a factor of 6 larger than the distance between nearest-neighbor Co atoms, 0.25 nm.

⁸Note that the difference in the sign of the asymmetry $A_{dI/dV}$ at the rim as compared to the center is ascribed to a so-called rim state. The rim state is spatially localized within 1 nm of the edges of the Co island, and it is identified in spectroscopy as a peak near the Fermi level (Pietzsch *et al.*, 2006).

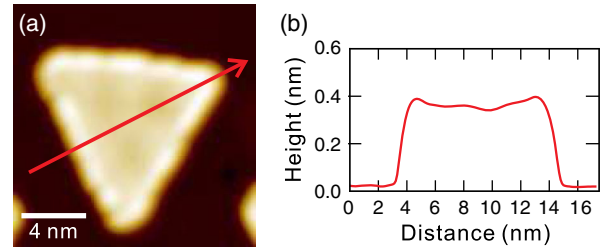


FIG. 12 (color online). Co islands on Cu(111). (a) Constant-current STM image of a triangular Co island on Cu(111). $V_S = -0.1$ V, $I = 1.0$ nA. (b) Line profile along the arrow in the STM image. The Co island is two atomic layers high, ≈ 0.4 nm, and has a base length of 12 nm. Adapted from Oka *et al.*, 2010.

The change of contrast of the asymmetry is interpreted by consideration of the energy dependence of the LDOS for majority-spin (n_\uparrow) and minority-spin (n_\downarrow) electrons. Figure 13(a) shows a plot of the calculated spin-resolved LDOS above a bilayer Co film on Cu(111) as a function of energy. The plot reveals that the dominant spin character is highly energy dependent. The spin polarization on the island, which is defined as

$$P_{\text{Co}}(eV) = \frac{n_\uparrow(eV) - n_\downarrow(eV)}{n_\uparrow(eV) + n_\downarrow(eV)}, \quad (28)$$

is positive in an energy range where the DOS of the majority-spin electron is dominant [Fig. 13(c)], and it is negative where that of the minority-spin electron is dominant [Figs. 13(b) and 13(e)]. Where the DOSs of majority- and minority-spin electrons are comparable, the spin polarization changes around zero [Fig. 13(d)]. This interpretation is fully supported by *ab initio* calculations of spin-polarization maps on the Co island [Figs. 13(f)–13(i)]. The overall agreement in the modulation pattern of the central region of the island at different energies identifies the dominant role of the energy-dependent spin-resolved DOS for change of contrast. The spatial variation of the spin polarization influences also the tunnel magnetoresistance, where it leads to a pronounced spatial oscillation (Oka *et al.*, 2011). This is reviewed in Sec. VI.

A detailed analysis of the spatial and energy dependence of the asymmetry $A_{dI/dV}$ reveals good agreement between the experimental data and the calculated spin polarization. Figure 14 shows two line profiles taken on the asymmetry $A_{dI/dV}$ map and on the spin-polarization map along the yellow arrows in Figs. 13(c) and 13(g). The spin polarization of the tip can be considered as constant, and the asymmetry $A_{dI/dV}$ is proportional to the spin polarization on the sample, i.e., $A_{dI/dV} = -(\text{const} \times P_T)P_S$. The line profiles show very similar structures, implying that the spin polarization of the tip should be negative due to the minus sign in front of the term of $(\text{const} \times P_T)P_S$. The line profiles reveal a difference in scale by a factor of 10, which is ascribed to the constant spin polarization of the tip. We estimate that the spin polarization of this tip is -10% around the Fermi energy. The overall agreement between the two line profiles demonstrates that the

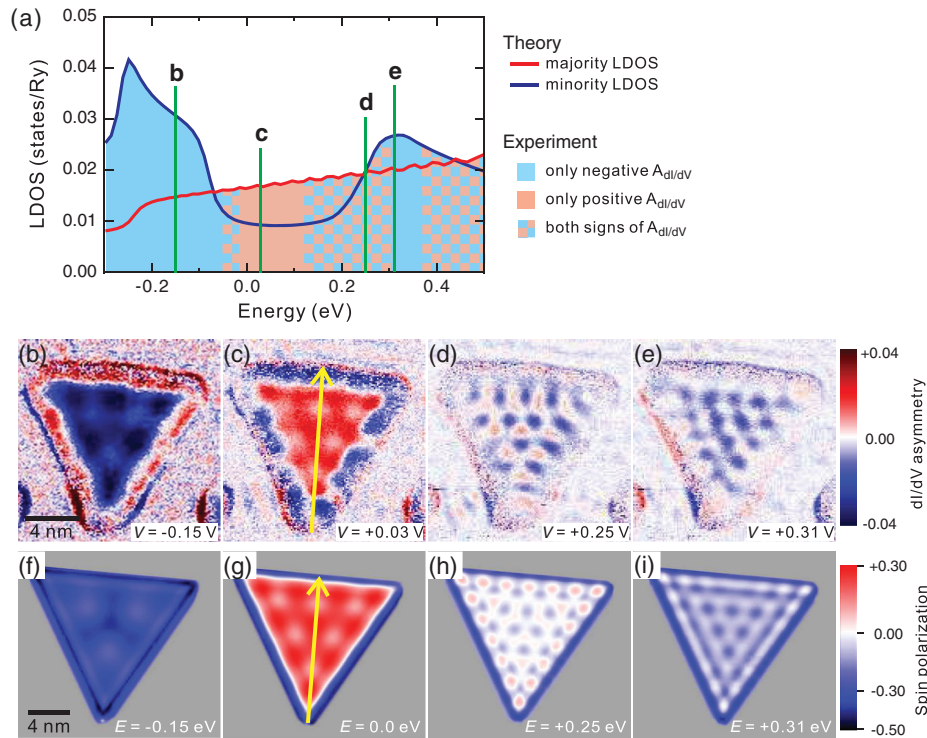


FIG. 13 (color). Energy dependences of the measured differential conductance dI/dV -asymmetry maps and calculated spin-polarization maps of Co islands. (a) Calculated spin-resolved LDOS of a two atomic-layer Co film on Cu(111). (b)–(e) Experimental dI/dV -asymmetry maps measured on the Co island of Fig. 12(a). The dI/dV -asymmetry maps are calculated from two dI/dV images measured at AP and P states from Eq. (20). Measurement conditions of dI/dV images: $B = -1.1$ T, $V_{\text{stab}} = +0.5$ V, and $I = 1.0$ nA. (f)–(i) Calculated spin-polarization maps of the triangular Co island. The spatial dependence of the spin polarization as defined by Eq. (28) is shown by the maps, which are calculated from two LDOS maps for the majority and the minority states. Vertical green lines in (a) correspond to the energy positions where the dI/dV asymmetry maps are obtained. A color map in (a) indicates the energy area where the experimental results for the inner part of the Co island show only positive (blue), only negative (red), or both signs (lattice pattern with blue and red) of the dI/dV asymmetry in the dI/dV -asymmetry maps. Yellow arrows in (c) and (g) give line profiles in Fig. 14. From Oka *et al.*, 2010.

asymmetry $A_{dI/dV}$ map obtained by SP-STM reflects the spin polarization on the sample.

The correlation between the experimentally measured asymmetry $A_{dI/dV}$ and the spin polarization on the sample was further explored regarding the energy dependence (Fig. 15). A spin polarization above a bilayer Co film is

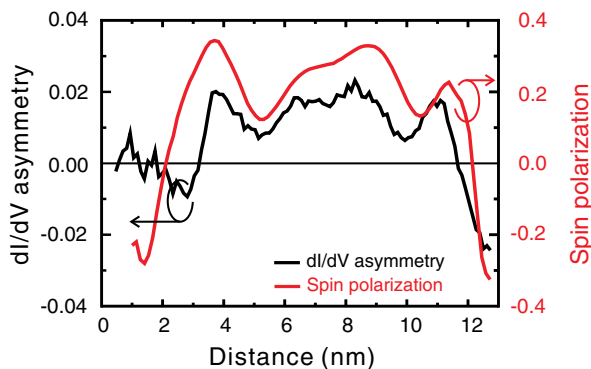


FIG. 14 (color online). Line profiles along the yellow arrows in Figs. 13(c) and 13(g). The plots correspond to the profiles of the dI/dV -asymmetry map and the spin-polarization map, respectively.

plotted as a function of energy and compared with a measured $A_{dI/dV}$, which is extracted from an average of the $A_{dI/dV}$ over the center region of a Co island. The two plots in Fig. 15 show similar characteristics but differences in the magnitude. The differences are ascribed to effects of the spin polarization of the tip and its energy dependence. This suggests that we can infer the spin polarization of the tip from the data of Fig. 15. We applied this approach to bulk Cr tips, extracting a tip spin polarization as large as 45% at the Fermi energy (Corbetta *et al.*, 2012). The similarities between the experimentally measured $A_{dI/dV}$ and the spin polarization on the sample demonstrated for the position (Fig. 14) and the energy dependences (Fig. 15) lead us to conclude that the asymmetry obtained by SP-STM reflects the spin polarization on the sample, and the $A_{dI/dV}$ map can provide a spatial distribution of the sample spin polarization at the subnanometer scale.

The spin-polarized quantum confinement is related to the existence of a spin-polarized s - p surface state which forms a two-dimensional electron system at the surface. The spin-polarized s - p surface state is not unique to the Co islands on Cu(111), but seems to be universal for magnetic nanostructures on noble metal (111) surfaces. Theory predicted that majority s - p surface states exist on Co islands on Au(111) (Rastei, Bucher *et al.*, 2007) and, indeed, it was confirmed by

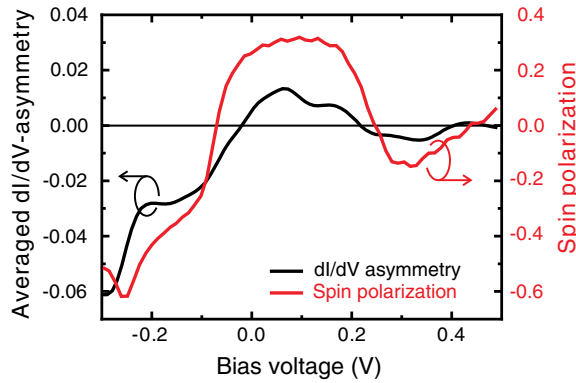


FIG. 15 (color online). Energy dependences of the measured differential conductance asymmetry and the calculated spin polarization. Plots of the dI/dV asymmetry averaged over the inner part of the Co island and of the spin polarization of a two atomic-layer Co film on Cu(111).

SP-STM and STS measurements (Schouteden *et al.*, 2011). For monolayer Fe islands on Au(111), majority s - p surface states were also found in *ab initio* calculations (Delga *et al.*, 2011; Donati *et al.*, 2011; Marathe *et al.*, 2012) and the electron confinement of the surface states was observed in differential conductance maps using STM and STS (Delga *et al.*, 2011; Marathe *et al.*, 2012). Bilayer Ni islands on Cu(111) are also expected to show spin-polarized s - p surface states from theory (Magaud *et al.*, 2004) and STM and STS measurements (Pons, Mallet, and Veuillen, 2001). However, spin-polarized measurements by SP-STM have not yet been done.

D. Tuning spin polarization on the nanoscale by confinement

As already seen, the surface state can be inherently spin polarized on magnetic substrates or, as discussed in the coming sections, can become polarized upon scattering at magnetic impurities or structures. In both cases, confinement of electrons of majority and minority character is expected to differ. The resulting confinement interference pattern can be characterized by the space-resolved electron density of states $n_{\uparrow(\downarrow)}(E, r)$ of majority (\uparrow) and minority (\downarrow) electrons. The two densities together define the local spin polarization

$$P = \frac{n_{\uparrow} - n_{\downarrow}}{n_{\uparrow} + n_{\downarrow}}, \quad (29)$$

which enters the determination of all tunneling-related processes and quantities, such as the differential conductance and the TMR. Thus tailoring the local spin polarization offers novel venues toward turning these properties. Since the spin polarization is strongly affected by electron confinement (Niebergall, Stepanyuk *et al.*, 2006; Oka *et al.*, 2010), changing the latter allows us to manipulate the polarization. From the properties of the electron confinement described above, two basic possibilities of confinement tailoring can be derived: (i) changing the confinement geometry and scattering properties of the confining boundary or (ii) changing the band structure of the electrons to be confined.

The former possibility is straightforward. We have seen that different confinement geometries, for example, different quantum corrals or islands of different sizes, produce different confinement patterns. In the case of spin-polarized confinement the resulting spatial change in majority and minority electron confinement patterns would inevitably lead to a change in the local spin-polarization distribution.

The latter possibility is to select a surface with a predefined electronic structure. One can choose the material of the substrate, since the energy and effective mass of the surface-state band are different at different surfaces (Reinert *et al.*, 2001). But changing the chemical composition of the surface is not, strictly speaking, necessary. It has been shown, both experimentally and theoretically, that the surface state is sensitive to the lattice parameter of the surface and responds to the change thereof (Rastei, Bucher *et al.*, 2007). For example, Rastei, Heinrich *et al.* (2007) showed that Co nanoislands on a Cu(111) surface exhibit mesoscopic relaxations and thus the average bond length within the island depends strongly on the island size. Position-dependent measurements of differential conductance on islands of different sizes allowed one to correlate the energy position of the Co surface state with the bond length within the Co islands. Thus, by changing the local bond length by exploiting the strain or stress, one can tailor electron confinement and consequently the resulting spin polarization.

Both these possibilities to tailor confinement are, however, inherently static and feasible only at the design stage of the experiment. To be able to tailor confinement dynamically other methods are needed. One such method is the application of an external electric field. It was shown (Ignatiev and Stepanyuk, 2011; Berland, Einstein, and Hyldgaard, 2012; Brovko *et al.*, 2014) that the surface-state band exhibits a Stark-like shift if the surface is exposed to an electric field. This opens the possibility of dynamical manipulation of the band structure of the surface states and accordingly the spin polarization. As an example, Fig. 16 shows the effect of an external electric field on the surface state of a Co nanoisland on Cu(111) (Ignatiev, Brovko, and Stepanyuk, 2012). One can see that an electric field of 0.6 V/\AA shifts both majority and minority surface-state bands by about 0.15 eV. The accompanying change of the Fermi wave vector is depicted in Fig. 16 by arrows.

The change of the Fermi wave vector of the surface state is reflected in the change of the electron confinement pattern. An example is given in Fig. 17. Here the electron density for majority and minority electrons is plotted for zero field and a field of 0.6 V/\AA along with the TMR map, which is linked to the spin polarization by

$$\text{TMR}(E) = \frac{2P_T(E)P_S(E)}{1 - P_T(E)P_S(E)}, \quad (30)$$

where P are the polarizations of the surface and the imaginary STM tip (here taken to be 0.2).⁹ The electric field obviously affects the TMR and spin-polarization distribution across the island.

⁹See Eq. (32) for the discussion of this equation.

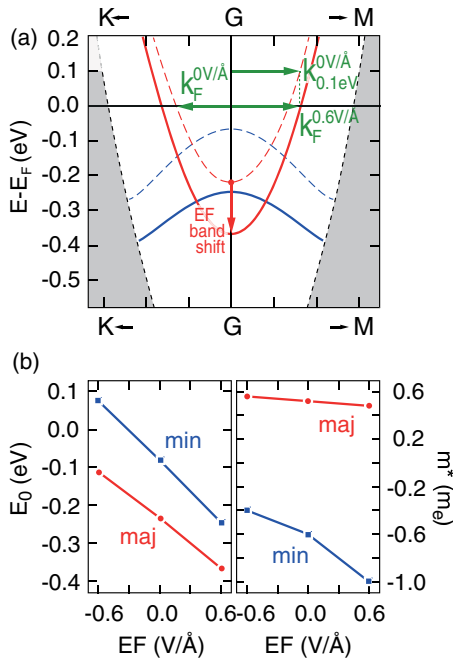


FIG. 16 (color online). (a) Sketch of the band structure and the shifts induced by an electric field (EF). The dashed lines show the zero-external-field case. The solid lines show data for a field of 0.6 V/\AA . Majority and minority bands are plotted with solid and dotted curves, respectively. The shaded area shows a continuum of bulk states. (b) The binding energies (E_0) and curvatures as given by the effective masses (m^*) of majority (circles) and minority (squares) surface bands are plotted. Adapted from Ignatiev, Brovko, and Stepanyuk, 2012.

Alloying offers a further way to modify the electronic structure at surfaces. Binary metal alloys of noble metals modify Shockley surface states (Asonen and Pessa, 1981; Asonen *et al.*, 1982). ARPES measurements revealed that the (111) surface of a $\text{Cu}_{0.9}\text{Al}_{0.1}$ single-crystal alloy shows Shockley surface states (Asonen and Pessa, 1981; Asonen *et al.*, 1982). The band bottom of the surface states is shifted downward in energy by 0.4 eV for a (1×1) surface atomic structure and by 0.8 eV for a $(\sqrt{3} \times \sqrt{3})R30^\circ$ structure compared to pristine $\text{Cu}(111)$ (Asonen and Pessa, 1981; Asonen *et al.*, 1982). Yu, Sagisaka, and Fujita (2009) observed spatial oscillations in differential conductance maps on a $\text{Cu}_{0.91}\text{Al}_{0.09}(111)$ single-crystal alloy by STM and STS due to the formation of standing waves of the shifted Shockley surface states. Recently, Yu *et al.* (2013) performed STM and STS measurements on Co islands on a $\text{Cu}_{0.91}\text{Al}_{0.09}(111)$ single-crystal alloy. They found a sharp peak at -0.45 V in differential conductance spectra measured at the center of Co islands, and ascribed the peak to a minority Co d surface state. They also found that the surface state shifts downward in energy while approaching the island edge. These findings are very similar to those of a minority d surface state of Co islands on $\text{Cu}(111)$ (Diekhöner *et al.*, 2003; Rastei, Heinrich *et al.*, 2007), although the energy position of the state is slightly lower than -0.35 V for Co islands on $\text{Cu}(111)$ (Pietzsch *et al.*, 2006). Metal overlayers (Hasegawa, Suzuki, and Sakurai, 2002; Bendounan *et al.*, 2003; Cercellier *et al.*, 2004) and noble gas adsorptions (Park *et al.*, 2000; Hövel, Grimm, and

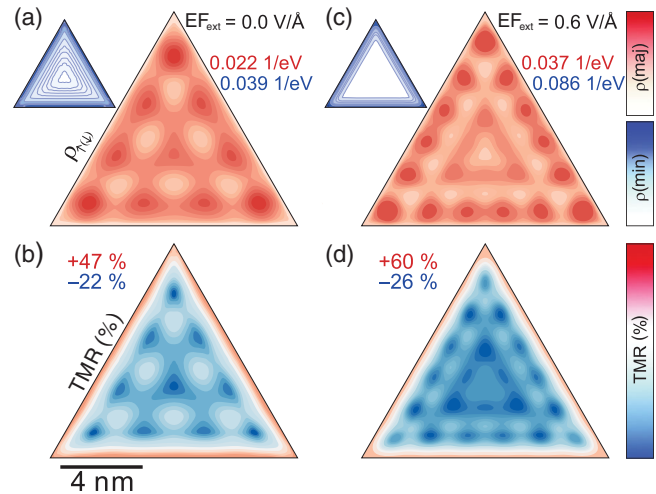


FIG. 17 (color). Electron density of states of a bilayer Co island at the Fermi energy E_F in (a) zero external electric field and (c) in an external field of 0.6 V/\AA calculated for majority and minority (insets) electrons. The color map is given on the right of the figure. The numbers next to the electron density of states distributions denote maximum values of the majority (red) and minority (blue) electron densities. The minimal values are always zero $1/\text{eV}$ (white). (b), (d) The TMR distribution maps for the above cases, calculated with Eq. (30). The numbers next to the maps denote the boundaries of the color scale. White always corresponds to zero TMR. The Co island has a base length of $\sim 12 \text{ nm}$, which is the same size as was considered in Fig. 13 (Oka *et al.*, 2010). Adapted from Ignatiev, Brovko, and Stepanyuk, 2012.

Reihl, 2001; Forster *et al.*, 2003) are further means to modify surface states of the noble metal (111) surfaces. These can also be exploited for the tuning of the spin-polarized Shockley surface-state energy position.

V. SPIN POLARIZATION OF SURFACE-STATE ELECTRONS UPON SCATTERING AT MAGNETIC SCATTERERS: THEORY AND EXPERIMENT

A. Spin polarization induced by adatoms

The presence of impurity atoms on metal surfaces influences the electronic and magnetic properties of surfaces. One interesting phenomenon due to magnetic adatoms on metal surfaces is the Kondo effect (Kondo, 1964). STM and STS measurements revealed that the Kondo resonance appears on single magnetic impurity atoms around the Fermi energy, and it extends a few nanometers away from the center of impurity atoms (Li, Schneider, Berndt, and Delley, 1998; Madhavan *et al.*, 1998). Another phenomenon due to adatoms on metal surfaces is an adatom-induced localization of two-dimensional surface states. It was predicted that any attractive potential on two-dimensional states gives rise to a bound state (Simon, 1976). STM and STS demonstrated that a bound state exists on single adatoms on $\text{Ag}(111)$ and $\text{Cu}(111)$ right below the band bottom of two-dimensional surface states (Olsson *et al.*, 2004; Limot *et al.*, 2005). Lazarovits, Szunyogh, and Weinberger (2006) theoretically showed that such a bound state is ascribed to a resonance in s -like states, and it can be

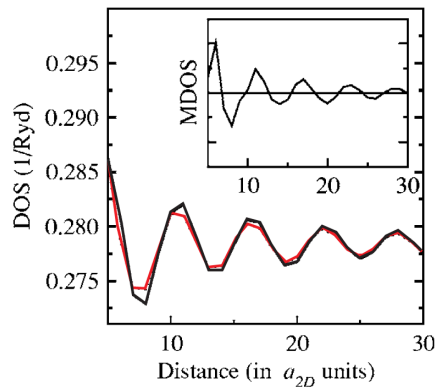


FIG. 18 (color online). Calculated minority-spin (black line) and majority-spin (gray line) s -like DOSs at $E - E_F = 0.012 \text{ Ry} \approx 0.16 \text{ eV}$ as a function of the distance from a single Fe impurity on a Cu(111) surface. The DOS was calculated at the first vacuum layer. The distance is expressed in units of the nearest-neighbor distance in Cu(111), $a_{2D} = 2.55 \text{ \AA}$. Inset: s -like magnetization density of states (MDOS), which is defined as the difference of the spin-projected s -like DOSs. Adapted from Lazarovits *et al.*, 2006.

spin polarized for magnetic adatoms. They also found that two-dimensional surface states interact with minority-spin d states of magnetic adatoms and experience spin-dependent resonant scattering. Figure 18 highlights this finding. The curves show the calculated spin-projected s -like DOSs as a function of the distance from a single Fe adatom on Cu(111). The s -like DOS clearly shows a spatial modulation in both spin channels due to the quantum interference of two-dimensional surface-state electrons. But a distinct difference in the amplitude of the modulation is calculated, which is revealed in the inset of Fig. 18 as the magnetization density of states. The spin-dependent resonant scattering enhances the amplitude of the s -like DOS modulation in the minority-spin channel. Consequently, a single Fe impurity on Cu(111) induces long-range oscillations in the relative amplitude of majority- and minority-spin s -like DOSs (inset of Fig. 18), leading to a long-range RKKY (Ruderman and Kittel, 1954; Kasuya, 1956; Yosida, 1957) interaction on noble metal (111) surfaces, which was predicted by Stepanyuk *et al.* (2004).

B. Quantum mirages and magnetic interactions in quantum corrals

Particularly instructive and by now famous consequences of electron confinement are quantum mirages. Atoms arranged by atomic manipulation (or naturally) on surface-state-supporting surfaces may form special closed geometries, which exhibit electron focusing as shown in Fig. 19 (Manoharan, Lutz, and Eigler, 2000). In their pioneering work, Manoharan, Lutz, and Eigler (2000) exploited atomic manipulation to assemble an elliptical quantum corral on a Cu(111) surface. The quantum corral serves as a focusing device for surface-state electrons. They showed the possibility of projecting the electronic structure surrounding a magnetic Co adatom to a remote location. Local variations of the DOS near the adatom, which was positioned in one of the focal points of the quantum ellipse, were coherently focused to the empty focal point,

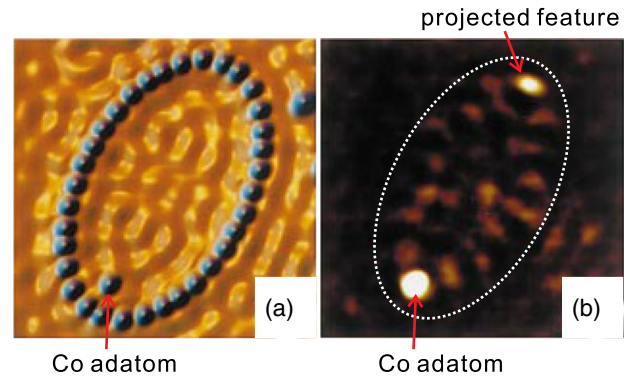


FIG. 19 (color online). Quantum mirage in a corral. (a) STM image of an elliptical quantum corral with a Co atom at the left focus. $V = 8 \text{ mV}$, $I = 1 \text{ nA}$, $15.4 \times 15.4 \text{ nm}^2$, and $T = 4 \text{ K}$. (b) Differential conductance d/dV difference map. This map was obtained via the difference between differential conductance maps of the quantum corral with and without the Co adatom. The difference map shows a projected electronic signature at the empty upper-right focus, originating from the Co adatom at the lower-left focus. This projected feature is termed a “mirage” in a corral. The ellipse with a dashed white line indicates the boundary of the corral. Adapted from Manoharan, Lutz, and Eigler, 2000.

forming a spectral image or “quantum mirage.” The corral acted as a quantum mechanical resonator, while the two-dimensional Cu surface-state electrons were the projection medium. As a result, a Kondo resonance (Kondo, 1964; Li, Schneider, Berndt, and Delley, 1998; Madhavan *et al.*, 1998) signature in differential conductance spectroscopy could be detected in the empty focus. The same conclusion could be derived from state-of-the-art *ab initio* calculations as shown in Fig. 20 (Stepanyuk *et al.*, 2005), which have shown that local variations of the LDOS can indeed be focused by surface structures, allowing not only projection of the magnetization of an adsorbate onto a remote location, but also tailoring of the interaction between adsorbates, as discussed in Sec. V.C.

Following those pioneering works numerous experiments and theoretical predictions have been made: the same idea of surface-state confinement has been applied to corrals on topological insulators (Fu, Zhang, Wang, and Li, 2011), the study of coupled quantum corrals was undertaken (Mitsuoka and Tamura, 2011), and special cases of surface states scattering on surfaces with pronounced spin-orbit contribution were investigated (Walls and Heller, 2007).

C. Surface-state-mediated interactions and exchange coupling between adatoms

The wide variety of effects connected to spin-polarized and non-spin-polarized LDOS oscillations at surfaces greatly expands if several well-defined scatterers are placed close to each other. As can be expected, taking into account the opticslike properties of surface-state electrons, LDOS oscillations will overlap, forming interference patterns which are the origin of a multitude of surface-based phenomena. A typical picture of such an interference pattern is presented in Fig. 21(a), where a constant-current STM image of two Co

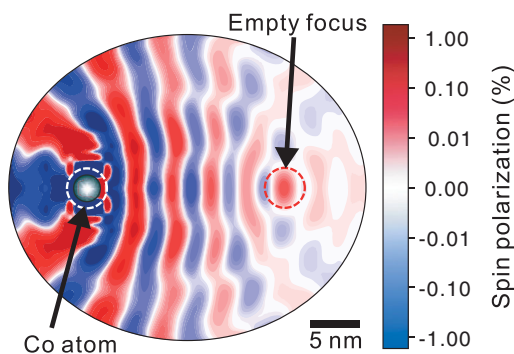
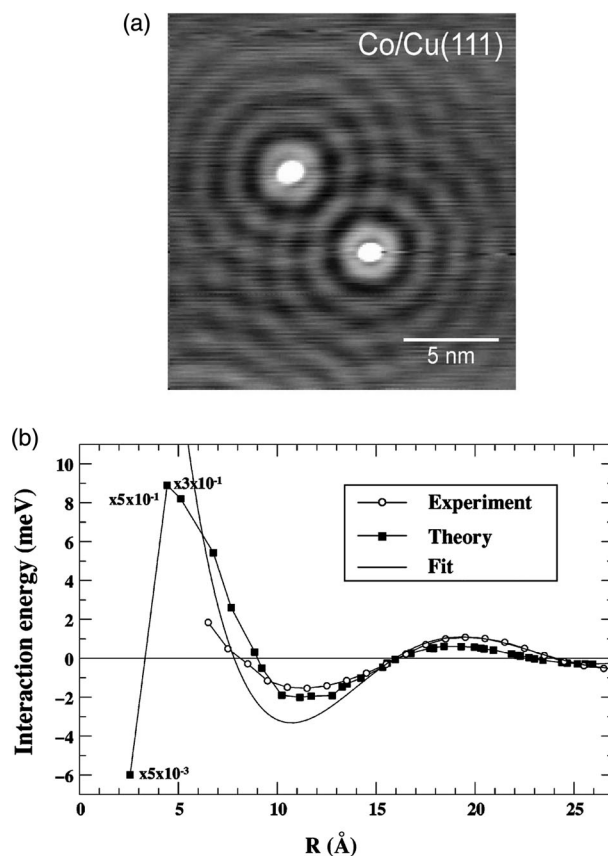


FIG. 20 (color). Spin-polarization map of surface-state electrons inside an elliptic Co corral on a Cu(111) surface. One focus of the corral is occupied by a Co adatom (white dashed circle). The mirage in the empty focus is highlighted by the red dashed circle. The geometrical parameters of the corral are the same as in the experimental setup of Fig. 19 (Manoharan, Lutz, and Eigler, 2000), i.e., semiaxis $a = 71.3 \text{ \AA}$ and eccentricity $e = 0.5$. Adapted from Stepanyuk *et al.*, 2005.

adatoms on Cu(111) is shown (Stepanyuk *et al.*, 2003). The energy of the interaction between the adatoms becomes dependent on the separation between the adatoms. This dependence carries a long-range character, and is, as already noted, the basis of the RKKY interaction. In Fig. 21(b) the interaction of two Co adatoms on a Cu(111) surface measured experimentally and calculated from first principles is fitted by a simple RKKY model, as given by Hyldgaard and Persson (2000). The nearly perfect match underlines the importance of the RKKY-like interaction for various aspects of surface physics, which still attract the interest of the community (Wahlström *et al.*, 1998; Hyldgaard and Persson, 2000; Stepanyuk *et al.*, 2003; Zhou *et al.*, 2010). If either the surface or the nanostructures thereon are magnetic, the scattering of electrons at impurities will be spin dependent. This leads to the formation of spin-polarized LDOS interference and, with it, to RKKY-mediated magnetic interaction. The RKKY interaction can be found to be responsible for such fascinating effects as the formation of superlattices (Silly *et al.*, 2004) and long-range exchange magnetic correlation (Stepanyuk *et al.*, 2003; Meier *et al.*, 2008; Smirnov *et al.*, 2009; Zhou *et al.*, 2010; Khajetoorians *et al.*, 2012).

Recent advances in experimental scanning probe techniques have made it possible to probe such RKKY-mediated exchange interactions in individual atom pairs, atomic chains, and more complex nanostructures by STM-based single-atom magnetometry (Meier *et al.*, 2008). In state-of-the-art experiments Khajetoorians *et al.* (2012) were able to map out the distance dependence of the RKKY exchange interaction of Fe adatoms on a Cu(111) surface. The results are in very good agreement with theoretical calculations and can be well fitted with the theoretical RKKY curve. The work of Khajetoorians *et al.* demonstrates real-space access to the magnetic states of nanostructures and provides an experimental approach to tackling open fundamental questions in magnetism.

It was shown that electron density redistribution (formation of standing waves) in quantum corrals governs adatom adsorption and nanostructure growth, allowing for creation of ordered arrays of adsorbates, virtual “orbits,” or empty



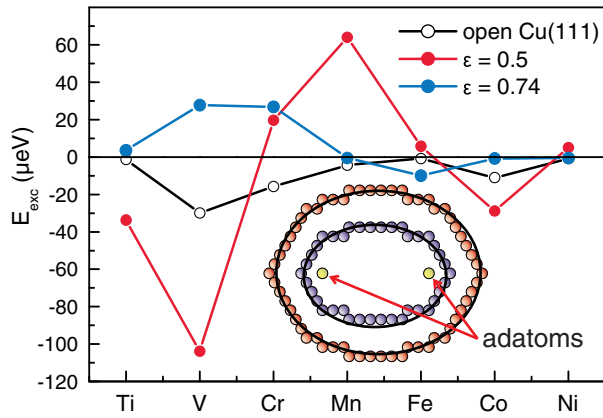


FIG. 22 (color online). The exchange interaction between magnetic adatoms inside Cu corrals of different eccentricities. The distance between foci is fixed. The exchange interaction on an open Cu(111) surface is presented by the black line. The exchange interaction in Cu corrals with eccentricities $\epsilon = 0.5$ and 0.74 is shown by the gray lines. The inset shows the corresponding models used for the calculations. Negative energies mean that the spins of both adatoms are ferromagnetically coupled, while positive energies correspond to an antiferromagnetic coupling. Adapted from Stepanyuk *et al.*, 2005.

nanostripe magnetization, and the asymmetry of the differential conductance was calculated from the data. As discussed previously, the asymmetry of the differential conductance is a measure of the spin polarization of the sample. The Co nanostripe shows a negative value of the asymmetry, while the Pt(111) in proximity to the Co nanostripe shows a positive value. The observed positive value of the asymmetry decays exponentially with a decay length of 0.9–1.2 nm as a function of distance from the stripe and vanishes within a few nanometers. The spin polarization at 4.1 Å above Pt(111) in proximity to an embedded Co chain was calculated by self-consistent *ab initio* calculations. The Pt atom closest to the Co chain shows an induced spin polarization of about +9% at +0.3 eV. The calculated spin polarization shows an exponential decay as a function of distance from the Co chain. It appears that induced spin polarization in a nonmagnetic substrate depends greatly on the polarizability of the substrate, which is larger for heavy elements.

Indeed we find in the lighter element Cu a smaller spin polarization in proximity to a bilayer Co island edge, as compared to the results previously discussed for a Pt substrate. At a distance of only 0.5 nm away from the Co edge (position 4.7 nm in Fig. 26) we measure a magnitude of the asymmetry of 0.007 at most. In view of the spin polarization of the tip of the order of 0.3 used here (Corbetta *et al.*, 2012) we estimate an upper limit for the magnitude of spin polarization in Cu induced by Co of 1%–2%. The asymmetry approaches zero, and consequently the induced spin polarization is below the detection limit, at larger distances. These examples show that SP-STM is capable of detecting even minute magnitudes of spin polarization in the low percent range with high spatial resolution. To appreciate these findings it is important to realize that spin-polarized electrons spill out from the Co structure toward the substrate surface. Thus, a spin-dependent redistribution of the electron density of states at the Co island

edge occurs. The underlying spin-dependent Smoluchowski effect (Polyakov *et al.*, 2012) is reviewed in the following.

More than 70 years ago, Smoluchowski proposed that the electron charge density does not follow atomically sharp surface geometries, but a redistribution and smoothing of the electron density at surface protrusions occurs to minimize the electron kinetic energy (Smoluchowski, 1941). This Smoluchowski effect has a significant impact on various properties of surfaces, for example, the local variation of the work function (Besocke and Wagner, 1973; Besocke, Krahl-Urban, and Wagner, 1977; Krahl-Urban, Niekisch, and Wagner, 1977; Wandelt, 1991; Ishida and Liebsch, 1992; Jia *et al.*, 1998; Merrick, Inglesfield, and Attard, 2005), the DOS (Crommie, Lutz, and Eigler, 1993b; Avouris and Lyo, 1994; Avouris, Lyo, and Molinàs-Mata, 1995), and on the occurrence of forces due to resulting dipole fields (Park *et al.*, 2005). These impacts of the Smoluchowski effect have been discussed so far in light of the redistribution of the electron charge density. Polyakov *et al.* (2012) expanded the description to include spin-dependent effects, where majority- and minority-spin electrons contribute differently to the charge redistribution.

They performed *ab initio* calculations by means of the Vienna simulation package (VASP) (Kresse and Furthmüller, 1996) using the Perdew-Wang version of the generalized gradient approximation with the Perdew-Wang 1991 functional (GGA-PW91) (Perdew and Wang, 1992). The edge of a bilayer-high Co island on Cu(111) is mimicked by an infinite stripe of Co atoms, which consists of four atomic rows wide in the topmost layer and five for the lower layer, and sits on the Cu substrate described by a slab of five layers [Fig. 23(a)]. The atomic structures of the infinite Co stripe are fully relaxed. Figure 23(b) presents energy- and site-resolved plots of the calculated total LDOSs for the minority and majority electrons in the vacuum space above the edge of the Co stripe. The total LDOS is strongly reduced above the step edge (position 3) and increased above the Cu surface (position 5), indicating charge redistribution at the step edge. This manifests the Smoluchowski effect at the Co step edge. The plots of the spin-resolved LDOSs for the minority and majority spins reveal reduction and increase of the LDOS above the edge (position 3) and the Cu surface (position 5), respectively, in both spin states. However, the LDOS for the minority electron is significantly larger than that for the majority electron. The *ab initio* calculations clearly demonstrate the spin dependence of the charge redistribution across a step edge of a magnetic nanostructure. A spin-polarization map near the Co step edge as functions of energy and site (Fig. 24) is calculated from the two plots of the spin-resolved LDOS [Fig. 23(b)] using Eq. (28).

SP-STM and STS allow one to discuss the spin polarization on the sample qualitatively by extracting $A_{dI/dV}$ as demonstrated in Sec. IV.C. The calculated spin-polarization map was compared with the experimentally extracted $A_{dI/dV}$. This has been investigated on a straight edge of a Co island, which faces a large open Cu(111) surface (Fig. 25). The area of interest of this study is shown in a line profile of the Co island as the shaded area (inset of Fig. 25). The asymmetry $A_{dI/dV}$ is extracted as described in Sec. IV.C. Three line profiles of the asymmetry are shown in Fig. 26 for different bias voltages.

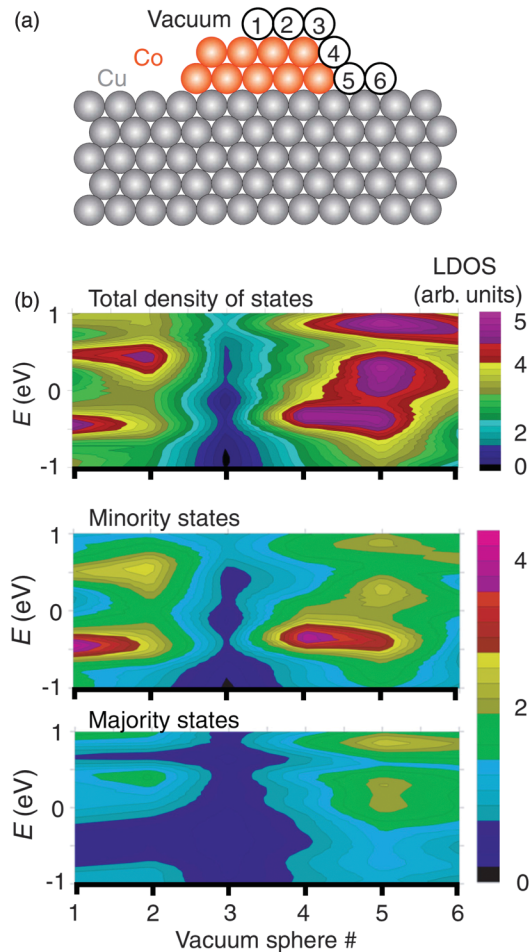


FIG. 23 (color). (a) Hard sphere model of the system used in the calculations of the spin-dependent Smoluchowski effect. Note that all atomic positions were allowed to relax. (b) Plots of the energy dependence of the total density of states (top) and of the spin-resolved density of states of minority (center) and majority (bottom) electrons as calculated at the position of the vacuum spheres identified in (a). From Polyakov *et al.*, 2012.

A spatial variation of the $A_{dI/dV}$ is visible and most pronounced near the position of 3–3.5 nm, i.e., at the descending slope of the step. The magnitude and sign of the spatial variation strongly depends on the bias voltage. To compare the theoretical (Fig. 24) with the experimental data (Fig. 26), an alignment of the horizontal spatial axis is required. The position of half step height is chosen as the common point. The position 4 nm of the experimental line profiles corresponds to the lateral position of the vacuum sphere 4. The $A_{dI/dV}$ for -0.05 V [Fig. 26(b)] shows small positive values near the upper step edge and small negative values at the half height of the step edge, and changes to zero above the Cu surface. This agrees favorably with the behavior of the calculated spin polarization across the step edge at -0.05 eV in Fig. 24. For other energies also, good agreement is found in comparison between the experiment and theory.

In conclusion, this combined experimental and theoretical work reveals that electron redistribution near surface protrusions is a spin-dependent phenomenon, described by the spin-dependent Smoluchowski effect.

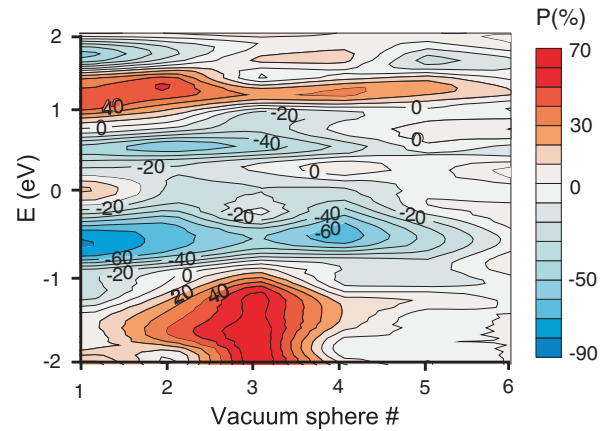


FIG. 24 (color). Calculation of the energy dependence of the spin polarization P at the vacuum spheres across the step edge. The spin polarization P is defined as Eq. (28). The position of the vacuum spheres is presented in Fig. 23(a). Adapted from Polyakov *et al.*, 2012.

E. Induced spin polarization in systems with strong spin-orbit coupling

Systems with strong spin-orbit coupling provide interesting electronic properties at surfaces. Spin-orbit coupling lifts the spin degeneracy of surface states, leading to the formation of spin-polarized surface states. Figure 27 schematically explains some key features of surface states of systems of strong spin-orbit coupling.

For systems with (almost) no spin-orbit coupling, surface states are degenerate and can be described by a single parabola in the dispersion relation as already discussed above in Sec. III. When spin-orbit coupling exists, the spin degeneracy

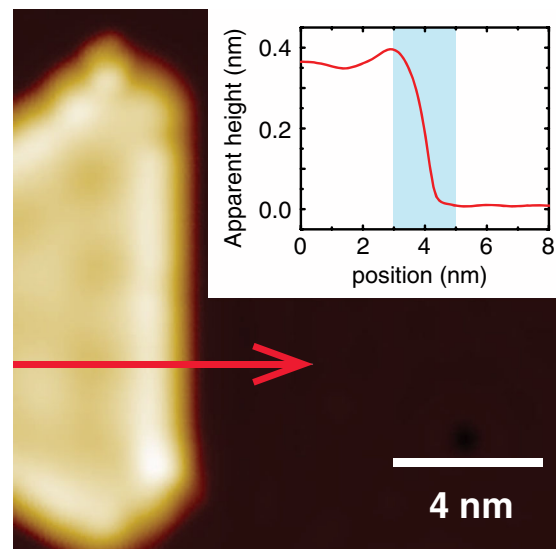


FIG. 25 (color online). Constant-current image ($V_{\text{gap}} = +0.1$ V, $I_t = 1$ nA, $T = 10$ K, bulk Cr tip) at the edge of a two-atomic-layer-high Co nanoisland on Cu(111). Inset: line profile along the line indicated in the figure. The highlighted area indicates the extension of the Co island step edge region of the dI/dV asymmetry line profiles in Fig. 26. From Polyakov *et al.*, 2012.

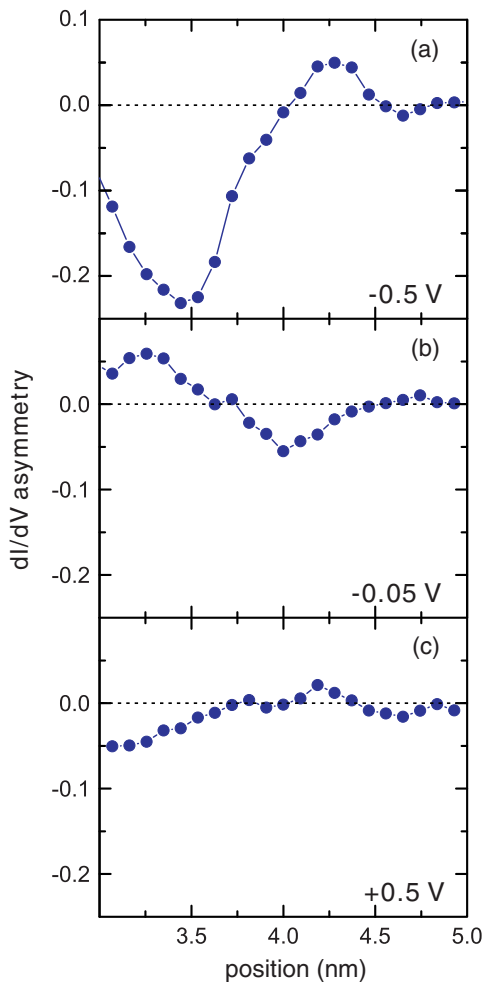


FIG. 26 (color online). $A_{dI/dV}$ line profiles for different gap voltages applied to the sample of the tunnel junction with reference to the tip. Gap voltage (a) -0.5 V, (b) -0.05 V, and (c) $+0.5$ V. The line profile is averaged over six adjacent lines next to the arrow in Fig. 25. From Polyakov *et al.*, 2012.

of surface states is lifted due to the lack of space inversion symmetry at the surface, resulting in two spin-split states [Fig. 27(a)]. This is the so-called Rashba effect (Bychkov and Rashba, 1984). The gradient of the potential at the surface acts as an electric field normal to the surface. Because of spin-orbit coupling, the spin direction of spin-split surface-state electrons lies in the surface plane and perpendicular to their momenta. This leads to helical spin texture at the constant-energy contour of the state [Fig. 27(b)].

Three-dimensional topological insulators also show rich spin-dependent phenomena (Hasan and Kane, 2010; Qi and Zhang, 2011). Three-dimensional topological insulators are characterized by their unique electronic structures. They have an insulating gap in the bulk and possess gapless surface states [Fig. 27(c)]. The spin orientation of topological surface-state electrons is in the surface plane and locked perpendicular to their momenta due to spin-orbit coupling. Thus, it rotates along the constant-energy contour [Fig. 27(d)].

Both constant-energy contours of the Rashba spin-split surface state [Fig. 27(b)] and the topological surface state [Fig. 27(d)] show helical spin texture. In the presence of nonmagnetic scatterers on the surface, it is expected that

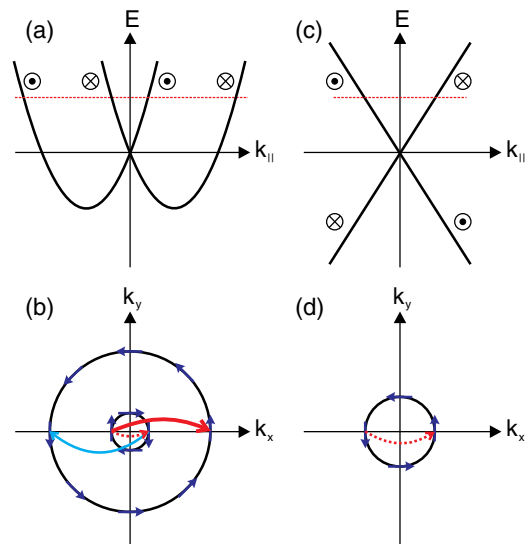


FIG. 27 (color online). Schematics of dispersion relations and constant-energy contours of [(a), (b)] Rashba spin-split surface states and [(c), (d)] topological surface states. The constant-energy contours [(c), (d)] correspond to a cut at the dashed line in (a) and (b), respectively. The arrows on the constant-energy contours indicate the spin direction at corresponding wave vectors. In (b), scattering between states with the same spin direction (solid arrows) is allowed, but scattering between those with opposite spin (dashed arrow) is prohibited. In (d), back-scattering (dashed arrow) never occurs since states at k and $-k$ have opposite spin directions.

spin-dependent or spin-conserving scattering will occur due to time-reversal symmetry. For example, in Fig. 27(b) back-scattering between the two contours with the same spin direction is allowed while it is prohibited in Fig. 27(d) because states at k and $-k$ have opposite spin directions.¹⁰ Therefore, the situation in Fig. 27(b) leads to formation of standing waves in the LDOS around the scatterers, but that in Fig. 27(d) does not. Note that this LDOS modulation is not spin polarized, unlike LDOS modulations on Co islands on Cu(111) discussed in Sec. IV.C, because there are two scattering channels with opposite spins for this case [Fig. 27(b)].

This spin-dependent or spin-conserving scattering has been observed using FT-STM and STS techniques on systems with strong spin-orbit coupling, Bi(110) (Pascual *et al.*, 2004; Kim *et al.*, 2005), Bi/Ag(111) (Hirayama, Aoki, and Kato, 2011; El-Kareh *et al.*, 2013), Bi/Cu(111) (Steinbrecher *et al.*, 2013), Bi_{1-x}Sb_x alloys (Roushan *et al.*, 2009), and Bi₂Te₃ (Zhang *et al.*, 2009; Alpichshev *et al.*, 2010). Figure 28 shows an example of such measurements (Roushan *et al.*, 2009). A FT-STS map of Bi_{1-x}Sb_x alloys at the Fermi energy shows some features that reflect scattering processes of surface-state electrons at the surface. This experimental FT-STS map is reproducible in simulated FT-STS maps only when spin-dependent scattering is taken into account. Alpichshev *et al.* (2010) found that LDOS modulations on Bi₂Te₃ are strongly suppressed within an energy

¹⁰Note that whether or not backscattering takes place strongly depends on the band structures of systems (Pascual *et al.*, 2004).

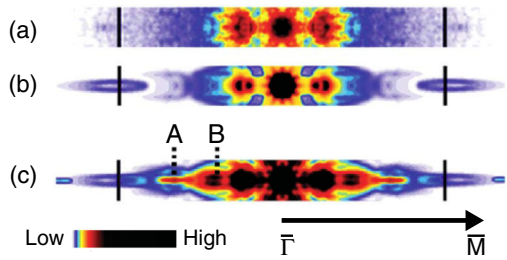


FIG. 28 (color online). FT-STs measurements on $\text{Bi}_{1-x}\text{Sb}_x$ alloys. (a) Experimental FT-STs map of $\text{Bi}_{1-x}\text{Sb}_x$ alloys at the Fermi energy along the $\bar{\Gamma}$ - \bar{M} direction. (b), (c) Simulated FT-STs maps with and without spin-dependent scattering effect, respectively. In (c), two additional high-intensity points (A and B) appear in comparison with (b). They originate from scattering between states with opposite spins. Adapted from Roushan *et al.*, 2009.

range where the constant-energy contour of surface states has a circular shape as in Fig. 27(d). They ascribed this result to the lack of backscattering in helical spin texture due to time-reversal symmetry.

One interesting question arises. If time-reversal symmetry is violated by the introduction of magnetic scatterers or magnetic fields, where spin-flip scattering is allowed, how does the scattering process and resulting LDOS modulation of spin-polarized surface-state electrons change? It would be expected that the time-reversal-symmetry breaking will open new electron scattering channels where spin-flip scattering occurs, and it will give rise to corresponding LDOS modulations. In Fig. 27(d), for example, backscattering between states at k and $-k$ would occur and LDOS modulations with a spatial period of π/k could be seen in differential conductance maps by STM and STS.

Recent theoretical studies predict that a magnetic scatterer does not induce any additional effect on LDOS modulations in comparison with the nonmagnetic case even though it triggers spin-flip scattering (Guo and Franz, 2010; Stróżecka, Eiguren, and Pascual, 2011; Liu, Qi, and Zhang, 2012; Lounis, Bringer, and Blügel, 2012). A magnetic scatterer flips the spin of incident electronic waves and reflects electronic waves with opposite spin, that is, backscattering between opposite-spin states takes place. However, the interference of the incident and reflected electronic waves leads to a constant LDOS since they have orthogonal spin. Therefore, the resulting LDOS modulations are the same for magnetic and nonmagnetic scatterers and do not depend on the presence of spin-flip backscattering.

Instead, the theoretical studies propose an interesting consequence induced by time-reversal-symmetry breaking (Guo and Franz, 2010; Stróżecka, Eiguren, and Pascual, 2011; Liu, Qi, and Zhang, 2012; Lounis, Bringer, and Blügel, 2012). The interference of incident and spin-flip backscattered electronic waves induces a rotation of the spin-polarized LDOS (which is a vector; see Sec. II.C). This is a clear fingerprint of the presence of spin-flip backscattering in systems with strong spin-orbit coupling. Conventional FT-STM with a nonmagnetic tip can neither detect this rotation of the spin-polarized LDOS, nor distinguish LDOS modulations induced by magnetic and nonmagnetic scatterers. Spin-polarized FT-STM with a magnetic

tip is necessary to identify the fingerprint. Theory also predicts that a magnetic field induces spin-polarized LDOS modulations in a system of two nonmagnetic adatoms on strong spin-orbit-coupling surfaces (Fu, Zhang, and Li, 2011, 2012). To the best of our knowledge, spin-polarized experiments of LDOS modulations on systems with strong spin-orbit coupling have not been reported.

VI. IMPACT OF SPIN-DEPENDENT ELECTRON CONFINEMENT ON TRANSPORT PROPERTIES

A. Experiments on spatially modulated TMR

A combined study of SP-STM and STS measurements and *ab initio* calculations has demonstrated that the spin polarization within a single Co island is not homogeneous but spatially modulated due to the spin-polarized quantum interference (Oka *et al.*, 2010), as discussed in Sec. IV.C. As a result of the spatial modulation of the spin polarization of the sample, the tunneling current is expected to also be spatially modulated within a Co island. This would induce a spatial modulation of transport properties, such as the TMR. This effect has been observed experimentally and described by theory (Oka *et al.*, 2011). It is reviewed in the following.

The sample exploited is a single Co island on Cu(111) [inset of Fig. 29(a)], which exhibits a spatial modulation of the spin polarization due to confinement of majority *s-p* surface-state electrons as discussed in Sec. IV.C. First, the dependence of the tunneling current on the magnetic configuration of a magnetic tunnel junction system is examined. A hysteresis loop of the tunneling current is obtained by plotting a tunneling current at -0.27 V as a function of the magnetic field [Figs. 29(a) and 29(b)]. The tunneling current clearly varies for parallel and antiparallel magnetic configurations of the Co island with respect to a magnetic tip, which is ascribed to the so-called TMR effect (Julliere, 1975; Miyazaki and Tezuka, 1995; Moodera *et al.*, 1995). The junction resistance changes between 290 M Ω for the AP state and 190 M Ω for the P state at -0.27 V [Fig. 29(b)]. The TMR ratio, defined as (Parkin *et al.*, 2004; Yuasa *et al.*, 2004)

$$\frac{R_{AP} - R_P}{R_P} = \frac{I_P - I_{AP}}{I_{AP}}, \quad (31)$$

is extracted, where R_{AP} and R_P are the tunnel resistances and I_{AP} and I_P are the tunneling currents in the AP and P states, respectively. The TMR depends on the electronic properties of both electrodes (the Co island and the tip in this case) (De Teresa *et al.*, 1999; Tsymbal, Mryasov, and LeClair, 2003). Figure 29(c) reveals a strong energy dependence of the TMR ratio measured at the center of the Co island, which reflects the spin-resolved electronic LDOS of the Co island (Diekhöner *et al.*, 2003), and a maximum positive TMR ratio of $\sim 50\%$ at -0.27 V.

Figure 30(a) shows TMR spectra obtained at three different positions. All spectra show a similar bias-voltage dependence, but distinct differences in the magnitude are found. To see the position dependence of the TMR ratio within the island, a map of the TMR ratio at $+0.06$ V [Fig. 30(c)] is calculated from maps of the tunneling current for the P and AP states

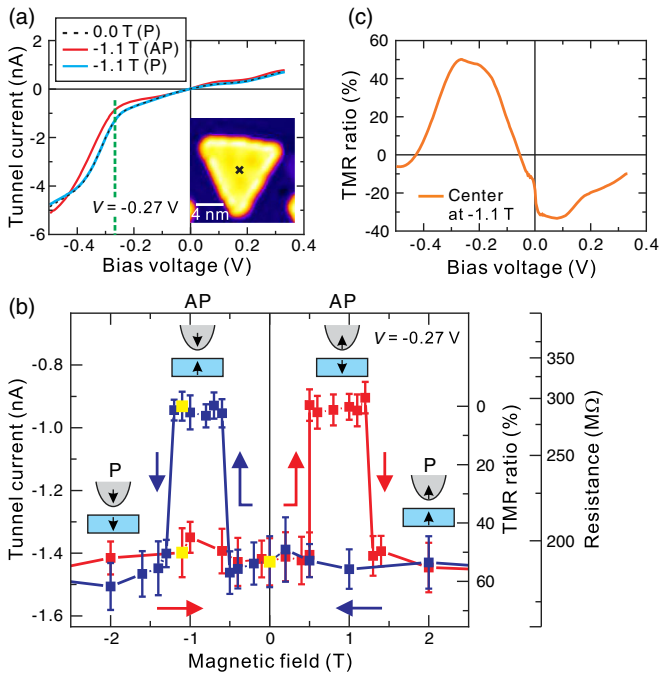


FIG. 29 (color online). Tunneling current, its magnetization dependence, and TMR spectrum measured on a bilayer Co island on Cu(111) at 8 K. (a) $I(V)$ curves measured at the center of the Co island shown in the inset at different magnetic fields. $V_{\text{stab}} = +0.5$ V, $I_{\text{stab}} = 1.0$ nA. The dashed line at -0.27 V gives the bias voltage of the measurement of the hysteresis curve in (b). The inset shows a constant-current STM image of the Co island on Cu(111). $V_S = -0.1$ V, $I = 1.0$ nA. (b) Hysteresis loop of the tunneling current measured at the center of the Co island. The gray sections of the hysteresis loop correspond to upward and downward sweeps of the magnetic field. Dots in the loop indicate measurement conditions of the $I(V)$ curves shown in (a). Schematics indicate the magnetization orientations of the Co island and the magnetic tip. (c) TMR spectrum measured at the center of the Co island, which is obtained from the two $I(V)$ curves at -1.1 T in (a) using Eq. (31). From Oka *et al.*, 2011.

[Figs. 31(a) and 31(b)] using Eq. (31). It reveals negative TMR ratios and a clear spatial modulation of the TMR ratio in the center region of the island. The modulation pattern is very similar to that of the spin polarization found in an $A_{dI/dV}$ map [see Fig. 4(d)]. The intimate relation between spin polarization and TMR ratio becomes evident from the calculation of spin-dependent transport Eq. (31) with Eq. (16),

$$\frac{I_P - I_{AP}}{I_{AP}} = \frac{2P_T \tilde{P}_S}{1 - P_T \tilde{P}_S}, \quad (32)$$

where \tilde{P}_S is the energy integral of the spin polarization of the sample between E_F and $E_F + eV$. This result demonstrates that the spin-polarized quantum interference induces a spatial modulation of the TMR within the single Co island.¹¹

¹¹It is noted that the opposite sign of the TMR ratio to the spin polarization is attributed to a negative spin polarization of the magnetic tip used in the measurements (for details, see Figs. 14 and 15).

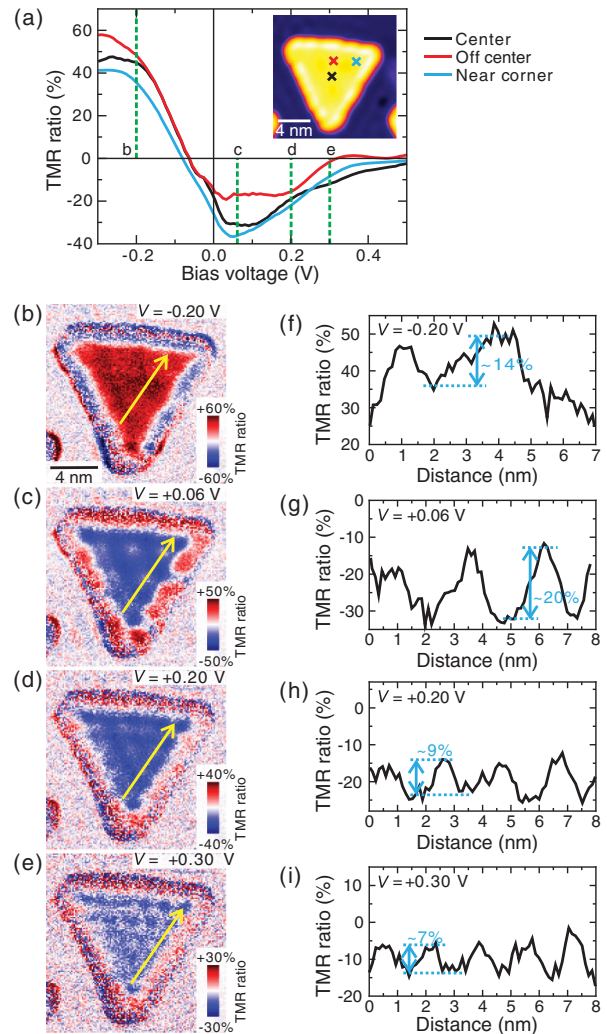


FIG. 30 (color). Spatial modulation of TMR within a single Co island and its energy dependence. (a) TMR spectra as a function of bias voltage V taken at three different positions on the Co island of Fig. 29 shown in the inset. Corresponding positions are indicated by crosses. Each TMR spectrum is obtained from two $I(V)$ curves measured at parallel (P) and antiparallel (AP) magnetization configurations at -1.1 T, using Eq. (31). (b)–(e) Maps of TMR ratio obtained at the indicated voltages. ($V_{\text{stab}} = +0.5$ V, $I_{\text{stab}} = 1.0$ nA, and -1.1 T). The selected voltages are indicated by green dashed lines in (a). (f)–(i) Line profiles, averaged over six adjacent lines for improved signal-to-noise ratio, of the TMR ratio images along the yellow arrows in (b)–(e). Adapted from Oka *et al.*, 2011.

Since the spatial modulation of the spin polarization changes with energy as seen in Fig. 13, similar changes in the TMR modulation would be expected. Maps of the TMR ratio¹² for different bias voltages are shown in Figs. 30(b)–30(e). All maps show a clear spatial modulation of the TMR ratio and clear changes of the modulation patterns can be seen. Line profiles along the yellow arrows allow a quantitative analysis

¹²At a given energy, the tip spin polarization (P_T) can be assumed as constant. Thus, maps of the TMR ratio reflect spatial variation of the energy integral of the sample spin polarization (\tilde{P}_S).

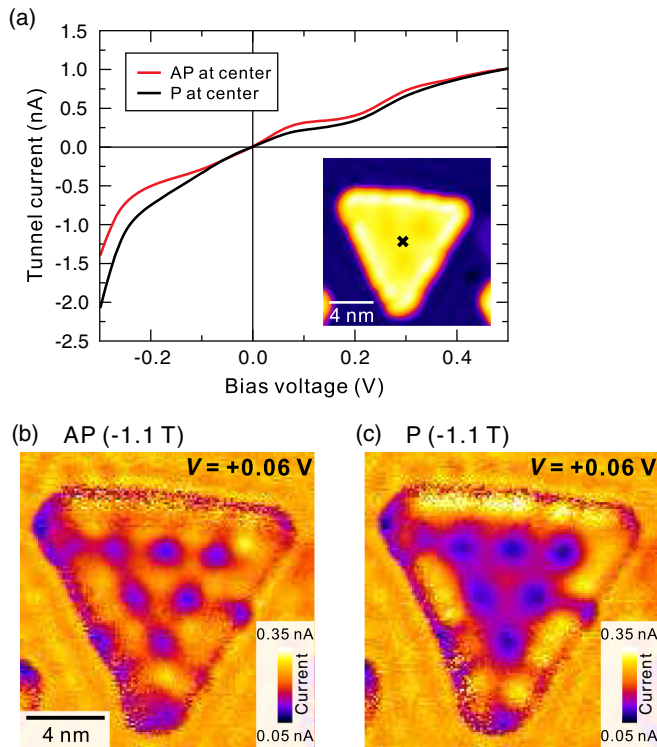


FIG. 31 (color online). Constituent measurements for a TMR spectrum and a TMR map of a Co island. (a) $I(V)$ curves measured at the center of the Co island shown in the inset at -1.1 T for antiparallel (AP) and parallel (P) magnetization configurations. $V_{\text{stab}} = +0.5$ V, $I_{\text{stab}} = 1.0$ nA. These $I(V)$ curves are the basis for the TMR spectrum shown in Fig. 30(a). The inset shows a constant-current STM image of a Co island on Cu(111). $V_S = -0.1$ V, $I = 1.0$ nA. (b), (c) Tunnel-current images (constant height) of the Co island measured at $V = +0.06$ V in the AP and P states, respectively. $V_{\text{stab}} = +0.5$ V, $I_{\text{stab}} = 1.0$ nA, and -1.1 T. Both images show a spatial modulation of the tunneling current. The TMR map presented in Fig. 30(c) is calculated from these two images using Eq. (31).

of the TMR maps [Figs. 30(f)–30(i)]. At $+0.06$ V, the TMR ratio within the island is modulated with an amplitude of $\sim 20\%$ and a spacing between maxima and minima of ~ 1.3 nm. The amplitude and the spacing become smaller with increasing bias voltage, and at $+0.30$ V a modulation amplitude of $\sim 7\%$ with a spacing between maxima and minima of ~ 0.7 nm, which corresponds to a three-atomic distance, is shown.

The spin polarization within the Co island also drastically changes its sign with energy (Fig. 13), whereas the TMR within the island does not show such great changes in its sign, but it exhibits a positive and negative sign below and above -0.05 V, respectively (Fig. 30). This finding can be understood by considering the difference in the property of the differential conductance and the tunneling current. In the case of spin-polarized tunneling, dI/dV carries a term of $\tilde{m}_S(V)$ in Eq. (19), which is the spin-polarized LDOS at $E_F + eV$, and therefore, the spin polarization $P_S(V)$ is an energy-resolved quantity. In contrast, the tunneling current contains a term of $\tilde{m}_S(V)$ in Eq. (16), which is an energy integral of the spin-polarized LDOS between E_F and $E_F + eV$ [Eq. (17)].

Thus, the TMR depends on the energy integral of the spin polarization between E_F and $E_F + eV$, $\tilde{P}_S(V)$. The TMR within the island shows positive values below -0.05 V, where the minority d state dominates $\tilde{P}_S(V)$, while it exhibits negative ones above -0.05 V, where the majority s - p surface state governs $\tilde{P}_S(V)$.¹³ These results are explained in light of spin-dependent transport properties with the help of *ab initio* calculations, which will be reviewed in Sec. VI.B.

The impact of the spin-dependent Smoluchowski effect on the TMR was investigated (Polyakov *et al.*, 2012). Figure 32 shows a line scan of the TMR ratio at -0.3 V obtained across a step edge of a Co island on Cu(111), which is indicated by an arrow in Fig. 25. The line scan elucidates a local variation of the TMR ratio from -10% at the upper part of the step edge to $+10\%$ at the bottom of the step edge, which is ascribed to a spatial variation of the spin polarization induced by the spin-dependent Smoluchowski effect. This result indicates that step edges in a magnetic tunnel junction cause a reduction of the total TMR ratio of the system, and this points at the importance of atomically well-controlled growth in the fabrication of magnetic tunnel junction devices. It also reflects that boundary effects need to be considered in the nanometer range toward the edge of a nanostructure. Near the boundary a very different TMR ratio from that in the center region may result and this will be detrimental when the overall structure size shrinks to the few-nanometer range.

B. *Ab initio* based theory of spin-dependent transport

To understand the energy dependence of the TMR ratio in Fig. 29, *ab initio* calculations of spin-dependent transport properties are performed (Oka *et al.*, 2011) using the SMEAGOL code (Rocha *et al.*, 2005, 2006; Rungger and Sanvito, 2008). Figure 33(a) presents the TMR ratio as a function of the bias voltage, which is calculated using a model of an STM tunnel junction as depicted in the inset of Fig. 33(a). A comparison of the calculated TMR ratio [Fig. 33(a)] with the experimental one [Fig. 29(c)] indicates a good qualitative agreement, suggesting that the calculations can provide the electronic origin of the energy dependence of the TMR ratio. An important property to be considered is the transmission coefficient because its energy integral gives the tunneling current. Figure 33(b) shows spin-resolved transmission coefficients for P and AP configurations at different bias voltages. The data reveal that transmission peaks (labeled as 1 and 2) predominantly contribute to the tunneling current and consequently govern the amplitude and the sign of the TMR ratio. The transmission peak 1 is the main cause of a negative TMR ratio at 0 V and the peak 2 causes a large positive TMR ratio at -0.2 V. Since the transmission coefficient is linked to the transition between electronic states of the Cr tip and the Co island, the projected DOS (PDOS) of a Cr atom at the tip apex and a Co atom under the apex can give a hint toward the origin of the transmission peaks. Figure 33(c) shows plots of the PDOSs on s - p orbitals of the Cr atom (tip) and the Co atom (island). They focus on s - p states because at the typical tip-sample distance of 0.5 nm, the effect of d states

¹³Note the same as footnote 11.

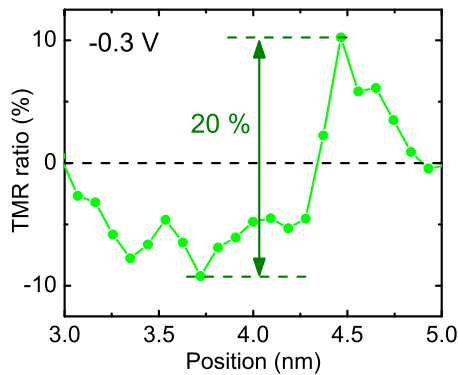


FIG. 32 (color online). Line scan of the TMR ratio measured along the arrow in Fig. 25 at -0.3 V. From Polyakov *et al.*, 2012.

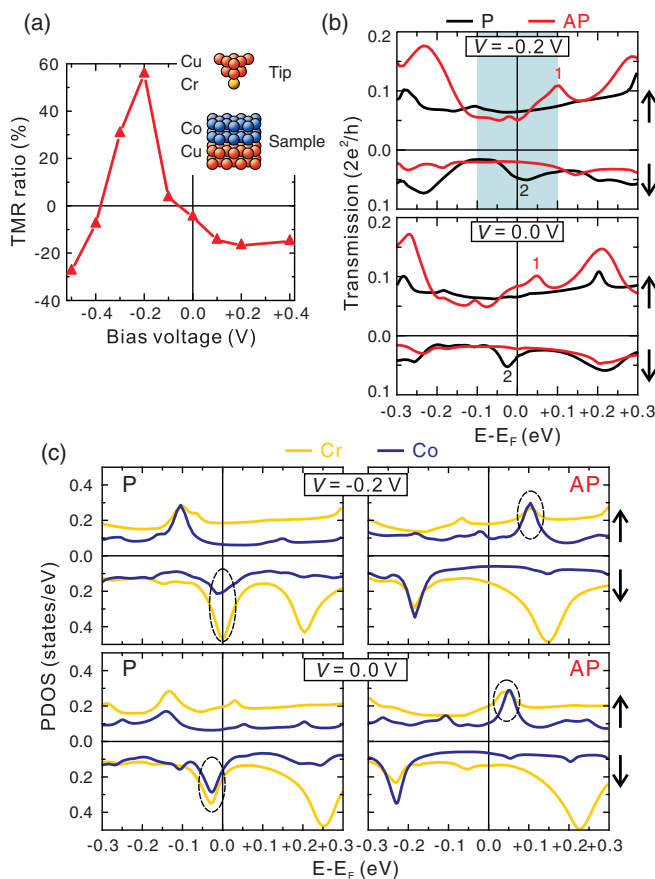


FIG. 33 (color online). Energy dependence of spin-dependent transport properties. (a) Calculated energy-dependent TMR ratio. The inset shows the model of the tip and sample used in our calculations. (b) Spin-resolved transmission coefficient as a function of energy for both P and AP configurations at different bias voltages. The colored areas denote the bias window within which the transmission function is integrated to obtain the current. (c) s - p projected density of states (PDOS) of a Cr atom at a tip apex and a Co atom under the apex in P and AP configurations at bias voltages of $V = -0.2$ V (upper panel) and $V = 0.0$ V (lower panel). Up and down arrows indicate spin-up and spin-down channels, respectively. From Oka *et al.*, 2011.

on the transmission is small whereas s - p states give a dominant contribution (Zener, 1951a, 1951b; Tao *et al.*, 2009). At 0 V, peaks for both PDOSs can be found in the spin-up channel for the AP state at $+0.05$ V, where the transmission peak 1 is found. Therefore, the electronic origin of the transmission peak 1 is identified as the transition of spin-up s - p states between the Cr atom and the Co atom at the AP state. At -0.2 V, in the spin-down channel for the P state, both the Co and the Cr s - p states shift up in energy toward the Fermi energy and the transition between these states gives rise to the transmission peak 2. They argue that the bias voltage leads to not only a relative shift of the energy position of the PDOS but also a change in the intensity of the PDOS because different atomic orbitals respond differently to the electric field induced by the external bias voltage. This aspect is usually neglected when we discuss the working principle of STM or interpret differential conductance data. This effect has an important impact for the understanding of the energy dependence of spin-dependent transport properties. A word of caution appears well justified in appreciating that the STM itself, due to the application of sizable electric fields (~ 1 V/nm), induces changes of the electronic structure of the sample via the Stark effect (Becker, Golovchenko, and Swartzentruber, 1985; Binnig *et al.*, 1985; Limot *et al.*, 2003; Kröger *et al.*, 2004).

VII. CONCLUDING REMARKS AND FUTURE DEVELOPMENTS

This review provides a compilation of numerous examples for the experimental study of electron confinement in nanostructures, and it shows how quantitative insight into the electron dispersion relation is obtained from energy-dependent spatially resolved STM experiments. The link between the measured differential conductance data and the calculated density of states of nanostructures is elucidated. We discuss the quantization of the electron wave vector induced by electron confinement, giving rise to an electron dispersion relation, which is not continuous but discrete in the wave vector. The characteristic length scale of the quantization condition can be ascribed to a linear dimension such as the width of a substrate terrace, the diameter of a hexagonal depression, or the geometric altitude of a triangular island.

Careful quantitative analysis reveals that the often-cited parabolic dispersion relation in confined electronic systems is just an approximation. Deviations from a parabolic dispersion are observed in both experiment and theory. The analysis points out the importance of hybridization between electronic surface and bulk states. This leads to a reduced curvature of the dispersion relation at higher energies, which is of the order of 0.3 eV above the Fermi energy for Cu(111).

Spin-dependent electron scattering and electron confinement studied by STM and SP-STM are reviewed. Spin-dependent measurements of the differential conductance in individual nanostructures in connection with theory offer quantitative insights into spin polarization on the nanoscale. The magnitude and sign of the spin polarization vary on the nanometer scale, and this variation is energy dependent. Theory indicates that the energy dependence of the relative magnitude of the DOS of majority and minority electrons

is an important aspect in understanding the variation of spin polarization in a given nanostructure. The regular spatial variation of the spin polarization can be ascribed to spin-dependent electron confinement. Peculiar electronic states, localized at the rim of nanostructures, may also induce variations of the spin polarization near the edge of nanostructures.

Magnetic adatoms can induce spin polarization in non-magnetic substrates, e.g., noble metal substrates and topological insulators. The induced spin polarization leads to a long-range RKKY-like magnetic interaction between magnetic adatoms. Theory predicts that the long-range magnetic interaction can be tailored by surrounding magnetic adatoms with an atomic corral.

The implications of spatial variation of the spin polarization within a single nanostructure and near the edge of nanostructures for the electronic transport properties, such as differential conductance, tunneling current, and TMR, are discussed. Variations of these properties are sizable, and they may induce, e.g., a variation of the TMR ratio by 20% on the nanometer scale.

Here we review spatially varying spin-dependent electronic properties of individual nanostructures and at surfaces on the nanoscale. The roles of spatial variation of the spin polarization and of structural relaxations in nanostructures on the magnetic properties, such as the magnetic anisotropy and the magnetization reversal mode, of a single nanostructure have not yet been fully accounted for (Sander *et al.*, 2013). The corresponding calculations are very demanding, due to the lack of symmetry, as induced by structural and electronic relaxations near the nanostructure boundaries. Also the theoretical description of the magnetization reversal in a nanostructure with some 1000 atoms represents a true challenge for *ab initio* based theory. Ultimately we strive for a theoretical description of all experimental aspects, where also the magnetization reversal process can be described by theory (Sukhov and Berakdar, 2008; D. S. G. Bauer *et al.*, 2011; Böttcher, Ernst, and Henk, 2011). More work along these lines is called for to advance our understanding of the corresponding physical mechanisms on the electronic level.

Finally, we foresee that the application of spin-resolved spectroscopy by STM will contribute to the understanding of unconventional superconductivity in Fe-containing superconductors in the framework of quasiparticle interference (Hanaguri *et al.*, 2010; Hoffman, 2011; Allan *et al.*, 2012). Corresponding experiments are currently under way, where spectroscopy in the 10 mK temperature range will be exploited (Song *et al.*, 2010; Singh *et al.*, 2013). SP-STM will also contribute to the study of peculiar spin-dependent surface electronic properties of topological insulators and impurity scattering effects (Biswas and Balatsky, 2010; Guo and Franz, 2010; Fu, Zhang, and Li, 2011, 2012; Stróżecka, Eiguren, and Pascual, 2011; Liu, Qi, and Zhang, 2012; Lounis, Bringer, and Blügel, 2012).

ACKNOWLEDGMENTS

We thank J. Borme, H. F. Ding, F. Donati, P. A. Ignatiev, Y. Nahas, N. N. Negulyaev, L. Niebergall, S. Ouazi,

O. P. Polyakov, G. Rodary, O. V. Stepanyuk, K. Tao, and S. Wedekind for fruitful discussions, and N. Kurowsky and H. Menge for expert technical support. Support from Deutsche Forschungsgemeinschaft Grant No. SFB 762 is gratefully acknowledged.

REFERENCES

- Allan, M. P., A. W. Rost, A. P. Mackenzie, Y. Xie, J. C. Davis, K. Kihou, C. H. Lee, A. Iyo, H. Eisaki, and T.-M. Chuang, 2012, "Anisotropic energy gaps of iron-based superconductivity from intraband quasiparticle interference in LiFeAs," *Science* **336**, 563.
- Alpichshev, Z., J. G. Analytis, J.-H. Chu, I. R. Fisher, Y. L. Chen, Z. X. Shen, A. Fang, and A. Kapitulnik, 2010, "STM imaging of electronic waves on the surface of Bi₂Te₃: Topologically protected surface states and hexagonal warping effects," *Phys. Rev. Lett.* **104**, 016401.
- Altfeder, I. B., K. A. Matveev, and D. M. Chen, 1997, "Electron fringes on a quantum wedge," *Phys. Rev. Lett.* **78**, 2815.
- Alvarado, S. F., and P. Renaud, 1992, "Observation of spin-polarized-electron tunneling from a ferromagnet into GaAs," *Phys. Rev. Lett.* **68**, 1387.
- Ando, T., A. B. Fowler, and F. Stern, 1982, "Electronic properties of two-dimensional systems," *Rev. Mod. Phys.* **54**, 437.
- Asonen, H., M. Lindroos, M. Pessa, R. Prasad, R. S. Rao, and A. Bansil, 1982, "Angle-resolved photoemission study of (100), (110), and (111) surfaces of Cu_{0.9}Al_{0.1}: Bulk and surface electronic structure of the alloy," *Phys. Rev. B* **25**, 7075.
- Asonen, H., and M. Pessa, 1981, "Photoemission observation of an intrinsic surface-state band in a disordered Cu_{0.9}Al_{0.1} (111) alloy," *Phys. Rev. Lett.* **46**, 1696.
- Assig, M., M. Etzkorn, A. Enders, W. Stiepany, C. R. Ast, and K. Kern, 2013, "A 10 mK scanning tunneling microscope operating in ultra high vacuum and high magnetic fields," *Rev. Sci. Instrum.* **84**, 033903.
- Ast, C. R., 2013 (private communication).
- Aulbach, J., J. Schäfer, S. C. Erwin, S. Meyer, C. Loho, J. Settlein, and R. Claessen, 2013, "Evidence for long-range spin order instead of a Peierls transition in Si(553)-Au chains," *Phys. Rev. Lett.* **111**, 137203.
- Avouris, P., and I.-W. Lyo, 1994, "Observation of quantum-size effects at room-temperature on metal-surfaces with STM," *Science* **264**, 942.
- Avouris, P., I.-W. Lyo, and P. Molinàs-Mata, 1995, "STM studies of the interaction of surface state electrons on metals with steps and adsorbates," *Chem. Phys. Lett.* **240**, 423.
- Avouris, P., I.-W. Lyo, R. E. Walkup, and Y. Hasegawa, 1994, "Real space imaging of electron scattering phenomena at metal surfaces," *J. Vac. Sci. Technol. B* **12**, 1447.
- Baibich, M. N., J. M. Broto, A. Fert, F. N. Van Dau, F. Petroff, P. Etienne, G. Creuzet, A. Friederich, and J. Chazelas, 1988, "Giant magnetoresistance of (001)Fe/(001)Cr magnetic superlattices," *Phys. Rev. Lett.* **61**, 2472.
- Bardeen, J., 1961, "Tunnelling from a many-particle point of view," *Phys. Rev. Lett.* **6**, 57.
- Bauer, D. S. G., P. Mavropoulos, S. Lounis, and S. Blügel, 2011, "Thermally activated magnetization reversal in monatomic magnetic chains on surfaces studied by classical atomistic spin-dynamics simulations," *J. Phys. Condens. Matter* **23**, 394204.
- Bauer, U., M. Dąbrowski, M. Przybylski, and J. Kirschner, 2011, "Experimental confirmation of quantum oscillations of magnetic anisotropy in Co/Cu(001)," *Phys. Rev. B* **84**, 144433.

- Baumberger, F., M. Hengsberger, M. Muntwiler, M. Shi, J. Krempasky, L. Patthey, J. Osterwalder, and T. Greber, 2004, "Localization of surface states in disordered step lattices," *Phys. Rev. Lett.* **92**, 196805.
- Becker, M., and R. Berndt, 2010, "Scattering and lifetime broadening of quantum well states in Pb films on Ag(111)," *Phys. Rev. B* **81**, 205438.
- Becker, R. S., J. A. Golovchenko, and B. S. Swartzentruber, 1985, "Electron interferometry at crystal surfaces," *Phys. Rev. Lett.* **55**, 987.
- Bendounan, A., H. Cercellier, B. Kierren, Y. Fagot-Revurat, V. Y. Yurov, and D. Malterre, 2003, "Monitoring the local atomic structure by surface states spectroscopy," *Europhys. Lett.* **64**, 392.
- Berbil-Bautista, L., S. Krause, M. Bode, and R. Wiesendanger, 2007, "Spin-polarized scanning tunneling microscopy and spectroscopy of ferromagnetic Dy(0001)/W(110) films," *Phys. Rev. B* **76**, 064411.
- Berland, K., T. L. Einstein, and P. Hyldgaard, 2012, "Response of the shockley surface state to an external electrical field: A density-functional theory study of Cu(111)," *Phys. Rev. B* **85**, 035427.
- Bertacco, R., and F. Ciccacci, 1999, "Oxygen-induced enhancement of the spin-dependent effects in electron spectroscopies of Fe(001)," *Phys. Rev. B* **59**, 4207.
- Bertacco, R., D. Onofrio, and F. Ciccacci, 1999, "A novel electron spin-polarization detector with very large analyzing power," *Rev. Sci. Instrum.* **70**, 3572.
- Besocke, K., B. Krahl-Urban, and H. Wagner, 1977, "Dipole moments associated with edge atoms; a comparative study on stepped Pt, Au and W surfaces," *Surf. Sci.* **68**, 39.
- Besocke, K., and H. Wagner, 1973, "Adsorption of W on W(110): Work-function reduction and island formation," *Phys. Rev. B* **8**, 4597.
- Bibes, M., J. E. Villegas, and A. Barthélémy, 2011, "Ultrathin oxide films and interfaces for electronics and spintronics," *Adv. Phys.* **60**, 5.
- Binasch, G., P. Grünberg, F. Saurenbach, and W. Zinn, 1989, "Enhanced magnetoresistance in layered magnetic structures with antiferromagnetic interlayer exchange," *Phys. Rev. B* **39**, 4828.
- Binnig, G., K. H. Frank, H. Fuchs, N. Garcia, B. Reihl, H. Rohrer, F. Salvan, and A. R. Williams, 1985, "Tunneling spectroscopy and inverse photoemission: Image and field states," *Phys. Rev. Lett.* **55**, 991.
- Binnig, G., H. Rohrer, C. Gerber, and E. Weibel, 1982a, "Surface studies by scanning tunneling microscopy," *Phys. Rev. Lett.* **49**, 57.
- Binnig, G., H. Rohrer, C. Gerber, and E. Weibel, 1982b, "Tunneling through a controllable vacuum gap," *Appl. Phys. Lett.* **40**, 178.
- Binnig, G., H. Rohrer, C. Gerber, and E. Weibel, 1983, " 7×7 reconstruction on Si(111) resolved in real space," *Phys. Rev. Lett.* **50**, 120.
- Biswas, R. R., and A. V. Balatsky, 2010, "Impurity-induced states on the surface of three-dimensional topological insulators," *Phys. Rev. B* **81**, 233405.
- Bode, M., 2003, "Spin-polarized scanning tunnelling microscopy," *Rep. Prog. Phys.* **66**, 523.
- Bode, M., M. Getzlaff, and R. Wiesendanger, 1998, "Spin-polarized vacuum tunneling into the exchange-split surface state of Gd(0001)," *Phys. Rev. Lett.* **81**, 4256.
- Bonnell, D., 2001, Ed., *Scanning Probe Microscopy and Spectroscopy Theory, Techniques and Applications* (Wiley-VCH, New York).
- Borisov, A. G., T. Hakala, M. J. Puska, V. M. Silkin, N. Zabala, E. V. Chulkov, and P. M. Echenique, 2007, "Image potential states of supported metallic nanoislands," *Phys. Rev. B* **76**, 121402.
- Böttcher, D., A. Ernst, and J. Henk, 2011, "Atomistic magnetization dynamics in nanostructures based on first principles calculations: application to Co nanoislands on Cu(111)," *J. Phys. Condens. Matter* **23**, 296003.
- Braun, J., and M. Donath, 2002, "Contest between surface resonances and surface states at 3d ferromagnets," *Europhys. Lett.* **59**, 592.
- Braun, K.-F., and K.-H. Rieder, 2008, "Ni(111) surface state observed with scanning tunneling microscopy," *Phys. Rev. B* **77**, 245429.
- Briggs, G. A. D., and A. J. Fisher, 1999, "Stm experiment and atomistic modelling hand in hand: individual molecules on semiconductor surfaces," *Surf. Sci. Rep.* **33**, 1.
- Brovko, O., W. Hergert, and V. Stepanyuk, 2009, "Quantum confinement on nanoislands as a tool for tailoring exchange interaction: An ab initio study," *Phys. Rev. B* **79**, 205426.
- Brovko, O. O., P. Ruiz-Díaz, T. R. Dasa, and V. S. Stepanyuk, 2014, "Controlling magnetism on metal surfaces with non-magnetic means: electric fields and surface charging," *J. Phys. Condens. Matter* **26**, 093001.
- Brune, H., 1998, "Microscopic view of epitaxial metal growth: nucleation and aggregation," *Surf. Sci. Rep.* **31**, 125.
- Bürgi, L., H. Brune, O. Jeandupeux, and K. Kern, 2000, "Quantum coherence and lifetimes of surface-state electrons," *J. Electron Spectrosc. Relat. Phenom.* **109**, 33.
- Bürgi, L., O. Jeandupeux, H. Brune, and K. Kern, 1999, "Probing hot-electron dynamics at surfaces with a cold scanning tunneling microscope," *Phys. Rev. Lett.* **82**, 4516.
- Bürgi, L., O. Jeandupeux, A. Hirstein, H. Brune, and K. Kern, 1998, "Confinement of surface state electrons in Fabry-Pérot resonators," *Phys. Rev. Lett.* **81**, 5370.
- Bürgi, L., L. Petersen, H. Brune, and K. Kern, 2000, "Noble metal surface states: deviations from parabolic dispersion," *Surf. Sci.* **447**, L157.
- Bychkov, Y. A., and E. I. Rashba, 1984, "Properties of a 2d electron gas with lifted spectral degeneracy," *JETP Lett.* **39**, 78 [http://www.jetpletters.ac.ru/ps/1264/article_19121.shtml].
- Cao, R. X., B. F. Miao, Z. F. Zhong, L. Sun, B. You, W. Zhang, D. Wu, A. Hu, S. D. Bader, and H. F. Ding, 2013, "Two-dimensional quantum diffusion of Gd adatoms in nano-size Fe corrals," *Phys. Rev. B* **87**, 085415.
- Cebollada, A., R. Miranda, C. M. Schneider, P. Schuster, and J. Kirschner, 1991, "Experimental evidence of an oscillatory magnetic coupling in Co/Cu/Co epitaxial layers," *J. Magn. Magn. Mater.* **102**, 25.
- Cercellier, H., Y. Fagot-Revurat, B. Kierren, F. Reinert, D. Popović, and D. Malterre, 2004, "Spin-orbit splitting of the Shockley state in the Ag/Au(111) interface," *Phys. Rev. B* **70**, 193412.
- Chang, L. L., L. Esaki, and R. Tsu, 1974, "Resonant tunneling in semiconductor double barriers," *Appl. Phys. Lett.* **24**, 593.
- Chen, C. J., 1990a, "Origin of atomic resolution on metal surfaces in scanning tunneling microscopy," *Phys. Rev. Lett.* **65**, 448.
- Chen, C. J., 1990b, "Tunneling matrix elements in three-dimensional space: The derivative rule and the sum rule," *Phys. Rev. B* **42**, 8841.
- Chen, C. J., 1991, "Microscopic view of scanning tunneling microscopy," *J. Vac. Sci. Technol. A* **9**, 44.
- Chen, C. J., 1993, *Introduction to scanning tunneling microscopy* (Oxford University Press, New York).
- Chiang, C.-T., A. Winkelmann, J. Henk, F. Bisio, and J. Kirschner, 2012, "Spin-selective pathways in linear and nonlinear photoemission from ferromagnets," *Phys. Rev. B* **85**, 165137.
- Chikazumi, S., 1997, *Physics of Ferromagnetism*, International Series of Monographs on Physics (Oxford University Press, New York), 2nd ed..

- Clarke, A. R. H., J. B. Pethica, J. A. Nieminen, F. Besenbacher, E. Lægsgaard, and I. Stensgaard, 1996, "Quantitative scanning tunneling microscopy at atomic resolution: Influence of forces and tip configuration," *Phys. Rev. Lett.* **76**, 1276.
- Corbetta, M., S. Ouazi, J. Borome, Y. Nahas, F. Donati, H. Oka, S. Wedekind, D. Sander, and J. Kirschner, 2012, "Magnetic response and spin polarization of bulk Cr tips for in-field spin-polarized scanning tunneling microscopy," *Jpn. J. Appl. Phys.* **51**, 030208.
- Crampin, S., H. Jensen, J. Kröger, L. Limot, and R. Berndt, 2005, "Resonator design for use in scanning tunneling spectroscopy studies of surface electron lifetimes," *Phys. Rev. B* **72**, 035443.
- Crampin, S., J. Kröger, H. Jensen, and R. Berndt, 2005, "Phase coherence length and quantum interference patterns at step edges," *Phys. Rev. Lett.* **95**, 029701.
- Crommie, M. F., C. P. Lutz, and D. M. Eigler, 1993a, "Confinement of electrons to quantum corrals on a metal surface," *Science* **262**, 218.
- Crommie, M. F., C. P. Lutz, and D. M. Eigler, 1993b, "Imaging standing waves in a two-dimensional electron gas," *Nature (London)* **363**, 524.
- Crommie, M. F., C. P. Lutz, and D. M. Eigler, 1993c, "Spectroscopy of a single adsorbed atom," *Phys. Rev. B* **48**, 2851.
- Czerner, M., G. Rodary, S. Wedekind, D. V. Fedorov, D. Sander, I. Mertig, and J. Kirschner, 2010, "Electronic picture of spin-polarized tunneling with a Cr tip," *J. Magn. Magn. Mater.* **322**, 1416.
- Davies, J. H., 1997, *The physics of low-dimensional semiconductors: an introduction* (Cambridge University Press, Cambridge, England).
- Davis, L. C., M. P. Everson, R. C. Jaklevic, and W. Shen, 1991, "Theory of the local density of surface states on a metal: Comparison with scanning tunneling spectroscopy of a Au(111) surface," *Phys. Rev. B* **43**, 3821.
- Davison, S. G., and M. Stęślicka, 1992, *Basic theory of surface states* (Clarendon Press, Oxford).
- de la Figuera, J., J. E. Prieto, C. Ocal, and R. Miranda, 1993, "Scanning-tunneling-microscopy study of the growth of cobalt on Cu(111)," *Phys. Rev. B* **47**, 13 043.
- Delga, A., J. Lagoute, V. Repain, C. Chacon, Y. Girard, M. Marathe, S. Narasimhan, and S. Rousset, 2011, "Electronic properties of Fe clusters on a Au(111) surface," *Phys. Rev. B* **84**, 035416.
- De Teresa, J. M., A. Barthélémy, A. Fert, J. P. Contour, F. Montaigne, and P. Seneor, 1999, "Role of metal-oxide interface in determining the spin polarization of magnetic tunnel junctions," *Science* **286**, 507.
- Didiot, C., V. Cherkez, B. Kierren, Y. Fagot-Revurat, and D. Malterre, 2010, "Bulk state confinement and band folding in nanostructured surfaces," *Phys. Rev. B* **81**, 075421.
- Diekhöner, L., M. A. Schneider, A. N. Baranov, V. S. Stepanyuk, P. Bruno, and K. Kern, 2003, "Surface states of cobalt nanoislands on Cu(111)," *Phys. Rev. Lett.* **90**, 236801.
- Dietl, T., 2010, "A ten-year perspective on dilute magnetic semiconductors and oxides," *Nat. Mater.* **9**, 965.
- Dil, J. H., 2009, "Spin and angle resolved photoemission on non-magnetic low-dimensional systems," *J. Phys. Condens. Matter* **21**, 403001.
- Dingle, R., W. Wiegmann, and C. H. Henry, 1974, "Quantum states of confined carriers in very thin $\text{Al}_x\text{Ga}_{1-x}\text{As} - \text{GaAs} - \text{Al}_x\text{Ga}_{1-x}\text{As}$ heterostructures," *Phys. Rev. Lett.* **33**, 827.
- Donath, M., F. Passek, and V. Dose, 1993, "Surface state contribution to the magnetic moment of Ni(111)," *Phys. Rev. Lett.* **70**, 2802.
- Donati, F., G. Fratesi, M. Passoni, C. S. Casari, A. Mairov, C. E. Bottani, M. I. Trioni, and A. Li Bassi, 2011, "Strain effect on local electronic properties of Fe nanoislands grown on Au(111)," *Phys. Rev. B* **83**, 153404.
- Drakova, D., 2001, "Theoretical modelling of scanning tunnelling microscopy, scanning tunnelling spectroscopy and atomic force microscopy," *Rep. Prog. Phys.* **64**, 205.
- Duke, C., 1969, *Tunneling in solids, Solid state physics: Supplement* (Academic Press, New York).
- Eigler, D. M., and E. K. Schweizer, 1990, "Positioning single atoms with a scanning tunnelling microscope," *Nature (London)* **344**, 524.
- Eiguren, A., B. Hellsing, E. V. Chulkov, and P. M. Echenique, 2003, "Phonon-mediated decay of metal surface states," *Phys. Rev. B* **67**, 235423.
- Eiguren, A., B. Hellsing, F. Reinert, G. Nicolay, E. V. Chulkov, V. M. Silkin, S. Hüfner, and P. M. Echenique, 2002, "Role of bulk and surface phonons in the decay of metal surface states," *Phys. Rev. Lett.* **88**, 066805.
- El-Kareh, L., P. Sessi, T. Bathon, and M. Bode, 2013, "Quantum interference mapping of Rashba-split Bloch states in Bi/Ag(111)," *Phys. Rev. Lett.* **110**, 176803.
- Erwin, S. C., and F. J. Himpsel, 2010, "Intrinsic magnetism at silicon surfaces," *Nat. Commun.* **1**, 58.
- Esaki, L., 1958, "New phenomenon in narrow germanium p - n junctions," *Phys. Rev.* **109**, 603.
- Everson, M. P., R. C. Jaklevic, and W. Shen, 1990, "Measurement of the local density of states on a metal surface: Scanning tunneling spectroscopic imaging of Au(111)," *J. Vac. Sci. Technol. A* **8**, 3662.
- Fernández-Rossier, J., 2009, "Theory of single-spin inelastic tunneling spectroscopy," *Phys. Rev. Lett.* **102**, 256802.
- Fiete, G. A., and E. J. Heller, 2003, "Colloquium: Theory of quantum corrals and quantum mirages," *Rev. Mod. Phys.* **75**, 933.
- Fischer, Ø., M. Kugler, I. Maggio-Aprile, C. Berthod, and C. Renner, 2007, "Scanning tunneling spectroscopy of high-temperature superconductors," *Rev. Mod. Phys.* **79**, 353.
- Fisher, J. C., and I. Giaever, 1961, "Tunneling through thin insulating layers," *J. Appl. Phys.* **32**, 172.
- Forster, F., G. Nicolay, F. Reinert, D. Ehm, S. Schmidt, and S. Hüfner, 2003, "Surface and interface states on adsorbate covered noble metal surfaces," *Surf. Sci.* **532–535**, 160.
- Foster, A., and W. Hofer, 2006, *NanoScience and Technology, "Scanning probe microscopy: atomic scale engineering by forces and currents"* (Springer, New York).
- Fransson, J., O. Eriksson, and A. V. Balatsky, 2010, "Theory of spin-polarized scanning tunneling microscopy applied to local spins," *Phys. Rev. B* **81**, 115454.
- Friedel, J., 1958, "Metallic alloys," *Nuovo Cimento Suppl.* **7**, 287.
- Fu, Z.-G., P. Zhang, and S.-S. Li, 2011, "Aharonov-Bohm oscillations in the local density of topological surface states," *Appl. Phys. Lett.* **99**, 243110.
- Fu, Z.-G., P. Zhang, and S.-S. Li, 2012, "Probing crossover from analogous weak antilocalization to localization by an Aharonov-Bohm interferometer on topological insulator surface," *Appl. Phys. Lett.* **100**, 133103.
- Fu, Z.-G., P. Zhang, Z. Wang, and S.-S. Li, 2011, "Quantum corrals and quantum mirages on the surface of a topological insulator," *Phys. Rev. B* **84**, 235438.
- Gambardella, P., *et al.*, 2003, "Giant magnetic anisotropy of single cobalt atoms and nanoparticles," *Science* **300**, 1130.
- Gao, C. L., A. Ernst, G. Fischer, W. Hergert, P. Bruno, W. Wulfhchel, and J. Kirschner, 2008, "Spin wave dispersion on the nanometer scale," *Phys. Rev. Lett.* **101**, 167201.
- Gao, C. L., U. Schlickum, W. Wulfhchel, and J. Kirschner, 2007, "Mapping the surface spin structure of large unit cells: Reconstructed Mn films on Fe(001)," *Phys. Rev. Lett.* **98**, 107203.

- Gao, C. L., W. Wulfhekel, and J. Kirschner, 2008, "Revealing the 120° antiferromagnetic Néel structure in real space: One monolayer Mn on Ag(111)," *Phys. Rev. Lett.* **101**, 267205.
- Gartland, P. O., S. Berge, and B. J. Slagsvold, 1973, "Surface-effect characteristics of photoemission from clean copper-crystal surfaces," *Phys. Rev. Lett.* **30**, 916.
- Gartland, P. O., and B. J. Slagsvold, 1975, "Transitions conserving parallel momentum in photoemission from the (111) face of copper," *Phys. Rev. B* **12**, 4047.
- Gauyacq, J.-P., N. Lorente, and F. D. Novaes, 2012, "Excitation of local magnetic moments by tunneling electrons," *Prog. Surf. Sci.* **87**, 63.
- Gay, T. J., and F. B. Dunning, 1992, "Mott electron polarimetry," *Rev. Sci. Instrum.* **63**, 1635.
- Giaever, I., 1960a, "Electron tunneling between two superconductors," *Phys. Rev. Lett.* **5**, 464.
- Giaever, I., 1960b, "Energy gap in superconductors measured by electron tunneling," *Phys. Rev. Lett.* **5**, 147.
- Goldmann, A., V. Dose, and G. Borstel, 1985, "Empty electronic states at the (100), (110), and (111) surfaces of nickel, copper, and silver," *Phys. Rev. B* **32**, 1971.
- Gottlieb, A. D., and L. Wesoloski, 2006, "Bardeen's tunnelling theory as applied to scanning tunnelling microscopy: a technical guide to the traditional interpretation," *Nanotechnology* **17**, R57.
- Guo, H.-M., and M. Franz, 2010, "Theory of quasiparticle interference on the surface of a strong topological insulator," *Phys. Rev. B* **81**, 041102.
- Hamers, R. J., R. M. Tromp, and J. E. Demuth, 1986, "Surface electronic structure of Si(111)-(7 × 7) resolved in real space," *Phys. Rev. Lett.* **56**, 1972.
- Hanaguri, T., S. Niitaka, K. Kuroki, and H. Takagi, 2010, "Unconventional *s*-wave superconductivity in Fe(Se,Te)," *Science* **328**, 474.
- Hansmann, M., J. I. Pascual, G. Ceballos, H.-P. Rust, and K. Horn, 2003, "Scanning tunneling spectroscopy study of Cu(554): Confinement and dimensionality at a stepped surface," *Phys. Rev. B* **67**, 121409.
- Hasan, M. Z., and C. L. Kane, 2010, "Colloquium: Topological insulators," *Rev. Mod. Phys.* **82**, 3045.
- Hasegawa, Y., and P. Avouris, 1993, "Direct observation of standing wave formation at surface steps using scanning tunneling spectroscopy," *Phys. Rev. Lett.* **71**, 1071.
- Hasegawa, Y., T. Suzuki, and T. Sakurai, 2002, "Modification of electron density in surface states: standing wave observation on Pd overlayers by STM," *Surf. Sci.* **514**, 84.
- Heimann, P., H. Neddermeyer, and H. F. Roloff, 1977, "Ultraviolet photoemission for intrinsic surface states of the noble metals," *J. Phys. C* **10**, L17.
- Heinrich, A. J., J. Gupta, C. P. Lutz, and D. M. Eigler, 2004, "Single-atom spin-flip spectroscopy," *Science* **306**, 466.
- Heinze, S., M. Bode, A. Kubetzka, O. Pietzsch, X. Nie, S. Blügel, and R. Wiesendanger, 2000, "Real-space imaging of two-dimensional antiferromagnetism on the atomic scale," *Science* **288**, 1805.
- Heinze, S., K. von Bergmann, M. Menzel, J. Brede, A. Kubetzka, R. Wiesendanger, G. Bihlmayer, and S. Blügel, 2011, "Spontaneous atomic-scale magnetic skyrmion lattice in two dimensions," *Nat. Phys.* **7**, 713.
- Heller, E. J., M. F. Crommie, C. P. Lutz, and D. M. Eigler, 1994, "Scattering and absorption of surface electron waves in quantum corrals," *Nature (London)* **369**, 464.
- Himpfel, F. J., and D. E. Eastman, 1978, "Observation of a Λ_1 -symmetry surface state on Ni(111)," *Phys. Rev. Lett.* **41**, 507.
- Hirayama, H., Y. Aoki, and C. Kato, 2011, "Quantum interference of Rashba-type spin-split surface state electrons," *Phys. Rev. Lett.* **107**, 027204.
- Hirjibehedin, C. F., C.-Y. Lin, A. F. Otte, M. Ternes, C. P. Lutz, B. A. Jones, and A. J. Heinrich, 2007, "Large magnetic anisotropy of a single atomic spin embedded in a surface molecular network," *Science* **317**, 1199.
- Hirjibehedin, C. F., C. P. Lutz, and A. J. Heinrich, 2006, "Spin coupling in engineered atomic structures," *Science* **312**, 1021.
- Hoesch, M., M. Muntwiler, V. N. Petrov, M. Hengsberger, L. Patthey, M. Shi, M. Falub, T. Greber, and J. Osterwalder, 2004, "Spin structure of the Shockley surface state on Au(111)," *Phys. Rev. B* **69**, 241401.
- Hofer, W. A., 2003, "Challenges and errors: interpreting high resolution images in scanning tunneling microscopy," *Prog. Surf. Sci.* **71**, 147.
- Hofer, W. A., A. J. Fisher, R. A. Wolkow, and P. Grütter, 2001, "Surface relaxations, current enhancements, and absolute distances in high resolution scanning tunneling microscopy," *Phys. Rev. Lett.* **87**, 236104.
- Hofer, W. A., A. S. Foster, and A. L. Shluger, 2003, "Theories of scanning probe microscopes at the atomic scale," *Rev. Mod. Phys.* **75**, 1287.
- Hofer, W. A., K. Palotás, S. Rusponi, T. Cren, and H. Brune, 2008, "Role of hydrogen in giant spin polarization observed on magnetic nanostructures," *Phys. Rev. Lett.* **100**, 026806.
- Hoffman, J. E., 2011, "Spectroscopic scanning tunneling microscopy insights into Fe-based superconductors," *Rep. Prog. Phys.* **74**, 124513.
- Hoffman, J. E., K. McElroy, D.-H. Lee, K. M. Lang, H. Eisaki, S. Uchida, and J. C. Davis, 2002, "Imaging quasiparticle interference in $\text{Bi}_2\text{Sr}_2\text{CaCu}_2\text{O}_{8+\delta}$," *Science* **297**, 1148.
- Hörmandinger, G., 1994, "Imaging of the Cu(111) surface state in scanning tunneling microscopy," *Phys. Rev. B* **49**, 13 897.
- Hövel, H., B. Grimm, and B. Reihl, 2001, "Modification of the Shockley-type surface state on Ag(111) by an adsorbed xenon layer," *Surf. Sci.* **477**, 43.
- Hsieh, D., *et al.*, 2009, "Observation of unconventional quantum spin textures in topological insulators," *Science* **323**, 919.
- Huang, R. Z., V. S. Stepanyuk, and J. Kirschner, 2006, "Interaction of scanning tunneling microscopy tip with mesoscopic islands at the atomic-scale," *J. Phys. Condens. Matter* **18**, L217.
- Huang, R. Z., V. S. Stepanyuk, A. L. Klavskyuk, W. Hergert, P. Bruno, and J. Kirschner, 2006, "Atomic relaxations and magnetic states in a single-atom tunneling junction," *Phys. Rev. B* **73**, 153404.
- Hylgaard, P., and M. Persson, 2000, "Long-ranged adsorbate-adsorbate interactions mediated by a surface-state band," *J. Phys. Condens. Matter* **12**, L13.
- Ignatiev, P. A., 2009, Ph.D. thesis (Martin-Luther-Universität Halle-Wittenberg).
- Ignatiev, P. A., O. O. Brovko, and V. S. Stepanyuk, 2012, "Local tunneling magnetoresistance control with surface-state confinement and external electric field," *Phys. Rev. B* **86**, 045409.
- Ignatiev, P. A., and V. S. Stepanyuk, 2011, "Effect of the external electric field on surface states: An ab initio study," *Phys. Rev. B* **84**, 075421.
- Ignatiev, P. A., V. S. Stepanyuk, A. L. Klavskyuk, W. Hergert, and P. Bruno, 2007, "Electronic confinement on stepped Cu(111) surfaces: Ab initio study," *Phys. Rev. B* **75**, 155428.
- Ishida, H., and A. Liebsch, 1992, "Calculation of the electronic structure of stepped metal surfaces," *Phys. Rev. B* **46**, 7153.

- Jaklevic, R. C., and L. C. Davis, 1982, "Band signatures in the low-energy-electron reflectance spectra of fcc metals," *Phys. Rev. B* **26**, 5391.
- Jeandupeux, O., L. Bürgi, A. Hirstein, H. Brune, and K. Kern, 1999, "Thermal damping of quantum interference patterns of surface-state electrons," *Phys. Rev. B* **59**, 15 926.
- Jensen, H., J. Kröger, R. Berndt, and S. Crampin, 2005, "Electron dynamics in vacancy islands: Scanning tunneling spectroscopy on Ag(111)," *Phys. Rev. B* **71**, 155417.
- Jia, J. F., K. Inoue, Y. Hasegawa, W. S. Yang, and T. Sakurai, 1998, "Variation of the local work function at steps on metal surfaces studied with STM," *Phys. Rev. B* **58**, 1193.
- Johnson, M., and J. Clarke, 1990, "Spin-polarized scanning tunneling microscope: Concept, design, and preliminary results from a prototype operated in air," *J. Appl. Phys.* **67**, 6141.
- Julliere, M., 1975, "Tunneling between ferromagnetic films," *Phys. Lett.* **54A**, 225.
- Kaiser, W. J., and R. C. Jaklevic, 1986, "Spectroscopy of electronic states of metals with a scanning tunneling microscope," *IBM J. Res. Dev.* **30**, 411.
- Kasuya, T., 1956, "A theory of metallic ferro- and antiferromagnetism on Zener's model," *Prog. Theor. Phys.* **16**, 45.
- Kawagoe, T., Y. Iguchi, T. Miyamachi, A. Yamasaki, and S. Suga, 2005, "Spiral terraces and spin frustration in layered antiferromagnetic Cr(001) films," *Phys. Rev. Lett.* **95**, 207205.
- Kelly, M. J., 1995, *Low-dimensional semiconductors: materials, physics, technology, devices* (Clarendon Press, Oxford).
- Kevan, S. D., 1983, "Evidence for a new broadening mechanism in angle-resolved photoemission from Cu(111)," *Phys. Rev. Lett.* **50**, 526.
- Kevan, S. D., and R. H. Gaylord, 1987, "High-resolution photoemission study of the electronic structure of the noble-metal (111) surfaces," *Phys. Rev. B* **36**, 5809.
- Khajetoorians, A. A., S. Lounis, B. Chilian, A. T. Costa, L. Zhou, D. L. Mills, J. Wiebe, and R. Wiesendanger, 2011, "Itinerant nature of atom-magnetization excitation by tunneling electrons," *Phys. Rev. Lett.* **106**, 037205.
- Khajetoorians, A. A., J. Wiebe, B. Chilian, S. Lounis, S. Bluegel, and R. Wiesendanger, 2012, "Atom-by-atom engineering and magnetometry of tailored nanomagnets," *Nat. Phys.* **8**, 497.
- Kim, T. K., *et al.*, 2005, "Evidence against a charge density wave on Bi(111)," *Phys. Rev. B* **72**, 085440.
- Kirschner, J., 1985, *Polarized Electrons at Surfaces* (Springer, Berlin).
- Kirschner, J., and R. Feder, 1979, "Spin polarization in double diffraction of low-energy electrons from W(001): Experiment and theory," *Phys. Rev. Lett.* **42**, 1008.
- Kittel, C., 1949, "Physical theory of ferromagnetic domains," *Rev. Mod. Phys.* **21**, 541.
- Kleiber, M., M. Bode, R. Ravlić, and R. Wiesendanger, 2000, "Topology-induced spin frustrations at the Cr(001) surface studied by spin-polarized scanning tunneling spectroscopy," *Phys. Rev. Lett.* **85**, 4606.
- Kodama, H., T. Uzumaki, M. Oshiki, K. Sueoka, and K. Mukasa, 1998, "Spin-polarized tunneling by spin-polarized scanning tunneling microscopy," *J. Appl. Phys.* **83**, 6831.
- Koike, K., 2013, "Spin-polarized scanning electron microscopy," *Microscopy* **62**, 177.
- Koike, K., and K. Hayakawa, 1984, "Scanning electron microscope observation of magnetic domains using spin-polarized secondary electrons," *Jpn. J. Appl. Phys.* **23**, L187.
- Kondo, J., 1964, "Resistance minimum in dilute magnetic alloys," *Prog. Theor. Phys.* **32**, 37.
- Konoto, M., T. Kohashi, K. Koike, T. Arima, Y. Kaneko, T. Kimura, and Y. Tokura, 2004, "Direct imaging of temperature-dependent layered antiferromagnetism of a magnetic oxide," *Phys. Rev. Lett.* **93**, 107201.
- Krahl-Urban, B., E. A. Niekisch, and H. Wagner, 1977, "Work function of stepped tungsten single crystal surfaces," *Surf. Sci.* **64**, 52.
- Kresse, G., and J. Furthmüller, 1996, "Efficient iterative schemes for ab initio total-energy calculations using a plane-wave basis set," *Phys. Rev. B* **54**, 11 169.
- Kröger, J., L. Limot, H. Jensen, R. Berndt, S. Crampin, and E. Pehlke, 2005, "Surface state electron dynamics of clean and adsorbate-covered metal surfaces studied with the scanning tunnelling microscope," *Prog. Surf. Sci.* **80**, 26.
- Kröger, J., L. Limot, H. Jensen, R. Berndt, and P. Johansson, 2004, "Stark effect in Au(111) and Cu(111) surface states," *Phys. Rev. B* **70**, 033401.
- Krömker, B., M. Escher, D. Funnemann, D. Hartung, H. Engelhard, and J. Kirschner, 2008, "Development of a momentum microscope for time resolved band structure imaging," *Rev. Sci. Instrum.* **79**, 053702.
- Kronmüller, H., and S. Parkin, 2007, Eds., *Handbook of Magnetism and Advanced Magnetic Materials*, Vols. 1–5 (Wiley, New York).
- Kubby, J. A., and W. J. Greene, 1992, "Electron interferometry at a metal-semiconductor interface," *Phys. Rev. Lett.* **68**, 329.
- Kubetzka, A., M. Bode, O. Pietzsch, and R. Wiesendanger, 2002, "Spin-polarized scanning tunneling microscopy with antiferromagnetic probe tips," *Phys. Rev. Lett.* **88**, 057201.
- Kubetzka, A., O. Pietzsch, M. Bode, and R. Wiesendanger, 2003, "Determining the spin polarization of surfaces by spin-polarized scanning tunneling spectroscopy," *Appl. Phys. A* **76**, 873.
- Kutzner, J., R. Paucksch, C. Jabs, H. Zacharias, and J. Braun, 1997, "High-resolution photoelectron emission spectroscopy of surface states on Ni(111)," *Phys. Rev. B* **56**, 16 003.
- Lazarovits, B., L. Szunyogh, and P. Weinberger, 2006, "Spin-polarized surface states close to adatoms on Cu(111)," *Phys. Rev. B* **73**, 045430.
- Li, J., W.-D. Schneider, R. Berndt, and S. Crampin, 1998, "Electron confinement to nanoscale Ag islands on Ag(111): A quantitative study," *Phys. Rev. Lett.* **80**, 3332.
- Li, J., W.-D. Schneider, R. Berndt, and B. Delley, 1998, "Kondo scattering observed at a single magnetic impurity," *Phys. Rev. Lett.* **80**, 2893.
- Li, J., W.-D. Schneider, S. Crampin, and R. Berndt, 1999, "Tunneling spectroscopy of surface state scattering and confinement," *Surf. Sci.* **422**, 95.
- Li Bassi, A., *et al.*, 2007, "Bulk Cr tips for scanning tunneling microscopy and spin-polarized scanning tunneling microscopy," *Appl. Phys. Lett.* **91**, 173120.
- Limot, L., T. Maroutian, P. Johansson, and R. Berndt, 2003, "Surface-state Stark shift in a scanning tunneling microscope," *Phys. Rev. Lett.* **91**, 196801.
- Limot, L., E. Pehlke, J. Kröger, and R. Berndt, 2005, "Surface-state localization at adatoms," *Phys. Rev. Lett.* **94**, 036805.
- Liu, Q., X.-L. Qi, and S.-C. Zhang, 2012, "Stationary phase approximation approach to the quasiparticle interference on the surface of a strong topological insulator," *Phys. Rev. B* **85**, 125314.
- Lorente, N., and J.-P. Gauyacq, 2009, "Efficient spin transitions in inelastic electron tunneling spectroscopy," *Phys. Rev. Lett.* **103**, 176601.
- Loth, S., C. P. Lutz, and A. J. Heinrich, 2010, "Spin-polarized spin excitation spectroscopy," *New J. Phys.* **12**, 125021.

- Lounis, S., A. Bringer, and S. Blügel, 2012, "Magnetic adatom induced skyrmion-like spin texture in surface electron waves," *Phys. Rev. Lett.* **108**, 207202.
- Madhavan, V., W. Chen, T. Jamneala, M. F. Crommie, and N. S. Wingreen, 1998, "Tunneling into a single magnetic atom: Spectroscopic evidence of the Kondo resonance," *Science* **280**, 567.
- Maekawa, S., and U. Gäfvert, 1982, "Electron tunneling between ferromagnetic films," *IEEE Trans. Magn.* **18**, 707.
- Magaud, L., A. Pasturel, P. Mallet, S. Pons, and J.-Y. Veuillein, 2004, "Spin-polarized Shockley state at Ni(111) free surface and at Ni Cu based structures on Cu(111) surface," *Europhys. Lett.* **67**, 90.
- Manna, S., P. L. Gastelois, M. Dąbrowski, P. Kuświk, M. Cinal, M. Przybylski, and J. Kirschner, 2013, "Effect of quantum well states in Cu overlayer on magnetic anisotropy of Fe and Co films revisited," *Phys. Rev. B* **87**, 134401.
- Manoharan, H. C., C. P. Lutz, and D. M. Eigler, 2000, "Quantum mirages formed by coherent projection of electronic structure," *Nature (London)* **403**, 512.
- Marathe, M., J. Lagoute, V. Repain, S. Rousset, and S. Narasimhan, 2012, "Spin-polarized surface states on Fe-deposited Au(111) surface: A theoretical study," *Surf. Sci.* **606**, 950.
- McElroy, K., R. W. Simmonds, J. E. Hoffman, D.-H. Lee, J. Orenstein, H. Eisaki, S. Uchida, and J. C. Davis, 2003, "Relating atomic-scale electronic phenomena to wave-like quasiparticle states in superconducting $\text{Bi}_2\text{Sr}_2\text{CaCu}_2\text{O}_{8+\delta}$," *Nature (London)* **422**, 592.
- Meier, F., S. Lounis, J. Wiebe, L. Zhou, S. Heers, P. Mavropoulos, P. H. Dederichs, S. Blügel, and R. Wiesendanger, 2011, "Spin polarization of platinum (111) induced by the proximity to cobalt nanostripes," *Phys. Rev. B* **83**, 075407.
- Meier, F., L. Zhou, J. Wiebe, and R. Wiesendanger, 2008, "Revealing magnetic interactions from single-atom magnetization curves," *Science* **320**, 82.
- Merrick, I., J. E. Inglesfield, and G. A. Attard, 2005, "Local work function and induced screening effects at stepped Pd surfaces," *Phys. Rev. B* **71**, 085407.
- Meservey, R., P. M. Tedrow, and P. Fulde, 1970, "Magnetic field splitting of the quasiparticle states in superconducting aluminum films," *Phys. Rev. Lett.* **25**, 1270.
- Miao, G.-X., M. Münzenberg, and J. S. Moodera, 2011, "Tunneling path toward spintronics," *Rep. Prog. Phys.* **74**, 036501.
- Michaelson, H. B., 1977, "The work function of the elements and its periodicity," *J. Appl. Phys.* **48**, 4729.
- Michely, T., and J. Krug, 2004, *Islands, Mounds and Atoms*, Springer Series in Surface Sciences, Vol. 42 (Springer, Berlin).
- Mitsuoka, S., and A. Tamura, 2011, "Scanning tunneling microscopic images and scanning tunneling spectra for coupled rectangular quantum corrals," *J. Phys. Condens. Matter* **23**, 275302.
- Miyazaki, T., and N. Tezuka, 1995, "Giant magnetic tunneling effect in Fe/ Al_2O_3 /Fe junction," *J. Magn. Magn. Mater.* **139**, L231.
- Moodera, J. S., L. R. Kinder, T. M. Wong, and R. Meservey, 1995, "Large magnetoresistance at room temperature in ferromagnetic thin film tunnel junctions," *Phys. Rev. Lett.* **74**, 3273.
- Moodera, J. S., J. Nassar, and G. Mathon, 1999, "Spin-tunneling in ferromagnetic junctions," *Annu. Rev. Mater. Sci.* **29**, 381.
- Müller, E. W., and T. T. Tsong, 1969, *Field ion microscopy: principles and applications* (American Elsevier Pub. Co., New York).
- Nagai, S., K. Hata, H. Oka, D. Sander, and J. Kirschner, 2014, "Atomic structure and spin polarization at the apex of tips used in spin-polarized scanning tunneling microscopy," *Appl. Phys. Express* **7**, 025204.
- Niebergall, L., G. Rodary, H. F. Ding, D. Sander, V. S. Stepanyuk, P. Bruno, and J. Kirschner, 2006, "Electron confinement in hexagonal vacancy islands: Theory and experiment," *Phys. Rev. B* **74**, 195436.
- Niebergall, L., V. S. Stepanyuk, J. Berakdar, and P. Bruno, 2006, "Controlling the spin polarization of nanostructures on magnetic substrates," *Phys. Rev. Lett.* **96**, 127204.
- Nishide, A., A. A. Taskin, Y. Takeichi, T. Okuda, A. Kakizaki, T. Hirahara, K. Nakatsuji, F. Komori, Y. Ando, and I. Matsuda, 2010, "Direct mapping of the spin-filtered surface bands of a three-dimensional quantum spin Hall insulator," *Phys. Rev. B* **81**, 041309.
- Nishimura, Y., M. Takeya, M. Higashiguchi, A. Kimura, M. Taniguchi, H. Narita, Y. Cui, M. Nakatake, K. Shimada, and H. Namatame, 2009, "Surface electronic structures of ferromagnetic Ni(111) studied by STM and angle-resolved photoemission," *Phys. Rev. B* **79**, 245402.
- Oepen, H. P., and R. Frömter, 2007, in *Handbook of Magnetism and Advanced Magnetic Materials*, Vol. 3, edited by H. Kronmüller and S. Parkin (John Wiley & Sons, Ltd., New York).
- Oepen, H. P., and J. Kirschner, 1989, "Magnetization distribution of 180° domain walls at Fe(100) single-crystal surfaces," *Phys. Rev. Lett.* **62**, 819.
- Ohno, H., 1998, "Making nonmagnetic semiconductors ferromagnetic," *Science* **281**, 951.
- Ohwaki, T., D. Wortmann, H. Ishida, S. Blügel, and K. Terakura, 2006, "Spin-polarized field emission from Ni(001) and Ni(111) surfaces," *Phys. Rev. B* **73**, 235424.
- Oka, H., P. A. Ignatiev, S. Wedekind, G. Rodary, L. Niebergall, V. S. Stepanyuk, D. Sander, and J. Kirschner, 2010, "Spin-dependent quantum interference within a single magnetic nanostructure," *Science* **327**, 843.
- Oka, H., K. Tao, S. Wedekind, G. Rodary, V. S. Stepanyuk, D. Sander, and J. Kirschner, 2011, "Spatially modulated tunnel magnetoresistance on the nanoscale," *Phys. Rev. Lett.* **107**, 187201.
- Okawa, R., Y. Morikawa, S. Nagai, T. Iwata, K. Kajiwara, and K. Hata, 2011, "Stability measurement of ion beam current from argon field ion source," *e-J. Surf. Sci. Nanotechnol.* **9**, 371.
- Okuda, T., and A. Kimura, 2013, "Spin- and angle-resolved photoemission of strongly spin-orbit coupled systems," *J. Phys. Soc. Jpn.* **82**, 021002.
- Okuda, T., *et al.*, 2009, "Exchange splitting of the three $\bar{\Gamma}$ surface states of Ni(111) from three-dimensional spin- and angle-resolved photoemission spectroscopy," *Phys. Rev. B* **80**, 180404.
- Olsson, F. E., M. Persson, A. G. Borisov, J.-P. Gauyacq, J. Lagoute, and S. Fölsch, 2004, "Localization of the Cu(111) surface state by single Cu adatoms," *Phys. Rev. Lett.* **93**, 206803.
- Ono, M., Y. Nishigata, T. Nishio, T. Eguchi, and Y. Hasegawa, 2006, "Electrostatic potential screened by a two-dimensional electron system: A real-space observation by scanning-tunneling spectroscopy," *Phys. Rev. Lett.* **96**, 016801.
- Ortega, J. E., and F. J. Himpsel, 1992, "Quantum well states as mediators of magnetic coupling in superlattices," *Phys. Rev. Lett.* **69**, 844.
- Ortega, J. E., F. J. Himpsel, G. J. Mankey, and R. F. Willis, 1993, "Quantum-well states and magnetic coupling between ferromagnets through a noble-metal layer," *Phys. Rev. B* **47**, 1540.
- Ortega, J. E., J. Lobo-Checa, G. Peschel, S. Schirone, Z. M. Abd El-Fattah, M. Matena, F. Schiller, P. Borghetti, P. Gambardella, and A. Mugarza, 2013, "Scattering of surface electrons by isolated steps versus periodic step arrays," *Phys. Rev. B* **87**, 115425.
- Ortega, J. E., A. Mugarza, V. Repain, S. Rousset, V. Pérez-Dieste, and A. Mascaraque, 2002, "One-dimensional versus two-dimensional surface states on stepped Au(111)," *Phys. Rev. B* **65**, 165413.

- Ortega, J. E., M. Ruiz-Osés, J. Cordón, A. Mugarza, J. Kuntze, and F. Schiller, 2005, "One-dimensional versus two-dimensional electronic states in vicinal surfaces," *New J. Phys.* **7**, 101.
- Ortega, J. E., S. Speller, A. R. Bachmann, A. Mascaraque, E. G. Michel, A. Närmann, A. Mugarza, A. Rubio, and F. J. Himpsel, 2000, "Electron wave function at a vicinal surface: Switch from terrace to step modulation," *Phys. Rev. Lett.* **84**, 6110.
- Otte, A. F., M. Ternes, S. Loth, C. P. Lutz, C. F. Hirjibehedin, and A. J. Heinrich, 2009, "Spin excitations of a Kondo-screened atom coupled to a second magnetic atom," *Phys. Rev. Lett.* **103**, 107203.
- Otte, A. F., M. Ternes, K. von Bergmann, S. Loth, H. Brune, C. P. Lutz, C. F. Hirjibehedin, and A. J. Heinrich, 2008, "The role of magnetic anisotropy in the Kondo effect," *Nat. Phys.* **4**, 847.
- Ouazi, S., S. Wedekind, G. Rodary, H. Oka, D. Sander, and J. Kirschner, 2012, "Magnetization reversal of individual Co nanoislands," *Phys. Rev. Lett.* **108**, 107206.
- Palotás, K., and W. A. Hofer, 2005, "Multiple scattering in a vacuum barrier obtained from real-space wavefunctions," *J. Phys. Condens. Matter* **17**, 2705.
- Park, J.-Y., U. D. Ham, S.-J. Kahng, Y. Kuk, K. Miyake, K. Hata, and H. Shigekawa, 2000, "Modification of surface-state dispersion upon Xe adsorption: A scanning tunneling microscope study," *Phys. Rev. B* **62**, R16341.
- Park, J. Y., G. M. Sacha, M. Enachescu, D. F. Ogletree, R. A. Ribeiro, P. C. Canfield, C. J. Jenks, P. A. Thiel, J. J. Sáenz, and M. Salmeron, 2005, "Sensing dipole fields at atomic steps with combined scanning tunneling and force microscopy," *Phys. Rev. Lett.* **95**, 136802.
- Parkin, S., H. Yang, S.-H. Yang, and M. Hayashi, 2007, in *Handbook of Magnetism and Advanced Magnetic Materials*, Vol. 5, edited by H. Kronmüller and S. Parkin (John Wiley & Sons, Inc., New York).
- Parkin, S. S. P., R. Bhadra, and K. P. Roche, 1991, "Oscillatory magnetic exchange coupling through thin copper layers," *Phys. Rev. Lett.* **66**, 2152.
- Parkin, S. S. P., C. Kaiser, A. Panchula, P. M. Rice, B. Hughes, M. Samant, and S. H. Yang, 2004, "Giant tunnelling magnetoresistance at room temperature with MgO(100) tunnel barriers," *Nat. Mater.* **3**, 862.
- Parkin, S. S. P., N. More, and K. P. Roche, 1990, "Oscillations in exchange coupling and magnetoresistance in metallic superlattice structures: Co/Ru, Co/Cr, and Fe/Cr," *Phys. Rev. Lett.* **64**, 2304.
- Pascual, J. I., A. Dick, M. Hansmann, H. P. Rust, J. Neugebauer, and K. Horn, 2006, "Bulk electronic structure of metals resolved with scanning tunneling microscopy," *Phys. Rev. Lett.* **96**, 046801.
- Pascual, J. I., *et al.*, 2004, "Role of spin in quasiparticle interference," *Phys. Rev. Lett.* **93**, 196802.
- Payne, F. W., W. Jiang, and L. A. Bloomfield, 2006, "Magnetism and magnetic isomers in free chromium clusters," *Phys. Rev. Lett.* **97**, 193401.
- Pennec, Y., W. Auwärter, A. Schiffrin, A. Weber-Bargioni, A. Riemann, and J. V. Barth, 2007, "Supramolecular gratings for tuneable confinement of electrons on metal surfaces," *Nat. Nanotechnol.* **2**, 99.
- Perdew, J. P., and Y. Wang, 1992, "Accurate and simple analytic representation of the electron-gas correlation energy," *Phys. Rev. B* **45**, 13244.
- Petersen, L., P. Hofmann, E. W. Plummer, and F. Besenbacher, 2000, "Fourier transform-STM: determining the surface Fermi contour," *J. Electron Spectrosc. Relat. Phenom.* **109**, 97.
- Petersen, L., P. Laitenberger, E. Lægsgaard, and F. Besenbacher, 1998, "Screening waves from steps and defects on Cu(111) and Au(111) imaged with STM: Contribution from bulk electrons," *Phys. Rev. B* **58**, 7361.
- Petersen, L., P. T. Sprunger, P. Hofmann, E. Lægsgaard, B. G. Briner, M. Doering, H.-P. Rust, A. M. Bradshaw, F. Besenbacher, and E. W. Plummer, 1998, "Direct imaging of the two-dimensional Fermi contour: Fourier-transform STM," *Phys. Rev. B* **57**, R6858.
- Phark, S.-H., J. A. Fischer, M. Corbetta, D. Sander, and J. Kirschner, 2013, "Superparamagnetic response of Fe-coated W tips in spin-polarized scanning tunneling microscopy," *Appl. Phys. Lett.* **103**, 032407.
- Pierce, D. T., 1988, "Spin-polarized electron microscopy," *Phys. Scr.* **38**, 291.
- Pierce, D. T., and F. Meier, 1976, "Photoemission of spin-polarized electrons from GaAs," *Phys. Rev. B* **13**, 5484.
- Pietzsch, O., A. Kubetzka, M. Bode, and R. Wiesendanger, 2004, "Spin-polarized scanning tunneling spectroscopy of nanoscale cobalt islands on Cu(111)," *Phys. Rev. Lett.* **92**, 057202.
- Pietzsch, O., A. Kubetzka, D. Haude, M. Bode, and R. Wiesendanger, 2000, "A low-temperature ultrahigh vacuum scanning tunneling microscope with a split-coil magnet and a rotary motion stepper motor for high spatial resolution studies of surface magnetism," *Rev. Sci. Instrum.* **71**, 424.
- Pietzsch, O., S. Okatov, A. Kubetzka, M. Bode, S. Heinze, A. Lichtenstein, and R. Wiesendanger, 2006, "Spin-resolved electronic structure of nanoscale cobalt islands on Cu(111)," *Phys. Rev. Lett.* **96**, 237203.
- Polyakov, O. P., M. Corbetta, O. V. Stepanyuk, H. Oka, A. M. Saletsky, D. Sander, V. S. Stepanyuk, and J. Kirschner, 2012, "Spin-dependent Smoluchowski effect," *Phys. Rev. B* **86**, 235409.
- Pons, S., P. Mallet, L. Magaud, and J. Y. Veuille, 2003, "Investigation of the Ni(111) Shockley-like surface state using confinement to artificial nanostructures," *Europhys. Lett.* **61**, 375.
- Pons, S., P. Mallet, and J.-Y. Veuille, 2001, "Electron confinement in nickel and copper nanostructures on Cu(111)," *Phys. Rev. B* **64**, 193408.
- Pratzer, M., H. J. Elmers, M. Bode, O. Pietzsch, A. Kubetzka, and R. Wiesendanger, 2001, "Atomic-scale magnetic domain walls in quasi-one-dimensional Fe nanostripes," *Phys. Rev. Lett.* **87**, 127201.
- Prins, M. W. J., D. L. Abraham, and H. van Kempen, 1993, "Spin-dependent transmission at ferromagnet/semiconductor interfaces," *J. Magn. Magn. Mater.* **121**, 152.
- Przybylski, M., M. Dąbrowski, U. Bauer, M. Cinal, and J. Kirschner, 2012, "Oscillatory magnetic anisotropy due to quantum well states in thin ferromagnetic films (invited)," *J. Appl. Phys.* **111**, 07C102 [<http://dx.doi.org/10.1063/1.3670498>].
- Qi, X.-L., and S.-C. Zhang, 2011, "Topological insulators and superconductors," *Rev. Mod. Phys.* **83**, 1057.
- Rastei, M. V., J. P. Bucher, P. A. Ignatiev, V. S. Stepanyuk, and P. Bruno, 2007, "Surface electronic states in Co nanoclusters on Au(111): Scanning tunneling spectroscopy measurements and ab initio calculations," *Phys. Rev. B* **75**, 045436.
- Rastei, M. V., B. Heinrich, L. Limot, P. A. Ignatiev, V. S. Stepanyuk, P. Bruno, and J. P. Bucher, 2007, "Size-dependent surface states of strained cobalt nanoislands on Cu(111)," *Phys. Rev. Lett.* **99**, 246102.
- Ravlić, R., M. Bode, A. Kubetzka, and R. Wiesendanger, 2003, "Correlation of dislocation and domain structure of Cr(001) investigated by spin-polarized scanning tunneling microscopy," *Phys. Rev. B* **67**, 174411.
- Reinert, F., G. Nicolay, S. Schmidt, D. Ehm, and S. Hüfner, 2001, "Direct measurements of the L-gap surface states on the (111) face of noble metals by photoelectron spectroscopy," *Phys. Rev. B* **63**, 115415.
- Rocha, A. R., V. M. García-Suárez, S. Bailey, C. Lambert, J. Ferrer, and S. Sanvito, 2005, "Towards molecular spintronics," *Nat. Mater.* **4**, 335.

- Rocha, A. R., V. M. García-Suárez, S. Bailey, C. Lambert, J. Ferrer, and S. Sanvito, 2006, "Spin and molecular electronics in atomically generated orbital landscapes," *Phys. Rev. B* **73**, 085414.
- Rodary, G., J.-C. Girard, L. Largeau, C. David, O. Mauguin, and Z.-Z. Wang, 2011, "Atomic structure of tip apex for spin-polarized scanning tunneling microscopy," *Appl. Phys. Lett.* **98**, 082505.
- Rodary, G., D. Sander, H. Liu, H. Zhao, L. Niebergall, V. S. Stepanyuk, P. Bruno, and J. Kirschner, 2007, "Quantization of the electron wave vector in nanostructures: Counting k -states," *Phys. Rev. B* **75**, 233412.
- Rodary, G., S. Wedekind, H. Oka, D. Sander, and J. Kirschner, 2009, "Characterization of tips for spin-polarized scanning tunneling microscopy," *Appl. Phys. Lett.* **95**, 152513.
- Rodary, G., S. Wedekind, D. Sander, and J. Kirschner, 2008, "Magnetic hysteresis loop of single Co nano-islands," *Jpn. J. Appl. Phys.* **47**, 9013.
- Roushan, P., J. Seo, C. V. Parker, Y. S. Hor, D. Hsieh, D. Qian, A. Richardella, M. Z. Hasan, R. J. Cava, and A. Yazdani, 2009, "Topological surface states protected from backscattering by chiral spin texture," *Nature (London)* **460**, 1106.
- Ruderman, M. A., and C. Kittel, 1954, "Indirect exchange coupling of nuclear magnetic moments by conduction electrons," *Phys. Rev.* **96**, 99.
- Rungger, I., and S. Sanvito, 2008, "Algorithm for the construction of self-energies for electronic transport calculations based on singularity elimination and singular value decomposition," *Phys. Rev. B* **78**, 035407.
- Rusponi, S., N. Weiss, T. Cren, M. Epple, and H. Brune, 2005, "High tunnel magnetoresistance in spin-polarized scanning tunneling microscopy of Co nanoparticles on Pt(111)," *Appl. Phys. Lett.* **87**, 162514.
- Sander, D., 2004, "The magnetic anisotropy and spin reorientation of nanostructures and nanoscale films," *J. Phys. Condens. Matter* **16**, R603.
- Sander, D., H. Oka, M. Corbetta, V. Stepanyuk, and J. Kirschner, 2013, "New insights into nano-magnetism by spin-polarized scanning tunneling microscopy," *J. Electron Spectrosc. Relat. Phenom.* **189**, 206.
- Schlenhoff, A., S. Krause, G. Herzog, and R. Wiesendanger, 2010, "Bulk Cr tips with full spatial magnetic sensitivity for spin-polarized scanning tunneling microscopy," *Appl. Phys. Lett.* **97**, 083104.
- Schlickum, U., W. Wulfhekel, and J. Kirschner, 2003, "Spin-polarized scanning tunneling microscope for imaging the in-plane magnetization," *Appl. Phys. Lett.* **83**, 2016.
- Schmid, M., W. Hebenstreit, P. Varga, and S. Crampin, 1996, "Quantum wells and electron interference phenomena in Al due to subsurface noble gas bubbles," *Phys. Rev. Lett.* **76**, 2298.
- Schouteden, K., K. Lauwaet, D. A. Muzychenko, P. Lievens, and C. V. Haesendonck, 2011, "Spin-dependent electronic structure of self-organized Co nanomagnets," *New J. Phys.* **13**, 033030.
- Schouteden, K., P. Lievens, and C. Van Haesendonck, 2009, "Fourier-transform scanning tunneling microscopy investigation of the energy versus wave vector dispersion of electrons at the Au (111) surface," *Phys. Rev. B* **79**, 195409.
- Schouteden, K., and C. Van Haesendonck, 2009, "Quantum confinement of hot image-potential state electrons," *Phys. Rev. Lett.* **103**, 266805.
- Schouteden, K., and C. Van Haesendonck, 2012, "Lateral quantization of two-dimensional electron states by embedded Ag nanocrystals," *Phys. Rev. Lett.* **108**, 076806.
- Shinohara, R., K. Yamaguchi, Y. Suzuki, and W. Nabhan, 1998, "Fabrication of GaAs microtips and their application to spin-polarized scanning tunneling microscope," *Jpn. J. Appl. Phys.* **37**, 7151.
- Shockley, W., 1939, "On the surface states associated with a periodic potential," *Phys. Rev.* **56**, 317.
- Silly, F., M. Pivetta, M. Ternes, F. Patthey, J. P. Pelz, and W.-D. Schneider, 2004, "Creation of an atomic superlattice by immersing metallic adatoms in a two-dimensional electron sea," *Phys. Rev. Lett.* **92**, 016101.
- Simon, B., 1976, "The bound state of weakly coupled Schrödinger operators in one and two dimensions," *Ann. Phys. (Berlin)* **97**, 279.
- Singh, U. R., M. Enayat, S. C. White, and P. Wahl, 2013, "Construction and performance of a dilution-refrigerator based spectroscopic-imaging scanning tunneling microscope," *Rev. Sci. Instrum.* **84**, 013708.
- Smirnov, A., N. Negulyaev, L. Niebergall, W. Hergert, A. Saletsky, and V. Stepanyuk, 2008, "Effect of quantum confinement of surface electrons on an atomic motion on nanoislands: Ab initio calculations and kinetic Monte Carlo simulations," *Phys. Rev. B* **78**, 041405.
- Smirnov, A. S., N. N. Negulyaev, W. Hergert, A. M. Saletsky, and V. S. Stepanyuk, 2009, "Magnetic behavior of one- and two-dimensional nanostructures stabilized by surface-state electrons: a kinetic Monte Carlo study," *New J. Phys.* **11**, 063004.
- Smoluchowski, R., 1941, "Anisotropy of the electronic work function of metals," *Phys. Rev.* **60**, 661.
- Snijders, P. C., P. S. Johnson, N. P. Guisinger, S. C. Erwin, and F. J. Himpsel, 2012, "Spectroscopic evidence for spin-polarized edge states in graphitic Si nanowires," *New J. Phys.* **14**, 103004.
- Song, Y. J., A. F. Otte, V. Shvarts, Z. Zhao, Y. Kuk, S. R. Blankenship, A. Band, F. M. Hess, and J. A. Stroscio, 2010, "Invited review article: A 10 mK scanning probe microscopy facility," *Rev. Sci. Instrum.* **81**, 121101.
- Song, Z., J. I. Pascual, H. Conrad, K. Horn, and H.-P. Rust, 2001, "Surface states of d character imaged by scanning tunneling microscopy," *Surf. Sci.* **491**, 39.
- Sprunger, P. T., L. Petersen, E. W. Plummer, E. Lægsgaard, and F. Besenbacher, 1997, "Giant Friedel oscillations on the beryllium (0001) surface," *Science* **275**, 1764.
- Steinbrecher, M., H. Harutyunyan, C. R. Ast, and D. Wegner, 2013, "Rashba-type spin splitting from interband scattering in quasiparticle interference maps," *Phys. Rev. B* **87**, 245436.
- Stepanyuk, V. S., A. N. Baranov, D. V. Tsvilin, W. Hergert, P. Bruno, N. Knorr, M. A. Schneider, and K. Kern, 2003, "Quantum interference and long-range adsorbate-adsorbate interactions," *Phys. Rev. B* **68**, 205410.
- Stepanyuk, V. S., N. N. Negulyaev, L. Niebergall, and P. Bruno, 2007, "Effect of quantum confinement of surface electrons on adatom-adatom interactions," *New J. Phys.* **9**, 388.
- Stepanyuk, V. S., L. Niebergall, W. Hergert, and P. Bruno, 2005, "Ab initio study of mirages and magnetic interactions in quantum corrals," *Phys. Rev. Lett.* **94**, 187201.
- Stepanyuk, V. S., L. Niebergall, R. C. Longo, W. Hergert, and P. Bruno, 2004, "Magnetic nanostructures stabilized by surface-state electrons," *Phys. Rev. B* **70**, 075414.
- Stroscio, J. A., and D. M. Eigler, 1991, "Atomic and molecular manipulation with the scanning tunneling microscope," *Science* **254**, 1319.
- Stróżecka, A., A. Eguren, and J. I. Pascual, 2011, "Quasiparticle interference around a magnetic impurity on a surface with strong spin-orbit coupling," *Phys. Rev. Lett.* **107**, 186805.
- Subagyo, A., and K. Sueoka, 2006, "Spin-polarized scanning tunneling microscopy study on charge ordering of reconstructed Fe₃O₄(001) film surfaces," *Jpn. J. Appl. Phys.* **45**, 2255.

- Sueoka, K., K. Mukasa, and K. Hayakawa, 1993, "Possibility of observing spin-polarized tunneling current using scanning tunneling microscope with optically pumped GaAs," *Jpn. J. Appl. Phys.* **32**, 2989.
- Sueoka, K., A. Subagyo, H. Hosoi, and K. Mukasa, 2004, "Magnetic imaging with scanning probe microscopy," *Nanotechnology* **15**, S691.
- Sugiura, Y., H. Liu, T. Iwata, S. Nagai, K. Kajiwara, K. Asaka, Y. Saito, and K. Hata, 2011, "Fabrication of gas field ion emitter by field induced oxygen etching method," *e-J. Surf. Sci. Nanotechnol.* **9**, 344.
- Sukhov, A., and J. Berakdar, 2008, "Temperature-dependent magnetization dynamics of magnetic nanoparticles," *J. Phys. Condens. Matter* **20**, 125226.
- Tamm, I., 1932, "Über eine mögliche Art der Elektronenbindung an Kristalloberflächen," *Z. Phys.* **76**, 849.
- Tange, A., C. L. Gao, B. Y. Yavorsky, I. V. Maznichenko, C. Etz, A. Ernst, W. Hergert, I. Mertig, W. Wulfhekel, and J. Kirschner, 2010, "Electronic structure and spin polarization of the Fe(001)- $p(1 \times 1)$ O surface," *Phys. Rev. B* **81**, 195410.
- Tao, K., V. S. Stepanyuk, W. Hergert, I. Rungger, S. Sanvito, and P. Bruno, 2009, "Switching a single spin on metal surfaces by a STM tip: Ab Initio studies," *Phys. Rev. Lett.* **103**, 057202.
- Tedrow, P. M., and R. Meservey, 1971a, "Direct observation of spin-state mixing in superconductors," *Phys. Rev. Lett.* **27**, 919.
- Tedrow, P. M., and R. Meservey, 1971b, "Spin-dependent tunneling into ferromagnetic nickel," *Phys. Rev. Lett.* **26**, 192.
- Tedrow, P. M., and R. Meservey, 1973, "Spin polarization of electrons tunneling from films of Fe, Co, Ni, and Gd," *Phys. Rev. B* **7**, 318.
- Tersoff, J., and D. R. Hamann, 1983, "Theory and application for the scanning tunneling microscope," *Phys. Rev. Lett.* **50**, 1998.
- Tersoff, J., and D. R. Hamann, 1985, "Theory of the scanning tunneling microscope," *Phys. Rev. B* **31**, 805.
- Tillmann, D., R. Thiel, and E. Kisker, 1989, "Very-low-energy spin-polarized electron diffraction from Fe(001)," *Z. Phys. B* **77**, 1.
- Tournier-Colletta, C., B. Kierren, Y. Fagot-Revurat, C. Chatelain, and D. Malterre, 2011, "Enhanced electron confinement in pyramidal nanostructures," *Phys. Rev. B* **84**, 165420.
- Tournier-Colletta, C., B. Kierren, Y. Fagot-Revurat, and D. Malterre, 2010, "Phonon contribution to the lifetime of surface state quasiparticles confined in nanopillars," *Phys. Rev. Lett.* **104**, 016802.
- Tsong, T. T., 1990, *Atom-probe field ion microscopy: field ion emission and surfaces and interfaces at atomic resolution* (Cambridge University Press, Cambridge, England).
- Tsukahara, N., *et al.*, 2009, "Adsorption-induced switching of magnetic anisotropy in a single iron(II) phthalocyanine molecule on an oxidized Cu(110) surface," *Phys. Rev. Lett.* **102**, 167203.
- Tsymbal, E. Y., O. N. Mryasov, and P. R. LeClair, 2003, "Spin-dependent tunnelling in magnetic tunnel junctions," *J. Phys. Condens. Matter* **15**, R109.
- Ünal, A. A., C. Tusche, S. Ouazi, S. Wedekind, C.-T. Chiang, A. Winkelmann, D. Sander, J. Henk, and J. Kirschner, 2011, "Hybridization between the unoccupied Shockley surface state and bulk electronic states on Cu(111)," *Phys. Rev. B* **84**, 073107.
- Unguris, J., R. J. Celotta, and D. T. Pierce, 1991, "Observation of two different oscillation periods in the exchange coupling of Fe/Cr/Fe(100)," *Phys. Rev. Lett.* **67**, 140.
- Unguris, J., G. Hembree, R. J. Celotta, and D. T. Pierce, 1986, "Investigations of magnetic microstructures using scanning electron microscopy with spin polarization analysis," *J. Magn. Magn. Mater.* **54-57**, 1629.
- Vitali, L., P. Wahl, M. A. Schneider, K. Kern, V. M. Silkin, E. V. Chulkov, and P. M. Echenique, 2003, "Inter- and intraband inelastic scattering of hot surface state electrons at the Ag(111) surface," *Surf. Sci.* **523**, L47.
- von Bergmann, K., M. Bode, A. Kubetzka, M. Heide, S. Blügel, and R. Wiesendanger, 2004, "Spin-polarized electron scattering at single oxygen adsorbates on a magnetic surface," *Phys. Rev. Lett.* **92**, 046801.
- Wadas, A., and H. J. Hug, 1992, "Models for the stray field from magnetic tips used in magnetic force microscopy," *J. Appl. Phys.* **72**, 203.
- Wahl, P., M. A. Schneider, L. Diekhöner, R. Vogelgesang, and K. Kern, 2003, "Quantum coherence of image-potential states," *Phys. Rev. Lett.* **91**, 106802.
- Wahl, P., M. A. Schneider, L. Diekhöner, R. Vogelgesang, and K. Kern, 2005, "Wahl et al. reply:," *Phys. Rev. Lett.* **95**, 029702.
- Wahlström, E., I. Ekvall, H. Olin, and L. Walldén, 1998, "Long-range interaction between adatoms at the Cu(111) surface imaged by scanning tunnelling microscopy," *Appl. Phys. A* **66**, S1107.
- Walls, J. D., and E. J. Heller, 2007, "Spin-orbit coupling induced interference in quantum corrals," *Nano Lett.* **7**, 3377.
- Wandelt, K., 1991, "Properties and influence of surface defects," *Surf. Sci.* **251-252**, 387.
- Wedekind, S., 2010, Ph.D. thesis (Martin-Luther-Universität Halle-Wittenberg).
- Wedekind, S., G. Rodary, J. Borme, S. Ouazi, Y. Nahas, M. Corbetta, H. Oka, D. Sander, and J. Kirschner, 2011, "Switching fields of individual Co nanoislands," *IEEE Trans. Magn.* **47**, 3351.
- Weisbuch, C., and B. Vinter, 1991, *Quantum semiconductor structures: Fundamentals and applications* (Academic Press, New York).
- Weismann, A., M. Wenderoth, S. Lounis, P. Zahn, N. Quaas, R. G. Ulbrich, P. H. Dederichs, and S. Blügel, 2009, "Seeing the Fermi surface in real space by nanoscale electron focusing," *Science* **323**, 1190.
- Welker, J., and F. J. Giessibl, 2012, "Revealing the angular symmetry of chemical bonds by atomic force microscopy," *Science* **336**, 444.
- Wiebe, J., A. Wachowiak, F. Meier, D. Haude, T. Foster, M. Morgenstern, and R. Wiesendanger, 2004, "A 300 mK ultra-high vacuum scanning tunneling microscope for spin-resolved spectroscopy at high energy resolution," *Rev. Sci. Instrum.* **75**, 4871.
- Wiesendanger, R., 1994, *Scanning Probe Microscopy and Spectroscopy Methods and Applications* (Cambridge University Press, Cambridge, UK).
- Wiesendanger, R., 2009, "Spin mapping at the nanoscale and atomic scale," *Rev. Mod. Phys.* **81**, 1495.
- Wiesendanger, R., 2011, "Single-atom magnetometry," *Curr. Opin. Solid State Mater. Sci.* **15**, 1.
- Wiesendanger, R., H. J. Güntherodt, G. Güntherodt, R. J. Gambino, and R. Ruf, 1990, "Observation of vacuum tunneling of spin-polarized electrons with the scanning tunneling microscope," *Phys. Rev. Lett.* **65**, 247.
- Wiesendanger, R., I. V. Shvets, D. Bürgler, G. Tarrach, H. J. Güntherodt, J. M. D. Coey, and S. Gräser, 1992, "Topographic and magnetic-sensitive scanning tunneling microscope study of magnetite," *Science* **255**, 583.
- Winkelmann, A., D. Hartung, H. Engelhard, C.-T. Chiang, and J. Kirschner, 2008, "High efficiency electron spin polarization analyzer based on exchange scattering at Fe/W(001)," *Rev. Sci. Instrum.* **79**, 083303.
- Wortmann, D., S. Heinze, P. Kurz, G. Bihlmayer, and S. Blügel, 2001, "Resolving complex atomic-scale spin structures

- by spin-polarized scanning tunneling microscopy,” *Phys. Rev. Lett.* **86**, 4132.
- Wulfhekel, W., and C. L. Gao, 2010, “Investigation of non-collinear spin states with scanning tunneling microscopy,” *J. Phys. Condens. Matter* **22**, 084021.
- Wulfhekel, W., and J. Kirschner, 1999, “Spin-polarized scanning tunneling microscopy on ferromagnets,” *Appl. Phys. Lett.* **75**, 1944.
- Wulfhekel, W., and J. Kirschner, 2007, “Spin-polarized scanning tunneling microscopy of magnetic structures and antiferromagnetic thin films,” *Annu. Rev. Mater. Res.* **37**, 69.
- Wüsch, C., C. Stamm, S. Egger, D. Pescia, W. Baltensperger, and J. S. Helman, 1997, “Quantum oscillations in a confined electron gas,” *Nature (London)* **389**, 937.
- Yamada, T. K., M. M. J. Bischoff, G. M. M. Heijnen, T. Mizoguchi, and H. van Kempen, 2003, “Observation of spin-polarized surface states on ultrathin bct Mn(001) films by spin-polarized scanning tunneling spectroscopy,” *Phys. Rev. Lett.* **90**, 056803.
- Yamasaki, A., W. Wulfhekel, R. Hertel, S. Suga, and J. Kirschner, 2003, “Direct observation of the single-domain limit of Fe nanomagnets by spin-polarized scanning tunneling spectroscopy,” *Phys. Rev. Lett.* **91**, 127201.
- Yang, H., A. R. Smith, M. Prikhodko, and W. R. L. Lambrecht, 2002, “Atomic-scale spin-polarized scanning tunneling microscopy applied to $\text{Mn}_3\text{N}_2(010)$,” *Phys. Rev. Lett.* **89**, 226101.
- Yang, M. C., C. L. Lin, W. B. Su, S. P. Lin, S. M. Lu, H. Y. Lin, C. S. Chang, W. K. Hsu, and T. T. Tsong, 2009, “Phase contribution of image potential on empty quantum well states in Pb islands on the Cu(111) surface,” *Phys. Rev. Lett.* **102**, 196102.
- Yazyev, O. V., 2010, “Emergence of magnetism in graphene materials and nanostructures,” *Rep. Prog. Phys.* **73**, 056501.
- Yosida, K., 1957, “Magnetic properties of Cu-Mn alloys,” *Phys. Rev.* **106**, 893.
- Yu, Y., K. Sagisaka, and D. Fujita, 2009, “Modification of surface electronic properties on alloy surfaces: Standing waves on a Cu-9 at. % Al(111) surface observed by STM,” *Phys. Rev. B* **79**, 235427.
- Yu, Y., Y. Zhang, L. She, P. Wu, M. Huang, and G. Cao, 2013, “Scanning tunneling microscopy investigation of electronic properties of cobalt nanoislands supported by Cu-9 at. % Al(111),” *Surf. Sci.* **609**, 172.
- Yuasa, S., T. Nagahama, A. Fukushima, Y. Suzuki, and K. Ando, 2004, “Giant room-temperature magnetoresistance in single-crystal Fe/MgO/Fe magnetic tunnel junctions,” *Nat. Mater.* **3**, 868.
- Zak, J., 1984, “Band crossing and surface states in solids,” *Phys. Lett.* **106A**, 399.
- Zak, J., 1985, “Symmetry criterion for surface states in solids,” *Phys. Rev. B* **32**, 2218.
- Zangwill, A., 1988, *Physics at Surfaces* (Cambridge University Press, Cambridge, England).
- Zener, C., 1951a, “Interaction between the *d* shells in the transition metals,” *Phys. Rev.* **81**, 440.
- Zener, C., 1951b, “Interaction between the *d*-shells in the transition metals. II. ferromagnetic compounds of manganese with perovskite structure,” *Phys. Rev.* **82**, 403.
- Zhang, L., T. Miyamachi, T. Tomanić, R. Dehm, and W. Wulfhekel, 2011, “A compact sub-Kelvin ultrahigh vacuum scanning tunneling microscope with high energy resolution and high stability,” *Rev. Sci. Instrum.* **82**, 103702.
- Zhang, T., *et al.*, 2009, “Experimental demonstration of topological surface states protected by time-reversal symmetry,” *Phys. Rev. Lett.* **103**, 266803.
- Zhou, L., J. Wiebe, S. Lounis, E. Vedmedenko, F. Meier, S. Blügel, P. H. Dederichs, and R. Wiesendanger, 2010, “Strength and directionality of surface Ruderman-Kittel-Kasuya-Yosida interaction mapped on the atomic scale,” *Nat. Phys.* **6**, 187.